THE UNIVERSITY OF CALGARY

A Study of Visible Atomic Oxygen Airglow over Arecibo

by

Diana Helen Piggott

A THESIS

SUBMITTED TO THE FACULTY OF GRADUATE STUDIES

IN PARTIAL FULFILLMENT OF THE REQUIREMENTS FOR THE

DEGREE OF MASTER OF SCIENCE

DEPARTMENT OF PHYSICS AND ASTRONOMY

CALGARY, ALBERTA

JANUARY, 1994

ISBN   0-315-93955-9

Canada

Name __DIANA PIGGOTT__

Dissertation Abstracts International is arranged by broad, general subject categories. Please select the one subject which most nearly describes the content of your dissertation. Enter the corresponding four-digit code in the spaces provided.

__ATMOSPHERIC SCIENCE__

SUBJECT TERM

| 0 | 6 | 0 | 8 |

U·M·I

SUBJECT CODE

Subject Categories

THE HUMANITIES AND SOCIAL SCIENCES

COMMUNICATIONS AND THE ARTS
Architecture 0729
Art History 0377
Cinema 0900
Dance 0378
Fine Arts 0357
Information Science 0723
Journalism 0391
Library Science 0399
Mass Communications 0708
Music 0413
Speech Communication 0459
Theater 0465

EDUCATION
General 0515
Administration 0514
Adult and Continuing 0516
Agricultural 0517
Art 0273
Bilingual and Multicultural 0282
Business 0688
Community College 0275
Curriculum and Instruction 0727
Early Childhood 0518
Elementary 0524
Finance 0277
Guidance and Counseling 0519
Health 0680
Higher 0745
History of 0520
Home Economics 0278
Industrial 0521
Language and Literature 0279
Mathematics 0280
Music 0522
Philosophy of 0998
Physical 0523

Psychology 0525
Reading 0535
Religious 0527
Sciences 0714
Secondary 0533
Social Sciences 0534
Sociology of 0340
Special 0529
Teacher Training 0530
Technology 0710
Tests and Measurements 0288
Vocational 0747

LANGUAGE, LITERATURE AND LINGUISTICS
Language
  General 0679
  Ancient 0289
  Linguistics 0290
  Modern 0291
Literature
  General 0401
  Classical 0294
  Comparative 0295
  Medieval 0297
  Modern 0298
  African 0316
  American 0591
  Asian 0305
  Canadian (English) 0352
  Canadian (French) 0355
  English 0593
  Germanic 0311
  Latin American 0312
  Middle Eastern 0315
  Romance 0313
  Slavic and East European 0314

PHILOSOPHY, RELIGION AND THEOLOGY
Philosophy 0422
Religion
  General 0318
  Biblical Studies 0321
  Clergy 0319
  History of 0320
  Philosophy of 0322
Theology 0469

SOCIAL SCIENCES
American Studies 0323
Anthropology
  Archaeology 0324
  Cultural 0326
  Physical 0327
Business Administration
  General 0310
  Accounting 0272
  Banking 0770
  Management 0454
  Marketing 0338
Canadian Studies 0385
Economics
  General 0501
  Agricultural 0503
  Commerce-Business 0505
  Finance 0508
  History 0509
  Labor 0510
  Theory 0511
Folklore 0358
Geography 0366
Gerontology 0351
History
  General 0578

Ancient 0579
Medieval 0581
Modern 0582
Black 0328
African 0331
Asia, Australia and Oceania 0332
Canadian 0334
European 0335
Latin American 0336
Middle Eastern 0333
United States 0337
History of Science 0585
Law 0398
Political Science
  General 0615
  International Law and
    Relations 0616
  Public Administration 0617
Recreation 0814
Social Work 0452
Sociology
  General 0626
  Criminology and Penology ... 0627
  Demography 0938
  Ethnic and Racial Studies 0631
  Individual and Family
    Studies 0628
  Industrial and Labor
    Relations 0629
  Public and Social Welfare 0630
  Social Structure and
    Development 0700
  Theory and Methods 0344
Transportation 0709
Urban and Regional Planning 0999
Women's Studies 0453

THE SCIENCES AND ENGINEERING

BIOLOGICAL SCIENCES
Agriculture
  General 0473
  Agronomy 0285
  Animal Culture and
    Nutrition 0475
  Animal Pathology 0476
  Food Science and
    Technology 0359
  Forestry and Wildlife 0478
  Plant Culture 0479
  Plant Pathology 0480
  Plant Physiology 0817
  Range Management 0777
  Wood Technology 0746
Biology
  General 0306
  Anatomy 0287
  Biostatistics 0308
  Botany 0309
  Cell 0379
  Ecology 0329
  Entomology 0353
  Genetics 0369
  Limnology 0793
  Microbiology 0410
  Molecular 0307
  Neuroscience 0317
  Oceanography 0416
  Physiology 0433
  Radiation 0821
  Veterinary Science 0778
  Zoology 0472
Biophysics
  General 0786
  Medical 0760

EARTH SCIENCES
Biogeochemistry 0425
Geochemistry 0996

Geodesy 0370
Geology 0372
Geophysics 0373
Hydrology 0388
Mineralogy 0411
Paleobotany 0345
Paleoecology 0426
Paleontology 0418
Paleozoology 0985
Palynology 0427
Physical Geography 0368
Physical Oceanography 0415

HEALTH AND ENVIRONMENTAL SCIENCES
Environmental Sciences 0768
Health Sciences
  General 0566
  Audiology 0300
  Chemotherapy 0992
  Dentistry 0567
  Education 0350
  Hospital Management 0769
  Human Development 0758
  Immunology 0982
  Medicine and Surgery 0564
  Mental Health 0347
  Nursing 0569
  Nutrition 0570
  Obstetrics and Gynecology .. 0380
  Occupational Health and
    Therapy 0354
  Ophthalmology 0381
  Pathology 0571
  Pharmacology 0419
  Pharmacy 0572
  Physical Therapy 0382
  Public Health 0573
  Radiology 0574
  Recreation 0575

Speech Pathology 0460
Toxicology 0383
Home Economics 0386

PHYSICAL SCIENCES

Pure Sciences
Chemistry
  General 0485
  Agricultural 0749
  Analytical 0486
  Biochemistry 0487
  Inorganic 0488
  Nuclear 0738
  Organic 0490
  Pharmaceutical 0491
  Physical 0494
  Polymer 0495
  Radiation 0754
Mathematics 0405
Physics
  General 0605
  Acoustics 0986
  Astronomy and
    Astrophysics 0606
  Atmospheric Science 0608
  Atomic 0748
  Electronics and Electricity 0607
  Elementary Particles and
    High Energy 0798
  Fluid and Plasma 0759
  Molecular 0609
  Nuclear 0610
  Optics 0752
  Radiation 0756
  Solid State 0611
Statistics 0463

Applied Sciences
Applied Mechanics 0346
Computer Science 0984

Engineering
  General 0537
  Aerospace 0538
  Agricultural 0539
  Automotive 0540
  Biomedical 0541
  Chemical 0542
  Civil 0543
  Electronics and Electrical 0544
  Heat and Thermodynamics ... 0348
  Hydraulic 0545
  Industrial 0546
  Marine 0547
  Materials Science 0794
  Mechanical 0548
  Metallurgy 0743
  Mining 0551
  Nuclear 0552
  Packaging 0549
  Petroleum 0765
  Sanitary and Municipal 0554
  System Science 0790
Geotechnology 0428
Operations Research 0796
Plastics Technology 0795
Textile Technology 0994

PSYCHOLOGY
General 0621
Behavioral 0384
Clinical 0622
Developmental 0620
Experimental 0623
Industrial 0624
Personality 0625
Physiological 0989
Psychobiology 0349
Psychometrics 0632
Social 0451

♲

Nom _____

Dissertation Abstracts International est organisé en catégories de sujets. Veuillez s.v.p. choisir le sujet qui décrit le mieux votre thèse et inscrivez le code numérique approprié dans l'espace réservé ci-dessous.

SUJET   CODE DE SUJET

Catégories par sujets

HUMANITÉS ET SCIENCES SOCIALES

COMMUNICATIONS ET LES ARTS
Architecture 0729
Beaux-arts 0357
Bibliothéconomie 0399
Cinéma 0900
Communication verbale 0459
Communications 0708
Danse 0378
Histoire de l'art 0377
Journalisme 0391
Musique 0413
Sciences de l'information 0723
Théâtre 0465

ÉDUCATION
Généralités 515
Administration 0514
Art 0273
Collèges communautaires 0275
Commerce 0688
Économie domestique 0278
Éducation permanente 0516
Éducation préscolaire 0518
Éducation sanitaire 0680
Enseignement agricole 0517
Enseignement bilingue et
  multiculturel 0282
Enseignement industriel 0521
Enseignement primaire. 0524
Enseignement professionnel 0747
Enseignement religieux 0527
Enseignement secondaire 0533
Enseignement spécial 0529
Enseignement supérieur 0745
Évaluation 0288
Finances 0277
Formation des enseignants 0530
Histoire de l'éducation 0520
Langues et littérature 0279

Lecture 0535
Mathématiques 0280
Musique 0522
Orientation et consultation 0519
Philosophie de l'éducation 0998
Physique 0523
Programmes d'études et
  enseignement 0727
Psychologie 0525
Sciences 0714
Sciences sociales 0534
Sociologie de l'éducation 0340
Technologie 0710

LANGUE, LITTÉRATURE ET LINGUISTIQUE
Langues
  Généralités 0679
  Anciennes 0289
  Linguistique 0290
  Modernes 0291
Littérature
  Généralités 0401
  Anciennes 0294
  Comparée 0295
  Médiévale 0297
  Moderne 0298
  Africaine 0316
  Américaine 0591
  Anglaise 0593
  Asiatique 0305
  Canadienne (Anglaise) 0352
  Canadienne (Française) 0355
  Germanique 0311
  Latino-américaine 0312
  Moyen-orientale 0315
  Romane 0313
  Slave et est-européenne 0314

PHILOSOPHIE, RELIGION ET THÉOLOGIE
Philosophie 0422
Religion
  Généralités 0318
  Clergé 0319
  Études bibliques 0321
  Histoire des religions 0320
  Philosophie de la religion 0322
Théologie 0469

SCIENCES SOCIALES
Anthropologie
  Archéologie 0324
  Culturelle 0326
  Physique 0327
Droit 0398
Économie
  Généralités 0501
  Commerce-Affaires 0505
  Économie agricole 0503
  Économie du travail 0510
  Finances 0508
  Histoire 0509
  Théorie 0511
Études américaines 0323
Études canadiennes 0385
Études féministes 0453
Folklore 0358
Géographie 0366
Gérontologie 0351
Gestion des affaires
  Généralités 0310
  Administration 0454
  Banques 0770
  Comptabilité 0272
  Marketing 0338
Histoire
  Histoire générale 0578

Ancienne 0579
Médiévale 0581
Moderne 0582
Histoire des noirs 0328
Africaine 0331
Canadienne 0334
États-Unis 0337
Européenne 0335
Moyen-orientale 0333
Latino-américaine 0336
Asie, Australie et Océanie 0332
Histoire des sciences 0585
Loisirs 0814
Planification urbaine et
  régionale 0999
Science politique
  Généralités 0615
  Administration publique 0617
  Droit et relations
    internationales 0616
Sociologie
  Généralités 0626
  Aide et bien-être social 0630
  Criminologie et
    établissements
    pénitentiaires 0627
  Démographie 0938
  Études de l' individu et
    de la famille 0628
  Études des relations
    interethniques et
    des relations raciales 0631
  Structure et développement
    social 0700
  Théorie et méthodes. 0344
  Travail et relations
    industrielles 0629
Transports 0709
Travail social 0452

SCIENCES ET INGÉNIERIE

SCIENCES BIOLOGIQUES
Agriculture
  Généralités 0473
  Agronomie. 0285
  Alimentation et technologie
    alimentaire 0359
  Culture 0479
  Élevage et alimentation 0475
  Exploitation des péturages ... 0777
  Pathologie animale 0476
  Pathologie végétale 0480
  Physiologie végétale 0817
  Sylviculture et faune 0478
  Technologie du bois 0746
Biologie
  Généralités 0306
  Anatomie 0287
  Biologie (Statistiques) 0308
  Biologie moléculaire 0307
  Botanique 0309
  Cellule 0379
  Écologie 0329
  Entomologie 0353
  Génétique 0369
  Limnologie 0793
  Microbiologie 0410
  Neurologie 0317
  Océanographie 0416
  Physiologie 0433
  Radiation 0821
  Science vétérinaire 0778
  Zoologie 0472
Biophysique
  Généralités 0786
  Medicale 0760

SCIENCES DE LA TERRE
Biogéochimie 0425
Géochimie 0996
Géodésie 0370
Géographie physique 0368

Géologie 0372
Géophysique 0373
Hydrologie 0388
Minéralogie 0411
Océanographie physique 0415
Paléobotanique 0345
Paléoécologie 0426
Paléontologie 0418
Paléozoologie 0985
Palynologie 0427

SCIENCES DE LA SANTÉ ET DE L'ENVIRONNEMENT
Économie domestique 0386
Sciences de l'environnement 0768
Sciences de la santé
  Généralités 0566
  Administration des hipitaux .. 0769
  Alimentation et nutrition 0570
  Audiologie 0300
  Chimiothérapie 0992
  Dentisterie 0567
  Développement humain 0758
  Enseignement 0350
  Immunologie 0982
  Loisirs 0575
  Médecine du travail et
    thérapie 0354
  Médecine et chirurgie 0564
  Obstétrique et gynécologie... 0380
  Ophtalmologie 0381
  Orthophonie 0460
  Pathologie 0571
  Pharmacie 0572
  Pharmacologie 0419
  Physiothérapie 0382
  Radiologie 0574
  Santé mentale 0347
  Santé publique 0573
  Soins infirmiers 0569
  Toxicologie 0383

SCIENCES PHYSIQUES
Sciences Pures
Chimie
  Généralités 0485
  Biochimie 487
  Chimie agricole 0749
  Chimie analytique 0486
  Chimie minérale 0488
  Chimie nucléaire 0738
  Chimie organique 0490
  Chimie pharmaceutique 0491
  Physique 0494
  PolymÇres 0495
  Radiation 0754
Mathématiques 0405
Physique
  Généralités 0605
  Acoustique 0986
  Astronomie et
    astrophysique 0606
  Electronique et électricité 0607
  Fluides et plasma 0759
  Météorologie 0608
  Optique 0752
  Particules (Physique
    nucléaire) 0798
  Physique atomique 0748
  Physique de l'état solide 0611
  Physique moléculaire 0609
  Physique nucléaire 0610
  Radiation 0756
Statistiques 0463

Sciences Appliqués Et Technologie
Informatique 0984
Ingénierie
  Généralités 0537
  Agricole 0539
  Automobile 0540

Biomédicale 0541
Chaleur et ther
  modynamique 0348
Conditionnement
  (Emballage) 0549
Génie aérospatial 0538
Génie chimique 0542
Génie civil 0543
Génie électronique et
  électrique 0544
Génie industriel 0546
Génie mécanique 0548
Génie nucléaire 0552
Ingénierie des systèmes 0790
Mécanique navale 0547
Métallurgie 0743
Science des matériaux 0794
Technique du pétrole 0765
Technique minière 0551
Techniques sanitaires et
  municipales 0554
Technologie hydraulique 0545
Mécanique appliquée 0346
Géotechnologie 0428
Matières plastiques
  (Technologie) 0795
Recherche opérationnelle 0796
Textiles et tissus (Technologie) ... 0794
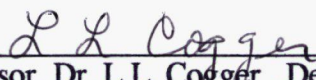
PSYCHOLOGIE
Généralités 0621
Personnalité 0625
Psychobiologie 0349
Psychologie clinique 0622
Psychologie du comportement ... 0384
Psychologie du développement .. 0620
Psychologie expérimentale 0623
Psychologie industrielle 0624
Psychologie physiologique 0989
Psychologie sociale 0451
Psychométrie 0632

✷
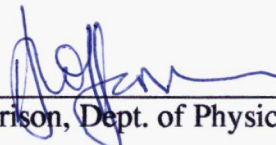
THE UNIVERSITY OF CALGARY

FACULTY OF GRADUATE STUDIES
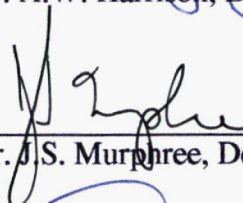
The undersigned certify that they have read, and recommend to the Faculty of Graduate Studies for acceptance, a thesis entitled "A Study of Visible Atomic Oxygen Airglow over Arecibo" submitted by Diana Helen Piggott in partial fulfillment of the requirements for the degree of Master of Science.
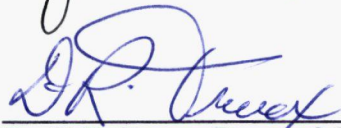
_____
Supervisor, Dr. L.L. Cogger , Dept. of Physics and Astronomy

_____
Dr. A.W. Harrison, Dept. of Physics and Astronomy

_____
Dr. J.S. Murphree, Dept. of Physics and Astronomy

_____
Dr. D.R. Truax, Dept. of Chemistry

8 April 1994
Date

ii

Abstract

Ionospheric data and airglow intensities were obtained from the Arecibo Observatory's incoherent scatter radar facility and airglow photometers, respectively for selected nights of 1971, 1976 and 1985. Electron densities and ion temperatures determined from radar signals were used, with the MSIS-83 model thermosphere, to calculate expected airglow brightnesses at 6300 Å and 5577 Å emanating from atomic oxygen in the F region. Dissociative recombination of O_2^+ ions is the major source of these emission lines. Two different sets of reaction rate coefficients reproduced observed 6300 Å intensities quite well under most conditions, under the assumption of photochemical equilibrium. The quantum efficiency of $O(^1S)$ production was found to lie in the range 0.03–0.1 per dissociative recombination, in agreement with other recent research. Atmospheric tides were found to be a likely factor in the red line hysteresis effect. Observations during a large geomagnetic disturbance revealed complex wave structure, implying substantial thermospheric composition changes.

Acknowledgements

Contents

List of Tables

List of Figures

Chapter 1

Introduction

The typical light of the night sky arises from many sources, including the stellar background, scattering of sunlight by interplanetary gas and dust ("zodiacal light"), and diffuse galactic light. There is in addition a terrestrial contribution, consisting of diffuse emissions from the Earth's upper atmosphere, which is now known as airglow. Airglow is distinguished from the more familiar aurora both by the physical processes involved and by its distribution in time and space. While aurorae are chiefly observed at high latitudes in times of geomagnetic disturbance, airglow is a global phenomenon which is present at all times. Due to the faintness and relative uniformity of the latter, it was not properly discovered until this century. The first emission to be studied was the green line at 5577 Å, which was already well known from the aurora. Interesting reviews of the early work on airglow may be found in Chamberlain (1961), McCormac (1967) and Bates (1978).

The terrestrial origin of this component of the night light was established photometrically in 1909 by Yntema, who named the phenomenon Earthlight. This work was confirmed and extended in the following two decades by investigators such as Slipher, van Rhijn and Babcock. The fourth Lord Rayleigh studied intensity variations with time, in various parts of the spectrum, which he correlated with sunspots and geomagnetic activity. In 1930 he measured the absolute intensity of the green line (5577 Å) in number of transitions per second in a line of sight column, which led to the naming of the associated photometric unit after him. An illuminating state of the art lecture on the upper atmosphere was given in 1931 by Sydney Chapman, who proposed recombination of particles ionized or dissociated by solar ultraviolet (uv) radiation as a possible source of airglow emissions (Chapman,

1931). In the 1920s and 1930s, oxygen was identified as the source of the green line, and oxygen red lines at 6300 and 6364 Å and the sodium D lines were resolved and identified. The 1940s and 1950s saw the discovery of O_2 and OH molecular bands, the blue line of atomic nitrogen (5200 Å), and a weak $H\alpha$ emission. Many more features have been added to this list, particularly with space-age observations of airglow in the daytime ("dayglow", as opposed to "nightglow"). Space probes have also been able to measure airglow emanating from the atmospheres of other planets in our system.

On the theoretical side, Bates first postulated dissociative recombination of molecular ions as a possible source of the nightglow in 1946, and in 1956 suggested the sequence $O^+ + O_2 \rightarrow O_2^+ + O$ leading to $O_2^+ + e \rightarrow O^* + O^*$ for the production of excited oxygen atoms. In an entertaining article, Bates (1988) describes how the theory of recombination in the ionosphere developed. In the 1950s, dissociative recombination was accepted as the source of most 6300 Å nightglow, and Barbier's famous formula relating the intensity at 6300 Å to ionospheric F-region parameters appeared (Barbier, 1957). Rocket measurements in the 1950s and 1960s led to a tremendous increase in knowledge of the upper atmosphere. In particular, the concentrations of ionic and neutral species were measured, and altitudes of maximum emission regions were located for various sources. Thus the origin of the oxygen red line was definitely fixed in the F region along with a small fraction of the green line, of which the major portion originates in the E region. This aided the identification of reactions responsible for atomic oxygen emissions (*e.g.*, Peterson, 1967, Dalgarno and Walker, 1964). Finally, Wickwar, Cogger and Carlson (1974) were able to show that, under most quiet conditions, the intensity of the 6300 Å nightglow may be completely attributed to dissociative recombination of O_2^+. Improvements to theoretical calculations since have been mainly due to recalculation and laboratory measurements of the relevant reaction rate coefficients (see Bates, 1978, for

examples of their evolution) and frequently updated models of neutral atmosphere composition.

Photometric studies of airglow have been made from ground-based observations and from balloon, rocket and satellite experiments. These have revealed variations of intensity with altitude, latitude and longitude, along with a great variety of temporal variations (McCormac, 1967). Spatial variations result from a combination of geographic and geomagnetic influences, especially insolation and transport. One somewhat unexpected feature was the appearance of 6300 Å intensity maxima centred near ±15° geomagnetic latitude, related to the Appleton anomaly (see sections 2.3, 2.5) of F-region electron densities. Bright red arcs are also observed at higher latitudes (~53° ± 8°), with N–S dimensions of hundreds of km, and thousands of km E–W. These have been called sub-auroral red, or SAR, arcs, and are excited at higher altitudes (~300 – 700 km) than are typical red line emissions. The green line is not similarly enhanced, indicating a low energy source of excitation (Nagy *et al.*, 1970; Rees and Roble, 1975).

On a diurnal scale, the dayglow tends to be 2–3 orders of magnitude brighter than the nightglow, which falls off exponentially with time after sunset as the ionosphere decays through recombination. However, several enhancements of the nightglow have been observed. In the winter months, post-twilight and pre-dawn increases in red line brightness have been attributed to excitation by photoelectrons streaming in along magnetic field lines from the conjugate point, where the sun shines for a longer period (Carlson, 1965; Wickwar, 1971). Post-midnight enhancements are often quite considerable, and are related to changes in neutral wind patterns allowing the F layer to descend, resulting in faster recombination (Nelson and Cogger, 1971). Other variations may be due to waves travelling through the thermosphere from polar regions.

Airglow intensities show a marked variation with solar cycle and solar activity, being on average much higher (up to an order of magnitude) at solar cycle maximum than at solar minimum. During geomagnetic storms, however, after an initial period of activity, F-region electron densities are suppressed, resulting in a lowering of red line intensities. Composition changes occurring during storms also affect airglow emissions; this matter will be discussed briefly in section 4.9.

Two significant advances in the study of terrestrial airglow were made in the 1970s. In the first, photometric airglow observations were compared with calculated model intensities using ionospheric data from an incoherent backscatter radar system (Cogger *et al.*, 1974). Results of such comparisons contribute to our understanding of both the neutral atmosphere and the ionosphere. Secondly, the Atmosphere Explorer series of satellites was launched with 14 interrelated instruments to collect thermospheric and ionospheric data, including the photometers of the Visible Airglow Experiment (VAE). Some new determinations of reaction rate coefficients used results from these measurements (Hays *et al.*, 1978), and provided grist for the mill of investigators in the 1980s (see review by Hays *et al.*, 1988).

Satellite experiments have two major advantages over those performed from the ground. *In situ* measurements of neutral and ionic composition vastly reduce i) the reliance on models and ii) the number of rate coefficients needed for calculations. Also, airglow emission profiles eliminate the line of sight column integration inherent in ground-based observations. In 1980, Cogger *et al.* used rate coefficients determined from Atmosphere Explorer satellite data, together with ground-based incoherent backscatter radar measurements of ionospheric electron densities and temperatures, to model red line nightglow intensities measured by ground-based photometers. Two major discrepancies were found: the calculated intensities were larger than the photometer measurements by

factors of more than two, and a loop structure appeared in several of the calculated *vs.* observed brightness plots ("red line hysteresis", Cogger *et al.*, 1980). These discrepancies provided the motivation for the present study. The first indicates the need to re-examine rate coefficients and thermospheric model densities, while the second suggests that it may be necessary to consider transport processes in the calculation.

For these purposes, simultaneous ionospheric radar and photometer data taken in 1985 were obtained, and combined with the 1971 and 1976 data of Cogger *et al.* to provide fairly broad coverage of solar maximum and minimum conditions. The photochemical model used in the present work incorporates some recent determinations of rate coefficients provided by several investigators, and a new model atmosphere (MSIS-83, Hedin, 1983), to obtain temperature and composition profiles of the neutral atmosphere. Recent work on the relevant chemical processes has been done by Link *et al.* (1981), Schmitt *et al.* (1981), Abreu *et al.* (1986), and briefly reviewed by Sharp (1986). Since then, papers by Fesen and Abreu (1987), Yee and Dalgarno (1987), Guberman (1987,1988), Yee (1988) and Link and Cogger (1988) have added new ideas and revised rate coefficients to the repertoire. These will be further discussed in Chapters 4 and 5.

Chapter 2 describes the present understanding of physical processes in the ionosphere, beginning with the formation of layers of ionization and leading to photochemical processes responsible for night-time emissions at 6300 Å and 5577 Å in the F region. This is followed by a brief discussion of thermospheric dynamics.

Chapter 3 provides a description of the equipment at Arecibo used to obtain the data for the analysis. It also includes a description of the basic techniques of incoherent scatter radar, and concludes with a detailed summary of the data obtained.

Details of data analysis and various approaches to modelling the results are found in Chapter 4. Interesting features in the data are discussed, as well as the physical validity and implications of the models employed.

Finally, Chapter 5 summarizes the results of this investigation, relating these to the conclusions of other researchers, and suggests further work to enhance our understanding of the low-latitude ionosphere.

Chapter 2

The Ionosphere

2.1 History

Although in the last century Gauss, Lord Kelvin and Stewart all suggested that electric currents in the upper atmosphere may have been responsible for observed diurnal variations in the earth's magnetic field (Bauer, 1973), the beginning of the twentieth century marks the real beginning of ionospheric physics. Marconi's trans-Atlantic radio transmissions of 1901 inspired Kennelly (USA), Heaviside (UK) and Nagaoko (Japan) independently to postulate the existence of a permanent conducting layer in the upper atmosphere, which came to be known as the Kennelly-Heaviside layer. Its presence was experimentally confirmed in the mid-1920s by Appleton and Barnett (UK), who named the "E-layer" for the electric vector of reflected radio waves (Bauer, 1973), and by Breit and Tuve (USA), who performed the first radar pulse sounding of the atmosphere (Giraud and Petit, 1978). This technique, the ionosonde, would be the major source of ionospheric data for the next thirty years.

In 1925, Appleton found and named the "D" and "F" layers, and the whole system of layers was later named the ionosphere by Watson-Watt. Figure 2.1 shows approximate locations of the various regions, and typical (free) electron density distributions. The F-region is subdivided into F_1 (maximum ion production) and F_2 (maximum ion/electron density), and the lower portion of the D region is sometimes referred to as the "C-layer" for the role played by cosmic rays.
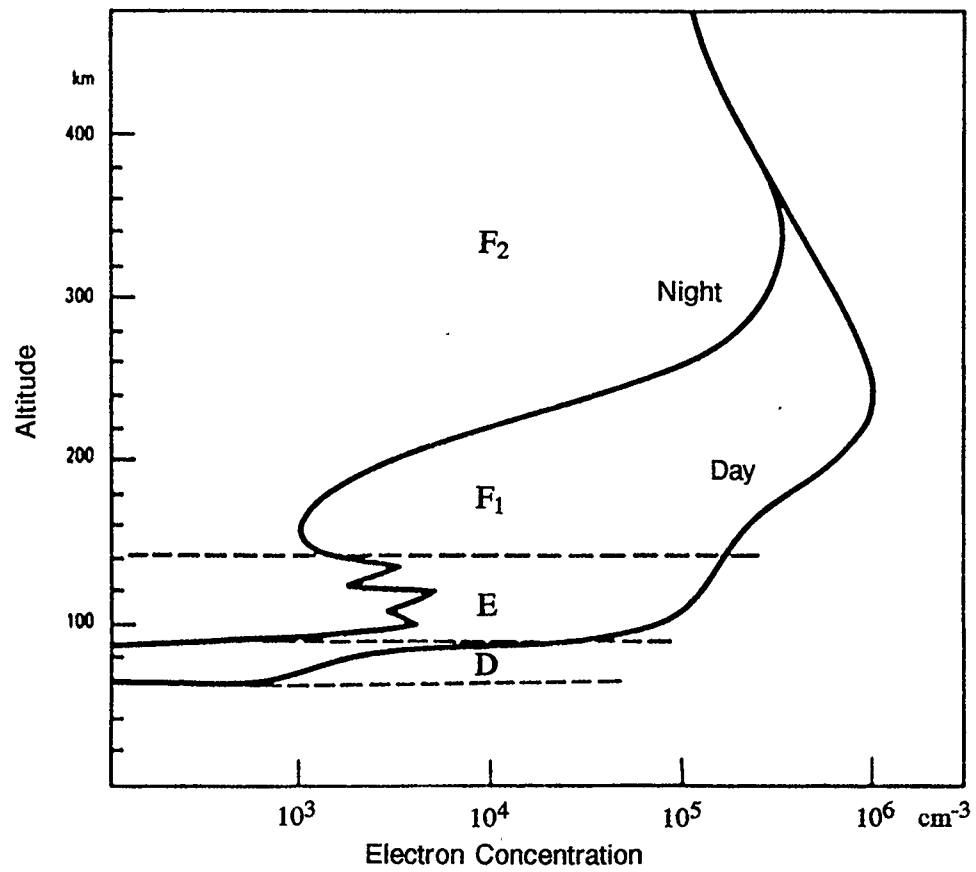
Figure 2.1 Regions of the terrestrial ionosphere and representative free
electron concentrations

Vertical profiles of plasma density in the ionosphere were first measured by radio sounding, using variable frequency radar to scan near the local plasma frequency, looking for total reflection of the radio waves (f ~ MHz). In 1958, the technique of incoherent scatter, or Thomson scatter, was established, in which radio waves of much higher frequency (f ~ $10^2 - 10^3$ MHz) are backscattered due to random thermal motions of the plasma. This method permits simultaneous measurement of several ionospheric parameters, but requires a powerful transmitter (P ~ megawatts). The backscattered power is proportional to the electron density, and the spectrum of the returned signal depends on electron and ion temperatures, ion composition and bulk plasma motion. From these can be derived information about electrical conductivities, and behaviour of the neutral component of the upper atmosphere (thermosphere).

At present, there are half a dozen incoherent scatter radar installations, covering a wide range of latitudes, which monitor local, and to some extent global, behaviour of the upper atmosphere. See, for example, the work by Blanc (1979), Evans (1978), Evans *et al.* (1979), and Burnside (1984).

2.2 Formation of Ionized Layers

Ionization is produced in the earth's upper atmosphere by solar radiation of ultraviolet and X-ray wavelengths, energetic particles and meteor impact. Apart from the contribution of cosmic rays to the lower D region (< 75 km), the absorption of solar radiation by neutral gases is the dominant ion production mechanism.
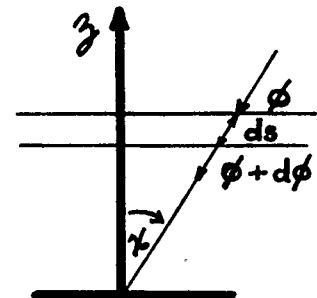
Figure 2.2 Geometry of absorbing atmosphere

As illustrated in figure 2.2, let $\phi(\lambda)$ = incident radiation flux for a given wavelength λ, (ϕ_∞ = flux outside atmosphere), n^i = concentration of ith species of neutral gas, $\sigma_a^i(\lambda)$ = absorption cross-section of ith species, ds = path length; then the change in flux over the path length ds is given by

$$d\phi = - \sum_i n^i \sigma_a^i(\lambda) \phi(\lambda) ds. \qquad (2.2.1)$$

With the definition of optical depth,

$$\tau(z,\lambda) = \sum_i \sigma_a^i(\lambda) \int_z^\infty n^i ds, \qquad (2.2.2)$$

(2.2.1) may be integrated to obtain the remaining flux at height z:

$$\phi(z,\lambda) = \phi_\infty(\lambda) e^{-\tau(z,\lambda)}. \qquad (2.2.3)$$

Absorption of the given wavelength will be greatest in the region near $\tau = 1$, so the altitude of maximum absorption may be estimated with some knowledge of absorption cross-sections and the height distribution of n^i. Sample models of thermospheric structure and composition are illustrated in figures 2.3 and 2.4. Table 2.1 and figure 2.5 give absorption data for the terrestrial ionosphere.

The rate of ionization of the ith species by radiation of wavelength λ is proportional to the remaining flux at λ and the ionization cross section σ_I^i :

$$q_i(z,\lambda) = n^i(z) \sigma_I^i(\lambda) \phi_\infty(\lambda) e^{-\tau(z,\lambda)}. \qquad (2.2.4)$$

From (2.2.4) the shape of the ionization production layer may be determined, with appropriate assumptions for n^i and τ. The simplest assumptions of a single constituent,
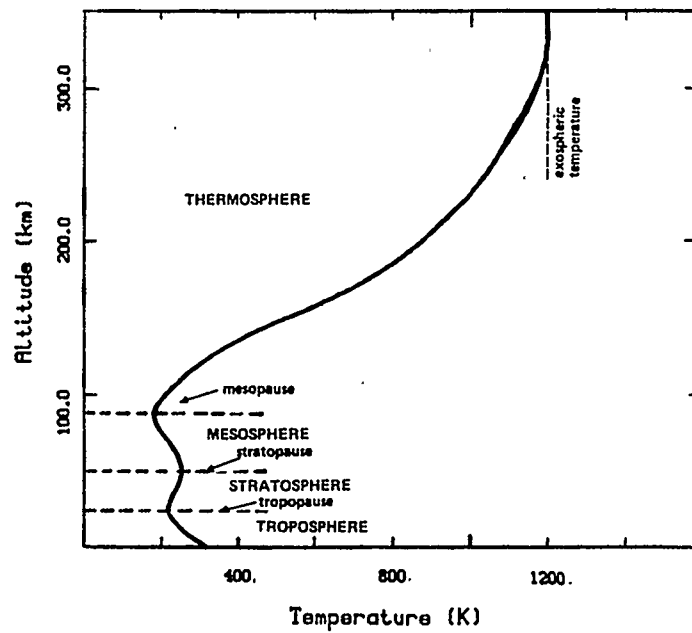
Figure 2.3 Thermal structure of atmosphere and atmospheric regions
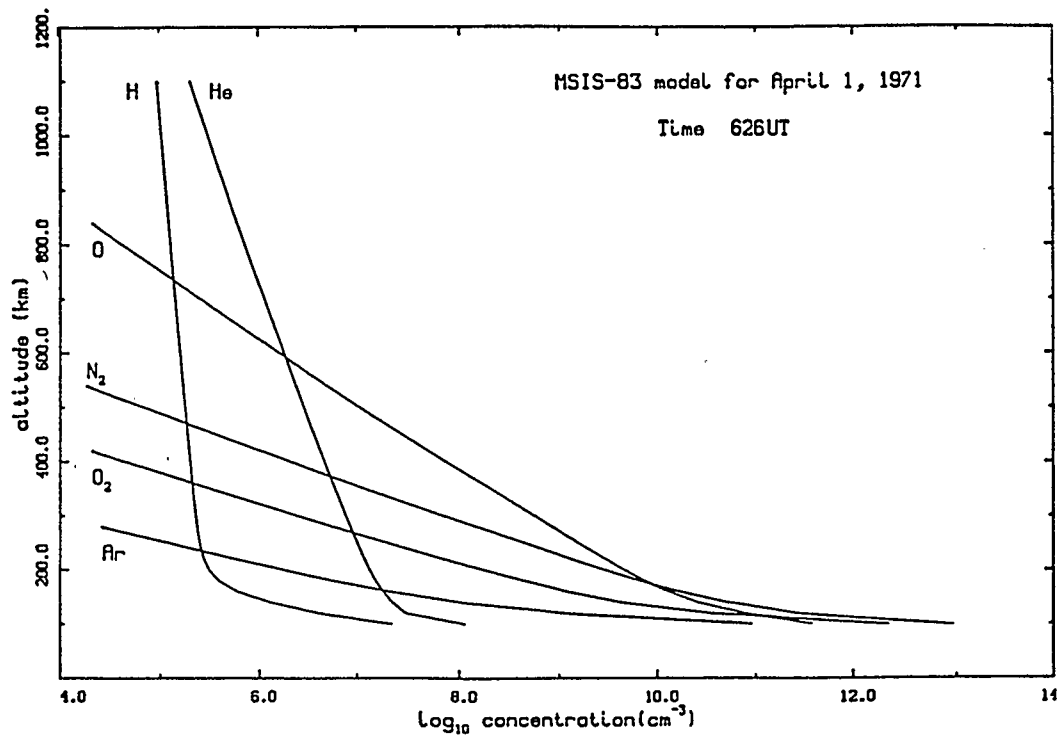
Figure 2.4 Composition of the thermosphere (MSIS-83 sample output)
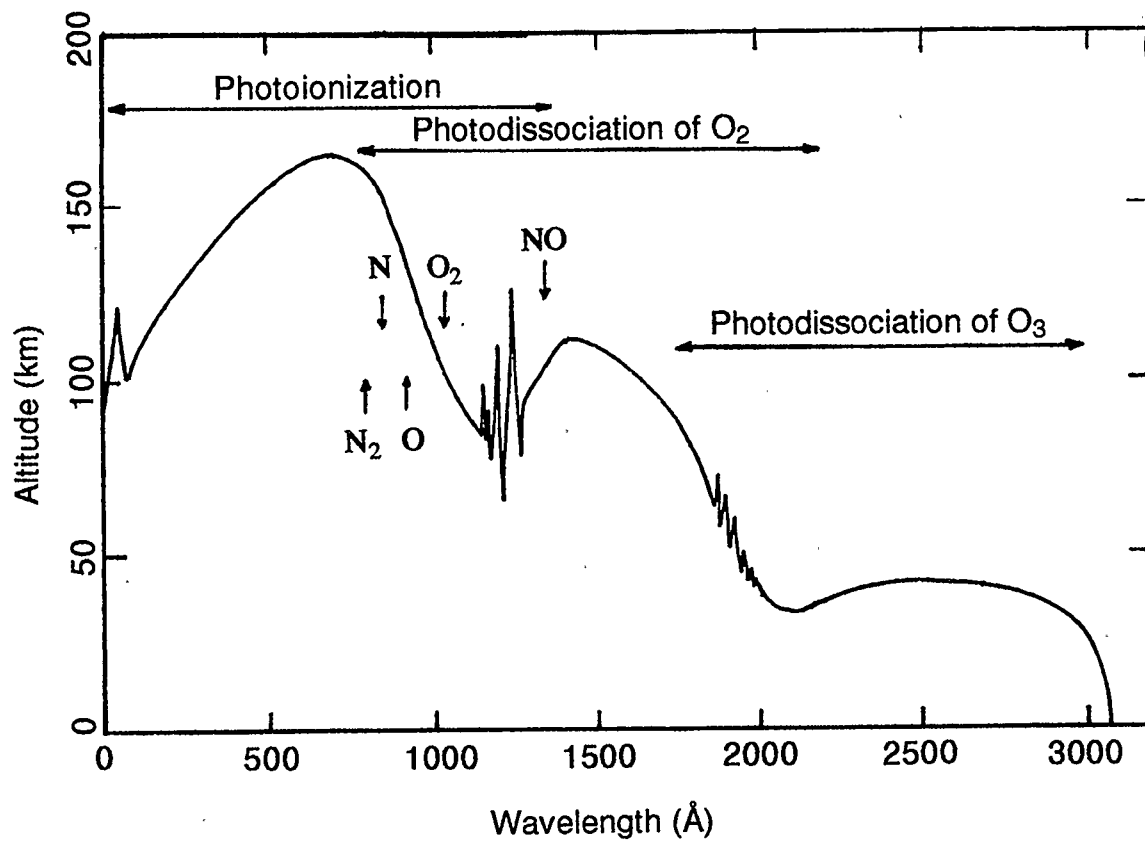
Figure 2.5 Altitude of unit optical depth for solar zenith angle = 0.

The arrows mark threshold photoionization wavelengths of the

indicated species (Giraud and Petit, 1978, p. 13)

isothermal, plane-parallel atmosphere of constant scale height (H), lead to the classical

Chapman production function (for a single wavelength):

$$q = q_m \exp\{ 1 - \frac{h}{H} - \sec\chi \ e^{-h/H} \}$$ (2.2.5)

where χ = solar zenith angle, and h is the altitude measured relative to $\tau = 1$, $\chi = 0$. q_m is

the maximum production rate, which occurs at unit optical depth:

$$q_m = \frac{\sigma_I \phi_\infty \ e^{-1} \cos\chi}{\sigma_a H}$$ (2.2.6)

These approximations are quite invalid for large solar zenith angles.

Table 2.1 Absorption of Radiation in Ionospheric Regions

Region	Absorption cross-section	Wavelengths absorbed	Absorbing species
D	$\sigma_a \lesssim 10^{-19}$ cm^2	uv, > 1750 Å	O_3
		X-rays, < 10 Å	O_2, N_2
		Lyman-α, 1216 Å	NO
E	$\sigma_a \lesssim 5 \times 10^{-18}$ cm^2	X-rays, 10-100 Å	O, O_2, N_2
		uv, > 800 Å	O_2
F	$\sigma_a \lesssim 10^{-17}$ cm^2	100-800 Å	O, O_2, N_2

For charge neutrality, the number density of ions (n_i) and of electrons (n_e) must be equal.

For a single ionic species we may write $n_e = n_i = n$. Ionization is lost directly through

recombination ($X^+ + e \rightarrow X^*$), or indirectly through charge exchange

($X^+ + Y \rightarrow X + Y^+$) followed by recombination. The former follows a square loss law:

$$\frac{dn_i}{dt} = -\alpha n_i n_e = -\alpha n_e^2 \qquad (2.2.7)$$

with a characteristic time $\tau_c = \frac{1}{\alpha n_e}$, whereas the latter (charge exchange) has a linear loss law:

$$\frac{dn_i}{dt} = -\beta n_i = -k[Y]n_i \qquad (2.2.8)$$

with $\tau_c = \frac{1}{\beta} = \frac{1}{k[Y]}$ ([Y] = concentration of neutral species).

The vertical distribution of ionization can be derived assuming chemical equilibrium (production = loss of ionization). For a Chapman production function, with losses through direct recombination, this leads to $q = \alpha n_e^2$, and an electron density profile called a Chapman layer:

$$n_e = \left(\frac{q_m}{\alpha}\right)^{1/2} \exp[\tfrac{1}{2}\{1 - \frac{h}{H} - \sec\chi\ e^{-h/H}\}]. \qquad (2.2.9)$$

The E and F_1 regions each correspond quite closely to this form, but in the F_2 region, charge exchange becomes the dominant loss mechanism, and chemical equilibrium then leads to $q = \beta n_e$, with β a decreasing function of altitude. This is a so-called "Bradbury" layer, in which n_e increases above the height of maximum ion production, as seen in the lower F_2 region, and in the D region.

Diffusion also becomes important in the F_2 region, and high above the peak of the layer the electron density drops off as $e^{-h/2H}$. The F_2 peak itself is determined by both chemical and diffusive processes. The position of maximum electron/ion concentration (h_{max}) occurs where the characteristic time constants of the two processes are roughly equal, i.e.,

$\tau_c \sim \tau_D$, where $\tau_c = \frac{1}{\beta}$ and $\tau_D = H_D^2/D_a$ (H_D = plasma [ambipolar] scale height;

D_a = ambipolar diffusion coefficient, for ions and electrons diffusing together). The electron density at the peak is given by $n_{max} = \dfrac{q(h_{max})}{\beta(h_{max})}$.

At night, production becomes negligible and the D and F_1 layers all but disappear. Cosmic rays and energetic particles maintain a low level of ionization in the D region, whereas resonantly scattered uv radiation (*e.g.* Lyman-α and Lyman-β) are thought responsible for the nocturnal E layer.

In the F region, recombination is to some extent balanced by downward diffusion of plasma, so that substantial levels of ionization are maintained through the night. A fairly simple one-dimensional model for the nocturnal F region gives:

$$\frac{\partial n_e}{\partial t} = -\beta(z)n_e + \frac{\partial}{\partial z}\left\{D(z)\left[\frac{\partial n_e}{\partial z} + \frac{n_e}{2H}\right]\right\}. \tag{2.2.10}$$

With $\beta(z) = \beta_0\, e^{-(z-z_0)/H}$ and $D(z) = D_0\, e^{(z-z_0)/H}$, (2.2.10) becomes

$$\frac{\partial n_e}{\partial t} = D_0\, e^{(z-z_0)/H}\left\{\frac{\partial^2 n_e}{\partial z^2} + \frac{3}{2H}\frac{\partial n_e}{\partial z}\right\} + n_e\left\{\frac{D_0 e^{(z-z_0)/H}}{2H^2} - \beta_0\, e^{-(z-z_0)/H}\right\} \tag{2.2.11}$$

This give rise to solutions of the form (Chamberlain and Hunten, 1987)

$$n_e(z,t) = \sum_j n_j(z)e^{-\lambda_j t} \tag{2.2.12}$$

the so-called "night stationary layers", which retain their shape and height of peak density. In reality, neutral winds play a large role in the nocturnal F region through ion-neutral collisions, and the actual behaviour of the layer is quite different from the above situation (see section 2.5). However, for undisturbed conditions, the electron density profiles may still be represented by a Chapman-like distribution of the form:

$$n_e(z) = a_0\, \exp\left[a_1\left\{1 - \frac{z-z_0}{H} - a_2 e^{-(z-z_0)/H}\right\}\right] \tag{2.2.13}$$

with

$$H = H_o + \beta(z-z_o)$$

$$h_{max} = z_o + \frac{H_o \log a_2}{1 - \beta \log a_2}$$

$$(n_e)_{max} = a_o \exp(-a_1 \log a_2) \qquad \text{(Burnside, 1984)}.$$

2.3 Characteristics of the F Region

The peak electron density varies from $\sim 10^6$ cm^{-3} during the day to $\sim 10^5$ cm^{-3} at night, and increases with solar activity. The height of the peak (F_2) usually falls in the range 200 to 450 km, being higher at night and in winter. It is higher over the equator than at midlatitudes, and the height increases with solar activity.

There are a number of anomalous characteristics, by which is meant departures from the simple Chapman layer behaviour, mostly due to dynamical processes. The maximum electron density is actually greater in winter than in summer, and climbs to maximum values in March and October, with minima in July and January, being lower in July than January. During daytime, there is a minimum over the (magnetic) dip equator, with maxima near dip latitudes $\pm 18°$, known as the geomagnetic Appleton anomaly, which diminishes at night.

2.4 F-Region Photochemistry

Daytime absorption of solar ultraviolet radiation in the F region forms principally N_2^+, O^+ and O_2^+, but O_2^+ and especially N_2^+ are lost quickly to recombination and charge exchange reactions, thus the major ions present are different from the initial ones. See figure 2.6 for an example of measured ion abundances in the F region. Above about 200 km, O^+ is the
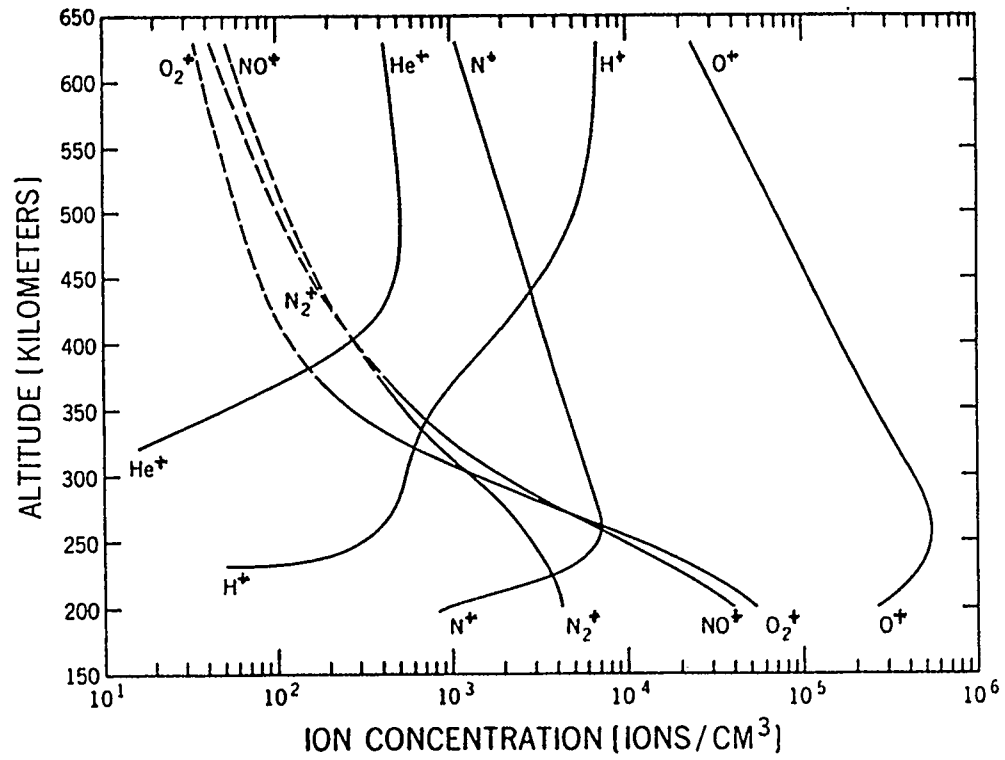
Figure 2.6 F region ion composition from rocket-borne mass spectrometer
(Brinton *et al.*, 1969)

dominant ion, with H^+ and He^+ becoming important at much higher altitudes. Table 2.2 shows the types of reactions involving ions which are important to the ionosphere. Atomic ions tend to recombine very slowly, and instead are lost through charge exchange reactions.

<u>Table 2.2 Ion Chemistry</u>

Reaction Type	Process	Significant Region
Radiative recombination	$X^+ + e \rightarrow X* + h\nu$	Interplanetary Space
Dissociative recombination	$XY^+ + e \rightarrow XY*$ $\rightarrow X + Y + h\nu$	all
Ion-ion recombination	$X^+ + Y^- \rightarrow X* + Y + \Delta E$	D region
Charge transfer (a) (b) dissociative (c) resonant (symmetric) (d) resonant (asymmetric) ("accidentally")	$X^+ + Y \rightarrow X + Y^+ + \Delta E$ $X^+ + YZ \rightarrow Y^+ + Z + X$ $X^+ + X \rightarrow X + X^+$ ($\Delta E = 0$) $X^+ + Y \rightleftarrows Y^+ + X$ (ΔE very small)	all
Ion-atom interchange	$X^+ + YZ \rightarrow XY^+ + Z$	all
(XY^+ then subject to dissociative recombination)		

Important reactions in the F region are the following:

1. Charge transfer $\quad\quad O^+ + H \rightleftarrows H^+ + O \quad\quad$ (asymmetric resonant)

$$N_2^+ + O \rightarrow O^+ + N_2$$
$$N_2^+ + O_2 \rightarrow O_2^+ + N_2$$
major sinks for N_2^+

$$O^+ + O_2 \rightarrow O_2^+ + O$$

$$\left. \begin{array}{l} \\ \\ \end{array} \right\} \quad \text{major sinks for } O^+$$

2. Ion-atom interchange $\quad O^+ + N_2 \rightarrow NO^+ + N$

$$N_2^+ + O \rightarrow NO^+ + N \qquad \text{major sink for } N_2^+$$

$$O_2^+ + N \rightarrow NO^+ + O$$

3. Dissociative recombination $\quad O_2^+ + e \rightarrow O + O + 6.96 \text{ eV}$

$$NO^+ + e \rightarrow N + O + 2.76 \text{ eV}$$
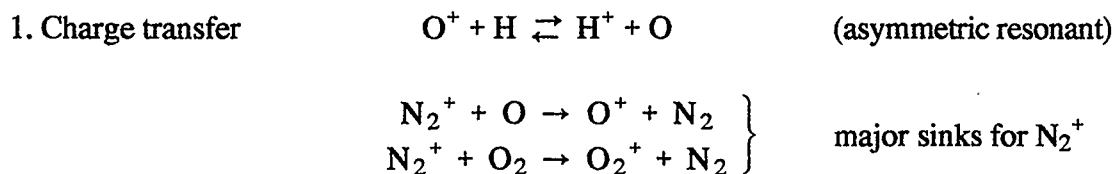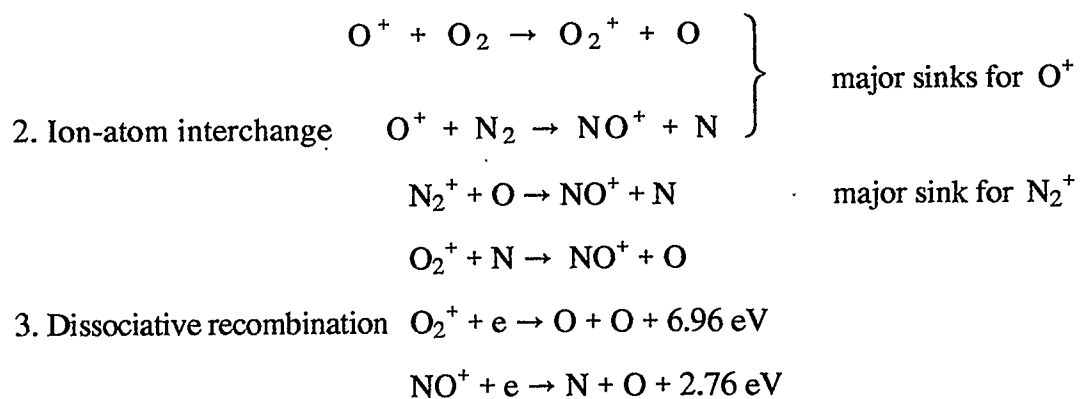
In particular, the dissociative recombination of O_2^+ is the primary source of F region airglow at 6300 Å and 5577 Å. NO^+ is considered an unlikely source due to non-conservation of spin (Dalgarno and Walker, 1964). The airglow in question is emitted by atomic oxygen in excited metastable states (see figure 2.7).
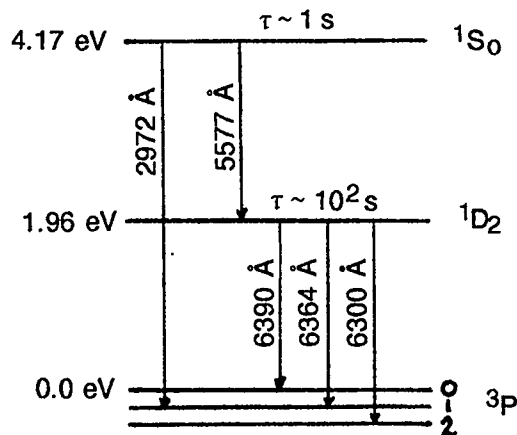
Figure 2.7 Forbidden transitions of atomic oxygen

Due to its relatively long lifetime, oxygen in the ^1D state is likely to be collisionally de-excited before it can emit. This is known as quenching, primarily a result of interaction with N_2, but O_2, O, and electrons may also contribute to the effect.

A simple photochemical model for these visible emissions equates production and loss terms for $O(^1D)$, $O(^1S)$ and O_2^+ for a steady-state, equilibrium situation. Information about thermospheric and ionospheric composition may then be used to calculate expected emission rates, for comparison with measured intensities. Details of the method may be found in chapter 4.

2.5 Thermospheric Dynamics

The structure of the upper atmosphere is inextricably linked to its constantly changing motion. This motion arises from a number of sources, ranging from steady to periodic to quasi-random in nature, and interaction between the various processes further complicates analysis.

The co-rotation of the atmosphere with the Earth itself constitutes the major part of its motion. It is therefore usually convenient to adopt a rotating coordinate system to investigate deviations from this "background" motion. This introduces centrifugal and Coriolis force terms into the equations of motion, of which normally only the Coriolis term has a significant effect.

The global circulation of neutral winds (relative to this rotating system) is driven mainly by solar heating, which causes a daily expansion and contraction of the atmosphere. The upper atmosphere is observed to superrotate, that is the mean zonal (E–W) wind above the equator is toward the east. Superimposed on this is a divergence away from the subsolar point, and corresponding convergence on the other side of the Earth.

Closely related to the above are the atmospheric tides, whose major components are driven by solar heating. The solar 24 h component appears dominant at low latitudes, high altitudes, giving way to the solar 12 h component at high latitudes and low altitudes. This

latter has been observed for more than two centuries (Hines, 1965, p. 138). A weak lunar 12 h component, resulting from gravitational attraction, has also been observed, but is usually neglected for modelling purposes.

Classical tidal theory, for the solar diurnal and semidiurnal components, is fully developed by Chapman and Lindzen (1970) and will be briefly summarized here. Simplifying assumptions include no dissipation, winds or temperature gradients, a perfectly smooth, spherical Earth, and the atmosphere a perfect gas in hydrostatic equilibrium. Linear perturbation theory applied to the basic equations of motion yields Laplace's tidal equation, an eigenfunction-eigenvalue problem expressed as:

$$F(\Theta_n^{\sigma,s}) = -\frac{4a^2\omega^2}{gh_n^{\sigma,s}} \Theta_n^{\sigma,s} \qquad (2.5.1)$$

with eigenfunctions $\{\Theta_n\}$, functions of latitude known as Hough functions (which may be expanded in terms of associated Legendre polynomials), and eigenvalues $\{h_n\}$ ("equivalent depths"), with the following definitions:

$$F = \frac{1}{\sin\theta}\frac{\partial}{\partial\theta}\left(\frac{\sin\theta}{f^2-\cos^2\theta}\frac{\partial}{\partial\theta}\right) - \frac{1}{f^2-\cos^2\theta}\left(\frac{s}{f}\frac{f^2+\cos^2\theta}{f^2-\cos^2\theta} + \frac{s^2}{\sin^2\theta}\right)$$

$\theta = $ colatitude

$\sigma = $ frequency of oscillation

$s = $ zonal wave number

$\omega = $ Earth's rotation rate

$a = $ Earth's radius

$f = \frac{\sigma}{2\omega}$

Figure 2.8 shows the latitude dependence of some of the dominant Hough functions, with associated equivalent depths listed in table 2.3.
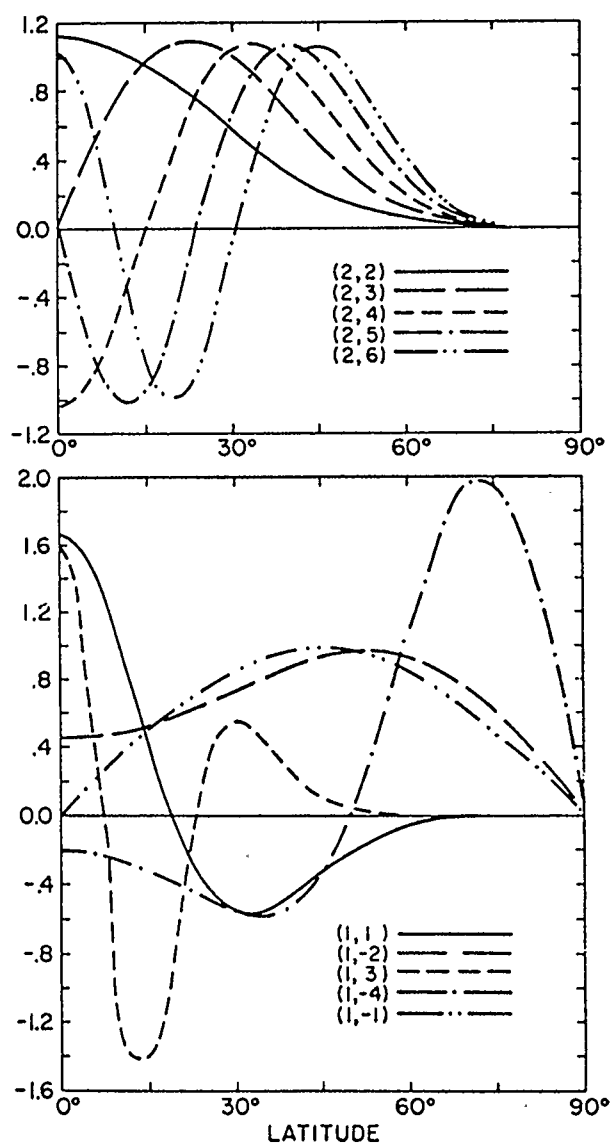
Figure 2.8 Latitude dependence of symmetric Hough functions for the migrating solar thermal tides: (top) semidiurnal, (bottom) diurnal. (Forbes and Garrett, 1979)

Table 2.3 Equivalent depths of symmetric solar tidal wave modes
(Chapman and Lindzen, 1970)

Diurnal mode		h_n (km)	Semidiurnal mode		h_n (km)
gravitational	D(1,1)	0.691	gravitational	S(2,2)	7.85
	D(1,3)	0.120		S(2,4)	2.11
	D(1,5)	0.048		S(2,6)	0.96
rotational	D(1,-2)	-12.27			
	D(1,-4)	-1.76			

Pressure, density, temperature and vertical velocities may be expressed in the general form:

$$g(z,\theta,t) = \sum_n g_n(z)\Theta(\theta)e^{i(\sigma t + s\lambda)} \qquad (2.5.2)$$

where λ = longitude (westward migrating waves), $g_n(z)$ = height structure function which depends on h_n, e.g., for the case of the pressure,

$$p_n(z) = \overline{p}\, e^{(1-i\alpha)z/2H}; \qquad \alpha = \sqrt{\frac{4\kappa H}{h_n} - 1}, \quad \kappa = \frac{c_p - c_v}{c_p} \qquad (2.5.3)$$

For real α we have internal waves with vertical wavelength $\frac{4\pi}{\alpha}$. Imaginary α yields external waves: no vertical wave structure, and amplitude decreasing as $\exp[-z(\beta-1)/2H]$ where $\alpha = i\beta$.

Negative or large positive equivalent depths are thus associated with waves which decay with height. Very small positive h_n yield small vertical wavelengths which are quickly dissipated by destructive interference (Fesen et al., 1986). Therefore most diurnal modes are confined to the region of excitation, particularly at latitudes greater than 30°.

The semidiurnal modes also have small, positive h_n, but with much larger vertical wavelengths that can propagate quite efficiently, particularly the S(2,2) mode which is globally the most dominant.

While classical tidal theory describes reasonably well the gross features of surface level oscillations, more realistic assumptions must be made to calculate thermospheric perturbations, where winds, temperature gradients, and the dissipative effects of molecular viscosity, thermal conduction and ion drag all become quite important. Modifications due to the latter (*i.e.*, dissipation) include complex equivalent depths and altitude dependent Hough functions. Interaction between directly excited modes (diurnal, semidiurnal) and thermospheric winds may produce higher order modes ("mode coupling") and reduced amplitudes of the lower order modes, particularly S(2,2). Recent work in these areas has been done by Mayr *et al.* (1979), Forbes (1982a,b) and Fesen *et al.* (1986), to name a few. Some of these recent results will be applied to an investigation of the so-called "hysteresis problem" of the OI 6300 Å emissions.

Tides are a special case of the more general subject of atmospheric waves, which fall into three main categories. Longitudinal (acoustic) waves are at the high frequency end of the spectrum (T < 270 s) and are rapidly dissipated at high altitudes. At the other end of the spectrum are the Rossby (planetary) waves. These are horizontal transverse waves resulting from Coriolis force variations, and have periods greater than 12 h (Beer, 1974).

Of greatest significance to the upper atmosphere are the vertical transverse waves known as gravity waves. They have periods ranging from several minutes to several hours, and amplitudes increasing with altitude as $\rho^{-1/2}$ (ρ = neutral gas density) to maintain a constant energy density. Tides are gravity waves having periods of (24/m) h (m = 1,2,3, ...). Many large scale gravity waves, known as TID's (travelling ionospheric disturbances), are

generated in the auroral zone during geomagnetic substorms and propagate equatorward. Large fluctuations in ionospheric parameters, such as electron density and temperature, are observed as these disturbances pass through. Airglow intensities are greatly affected by the fluctuations in both ionospheric and neutral densities and temperatures, and substantial amounts of energy may be deposited in the thermosphere during such a disturbance.

Opposing the motion of the (neutral) thermosphere are the frictional forces of viscosity and ion drag. In the upper F region, in the absence of electric fields, ions are more or less locked onto geomagnetic field lines, creating a steady drag on the neutral winds. At low-mid latitudes, equatorward winds drive plasma up the field lines, helping to maintain the nocturnal F_2 layer (see figure 2.9). When the winds decrease or reverse after midnight (Harper, 1971; Burnside, 1984), the layer "collapses" and the characteristic enhancement of the OI 6300 Å airglow intensity is observed as a result of plasma moving down to regions of higher (neutral) density. During this period, the ion/electron density is augmented by downward diffusion of plasma from the plasmasphere. This effect may be quite substantial at Arecibo, where the magnetic dip angle is 50°.

At high latitudes, plasma is accelerated by electric fields, and here ion "drag" is actually a momentum source for neutral winds, which are also modulated by auroral heating (Schunk, 1983).

In the D region and below, plasma is carried along with the neutral gas. A transition region exists in the E and lower F layers, particularly at low latitudes, where neutral wind-induced electric fields result in the "ionospheric dynamo" which modulates the geomagnetic field. Diurnal variations in $\vec{B_E}$ are therefore at least partly a result of tidal oscillations.
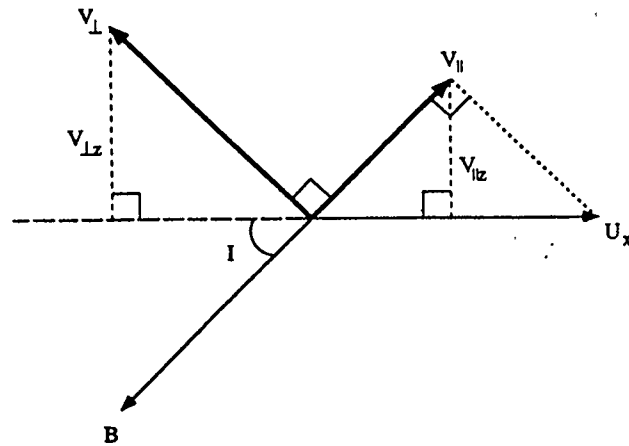
Figure 2.9 Earth's magnetic field over Arecibo and associated plasma motions

u_x = meridional neutral wind

v = plasma velocity

$v_{\parallel} = u_x \cos I$

$v_{\perp} = (\vec{E} \times \vec{B})/B^2$

$v_{\parallel_z} = u_x \cos I \sin I$

$v_{\perp_z} \sim (E_y/B_x) \sin I \cos I$

$\therefore v_z \sim (u_x + E_y/B_x) \sin I \cos I$

(Burrage *et al.*, 1990)

At the dip equator where field lines are horizontal, the resulting $\vec{E} \times \vec{B}$ drift lifts the F_2 peak during the day. Plasma then diffuses down the field lines away from the equator, leading to the previously mentioned Appleton anomaly of local n_e minimum over the equator and maxima near dip latitudes $\pm 18°$. The upward motion of plasma is known as the equatorial fountain (Schunk, 1983).

A concise mathematical description of dynamical processes in the upper atmosphere is given by Richmond (1983); a broad review of the subject may be found in the recent book by M.H. Rees (1989).

Some fundamental equations governing the behaviour of the thermosphere are the following (note that due to diffusive separation of atmospheric constituents above about 120 km, these equations generally refer to individual species).

1. Ideal gas equation of state: $p = nkT$ (2.5.4)

2. Hydrostatic equilibrium $\dfrac{\partial p}{\partial z} = -\rho g$ (2.5.5)

Using (2.5.4) this may be rewritten as $\dfrac{\partial p}{\partial z} = -\dfrac{p}{H}$, where

$H = \dfrac{kT}{mg}$ is the scale height for the species.

3. Momentum equation: $\dfrac{D\vec{v}}{Dt} + 2\vec{\omega} \times \vec{v} + \dfrac{1}{\rho}\nabla p = \vec{g} + \vec{F}$ (2.5.6)

where $\dfrac{D}{Dt} = \dfrac{\partial}{\partial t} + \vec{v} \cdot \nabla$ and $2\vec{\omega} \times \vec{v}$ = Coriolis term.

$\vec{F}$ is a term to describe frictional forces such as viscosity and ion drag.

4. Continuity equation: $\dfrac{\partial n}{\partial t} + \nabla \cdot (n\vec{v}) = P - L$ (2.5.7)

(P = production, L = loss)

This last equation is of primary importance for calculation of expected airglow intensities, where n is the concentration of the emitting species, *e.g.* $O(^1D)$. Standard simplifying assumptions set the left hand side to zero so that production and loss rates may be equated. The continuity equation for n = $[O^+]$ or $[e^-]$ is also a very useful tool for investigating the F_2 region, and much recent work has been done in this area by R.G. Burnside and others (*e.g.*, Burnside, 1984; Burnside *et al.*, 1985; Rishbeth, 1986).

Chapter 3

Experimental Measurements

3.1 Incoherent (Thomson) Scatter Radar

Radio waves are scattered by irregularities of plasma density in the ionosphere, and, at sufficiently high frequencies, by microscopic density fluctuations due to random thermal motion. This scattering is incoherent in nature, and, if dominated by electrons, the scattering cross-section is simply the classical Thomson cross-section for free electrons, hence the term "Thomson scatter". A complete description of the theory may be found in, for example, Evans (1969). The following is a summary of features relevant to this work.

The Debye length of a plasma, the effective range of individual Coulomb interactions, is given numerically by (Bauer, p. 132)

$$\lambda_D = 6.9 \left(\frac{T}{N}\right)^{1/2} cm \tag{3.1.1}$$

where T is plasma temperature in °K, and N is the number density per cm³. If λ is the incident radio wavelength, a useful parameter may be defined:

$$\alpha = 4\pi\lambda_D/\lambda . \tag{3.1.2}$$

Since electrons are responsible for the actual scattering, for $\alpha^2 >> 1$ ($\lambda << \lambda_D$), the frequency spectrum of the returned signal is essentially that of free electrons, and hence is roughly Gaussian with width

$$\Delta f_e = \frac{1}{\lambda} \left(\frac{8kT_e}{m_e}\right)^{1/2} , \tag{3.1.3}$$

where T_e is the electron temperature and m_e is the electron mass. However, for $\alpha^2 \ll 1$, ion-electron interactions become important. The resulting spectrum depends on electron density, ion and electron temperatures (T_i and T_e), ion composition, magnetic fields, electric currents, and bulk plasma motion. The spectral width, being governed mainly by $T_i^{1/2}$ and $m_i^{-1/2}$ (m_i = ion mass), is much narrower than for electrons alone, with a corresponding increase in returned energy per unit bandwidth. Given this practical consideration, and the possibility of obtaining information about the afore-mentioned physical quantities, radar facilities employ wavelengths such that $\lambda \gg \lambda_D$.

The combined backscatter cross-section, per electron, is given by (Evans, 1969)

$$\sigma = \frac{\sigma_e}{(1+\alpha^2)(1+\frac{T_e}{T_i}+\alpha^2)} \tag{3.1.4}$$

where σ_e is the radar cross-section for free electrons ($\sigma_e = 4\pi r_e^2$ for backscatter, where $r_e \sim 2.8 \times 10^{-15}$ m is the classical radius of the electron). For a short transmitted pulse, the radar equation gives the received power due to scattering at a distance R from the transmitter/receiver:

$$P_s = \frac{P_t L N \sigma c \tau \lambda^2}{128\pi^3 R^2} \int_\theta \int_\phi G^2(\theta,\phi) \sin\theta \, d\theta d\phi \qquad \text{(watts)} \tag{3.1.5}$$

N, σ and λ are as above; P_t is the peak transmitter power (W), L is an equipment loss factor, c is the speed of light, τ is the pulse length, and $G(\theta,\phi)$ is the antenna gain over isotropic (Evans, 1969).

The effects of varying T_e/T_i and ion composition on the power spectrum may be seen in figures 3.1 and 3.2. Since these effects are often difficult to distinguish, assumptions about one or the other must usually be made. For example, in the terrestrial F region, O^+ is dominant between 250 and 450 km, so the assumption of pure O^+ is made to obtain
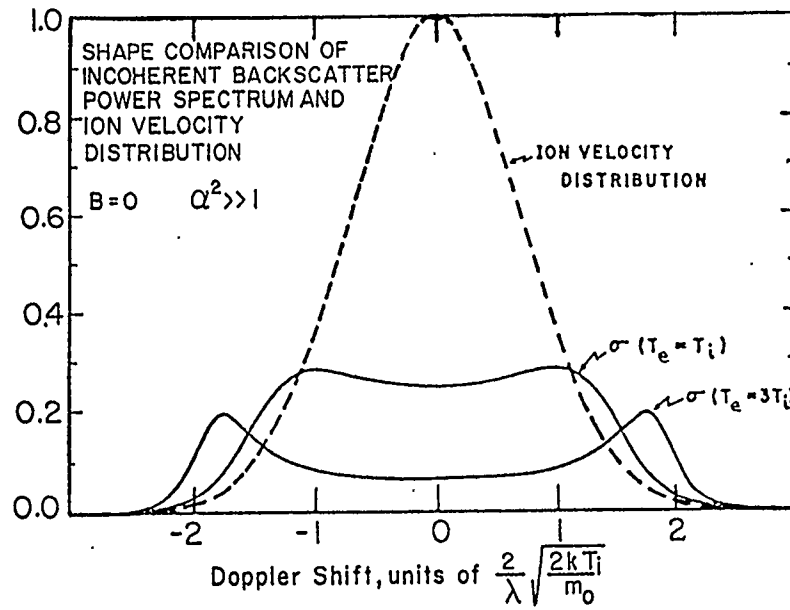
Figure 3.1 Effect of T_e on backscatter spectrum (Farley, 1967)
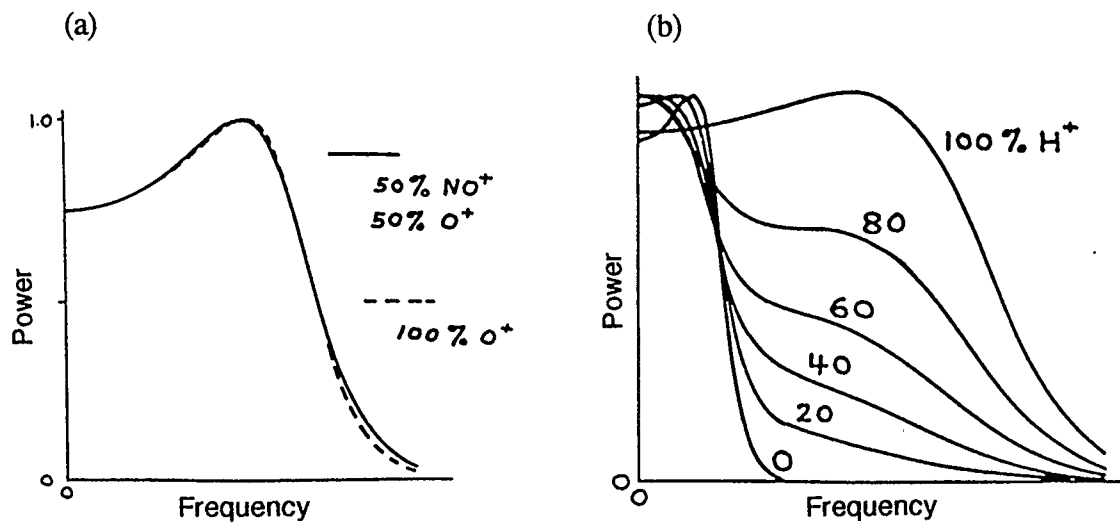
Figure 3.2 Spectra of two-ion mixtures: a) O+ and NO+, b) O+ and H+ (Moorcroft, 1967)

estimates of T_e/T_i. At lower altitudes, NO^+ and O_2^+ become significant, and H^+ and He^+ begin to emerge higher up. In practice, a search is made through a catalogue of theoretical spectra to find the best fit.

Bulk plasma motion (*i.e.*, line of sight ion velocities) may be determined from the net Doppler shift of the backscattered spectrum. The Doppler shift is usually quite small compared with the width of the spectrum, leading to large uncertainties in the ion velocities (Behnke, 1970). Large electric currents may appear as asymmetries in the spectrum, due to electron and ion contributions to Doppler shifts in opposite senses. This is observable only when relative electron velocities are on the order of their thermal velocities (Giraud and Petit, p. 101).

Finally, the Earth's magnetic field may reduce the height of the shoulders of the backscattered spectrum, by limiting the motion of electrons along the line of sight. This may be corrected for if the dip angle of the field is known.

3.2 Measurements at Arecibo

The radio observatory at Arecibo, Puerto Rico, is used part of the time for ionospheric radar sounding. Table 3.1 gives some relevant parameters for the installation. From the magnetic dip angle, it may be seen that electron motion is not severely limited in the line of sight. Also, for normal night-time conditions, $\alpha^2 << 1$ for the given operating frequency.

There are two main modes of operation of the radar system. The original mode employs pulse lengths on the order of 0.1 ms, yielding height resolution ($\Delta h = c\Delta t/2$) on the order of 10 km. The autocorrelation function (ACF) of the returned signal is calculated (details

in Behnke, 1970) to aid determination of n_e, T_e and T_i, and line of sight ion (plasma) velocity, v_z. These are determined fairly reliably in the altitude range 250-500 km, where O^+ ions dominate. Statistical uncertainties for n_e, T_e and T_i have been estimated at ±5% (Carlson, 1965; Wickwar, 1971).

Table 3.1 Arecibo Observatory Parameters
(Giraud and Petit, p. 100; Wickwar, p. 49; and technical data sheets)

Geographic Coordinates	18° 21' N, 66° 45' W
Geomagnetic Latitude	30° N (L=1.43)
Dip angle	50°
Antenna	300 m fixed spherical reflector
Operating frequency	430 MHz
Wavelength (λ)	69.7 cm
Peak power output	2.5 MW maximum
Beam width	(1/6)° (9 arc min)
Pulse length	μs to ms
Debye length (λ_D)	~.2-.8 cm (T_e~1000 K, n_e~10^5-10^6 cm^{-3})
$\alpha = 4\pi\lambda_D/\lambda$	~.04-.15

For resolution finer than 10 km, the ACF (single pulse) method is unsatisfactory due to poor signal to noise ratios at short pulse lengths. The technique of modulating longer pulses was introduced to overcome this limitation. In this method the phase of the transmitted signal is inverted (shifted abruptly by 180°) at various intervals. At Arecibo, a 13 element Barker code is used (see figure 3.3) to give height resolution of 600 m (equivalent to the resolution of a single 4 μs pulse), with signal to noise ratio equal to that

for a 52 μs pulse. Only the electron density profiles are obtained from this sampling, but for the altitude range 80 to 540 km.
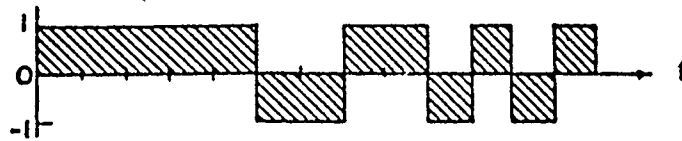
Figure 3.3 A 13 element Barker coded signal (Ioannidis and Farley, 1972)

ACF and Barker coded modes of operation are interwoven to provide continuous coverage of ionospheric parameters. Both modes require absolute calibration by an independent measure of electron density. The required calibration is provided by a nearby ionosonde - a type of radar which scans radio frequencies near the plasma frequency to find the maximum frequency that can be totally reflected. For the ordinary mode wave in the F_2 region, this critical frequency is referred to as f_oF_2, and is a measure of the maximum electron density in the region (Chamberlain and Hunten, p. 247):

$$n_{max} = 1.24 \times 10^4 \, (f_oF_2)^2 \qquad (3.2.1)$$

where n_{max} is per cm^3, and f_oF_2 is expressed in MHz. Ionograms (ionosonde traces) can be very difficult to read, particularly for night-time data, which may lead to some problems in interpretation.

3.3 Airglow Photometry

The airglow facility located adjacent to the radio telescope at Arecibo allows for convenient simultaneous measurements of both ionospheric parameters and airglow intensities. For the experiment analysed in this thesis, the latter were measured at 6300 Å and 5577 Å using tilting filter photometers, as described by Eather and Reasoner (1969). This type of photometer, shown schematically in figure 3.4, employs interference filters whose passbands are shifted to shorter wavelengths when they are tilted away from normal incidence of the incoming light beam. Filters are chosen such that the passband is centred at a slightly longer wavelength than required. A scan through all possible tilt angles is then certain to pass through the peak of the desired emission line. There are advantages to this method over a fixed filter system, one being that the passband of a fixed filter may change with time so that it is no longer centred on the emission line peak. Another is that a tilt scan will find both the peak emission and the nearby background continuum, facilitating the subtraction of background from the signal (figure 3.5).

The number of photon detections at a series of tilt angles constitute the raw data, and therefore counting statistics apply to the results. Increasing the field of view of the photometer, and hence the detected flux, will improve the precision of the measurements, although spectral resolution will be diminished due to the larger range of wavelengths passed through the filter at a given tilt angle. The instruments at Arecibo normally use a 5° field of view, corresponding to a circle of about 26 km diameter at an altitude of 300 km. This results in precisions a few percent for normal intensity values. Intensities are reported as integrated column brightnesses in rayleighs (R). For I $\leq$ 10 R, good precision is difficult to obtain; 5 R is considered the minimum reliable detection (Wickwar *et al.*, 1974).
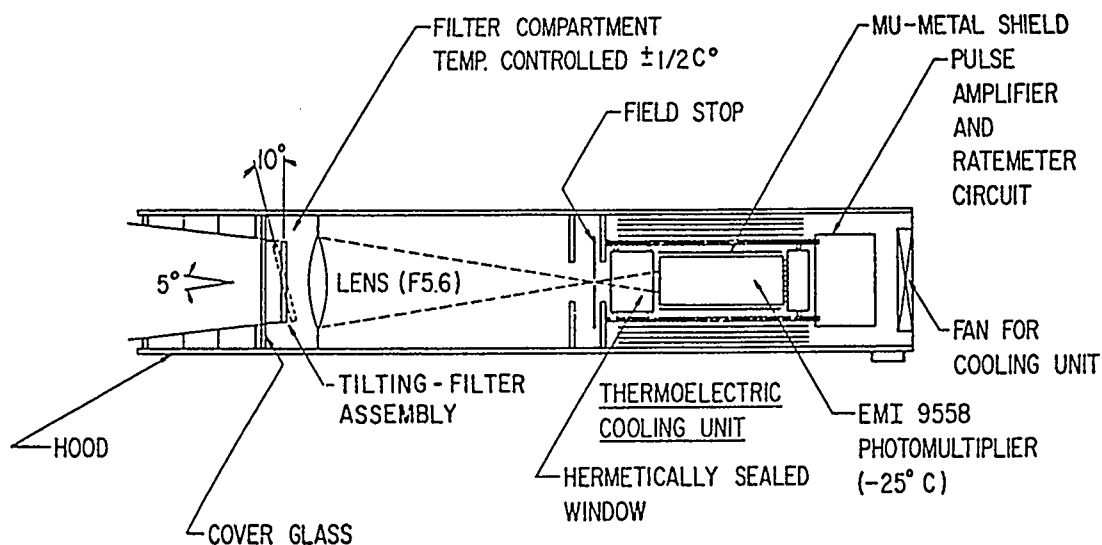
Figure 3.4 Basic features of tilting filter photometer (Wickwar, 1971)

time $\longrightarrow$
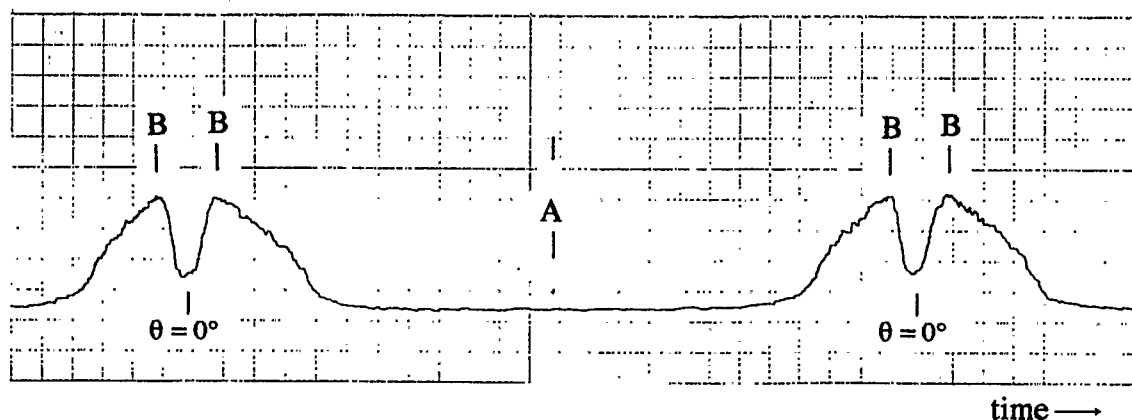
Figure 3.5 A typical filter scan. At A the photometer filter reaches its largest tilt angle (θ), and the scan reverses direction. As tilt angle increases, the photometer responds to progressively shorter visible wavelengths. At points marked B, the photometer filter passband is centred at the 5577 Å emission of atomic oxygen.

Although counting statistics contribute random error, a much greater source of uncertainty in intensity measurements results from calibration of the photometers. Calibration was accomplished using a C^{14}-activated phosphor emitting surface as a low brightness source (LBS) with a fixed emission rate. The absolute uncertainty of this calibration is estimated to be $\leq 15\%$. The combined effect of counting and calibration errors is an expected uncertainty of photometer readings of $\leq 20\%$.

Both photometers used in the present experiment employ a 5° field of view, yielding a bandwidth of 6 Å for the 6300 Å filter, and 5 Å for the 5577 Å filter. The size and shape of the transmittance curve vary with tilt angle (figure 3.6), and must be accounted for in the intensity calculations (see Wickwar, 1971).

FILTER TRANSMITTANCE FOR LIGHT INCIDENT IN A 5° CONE
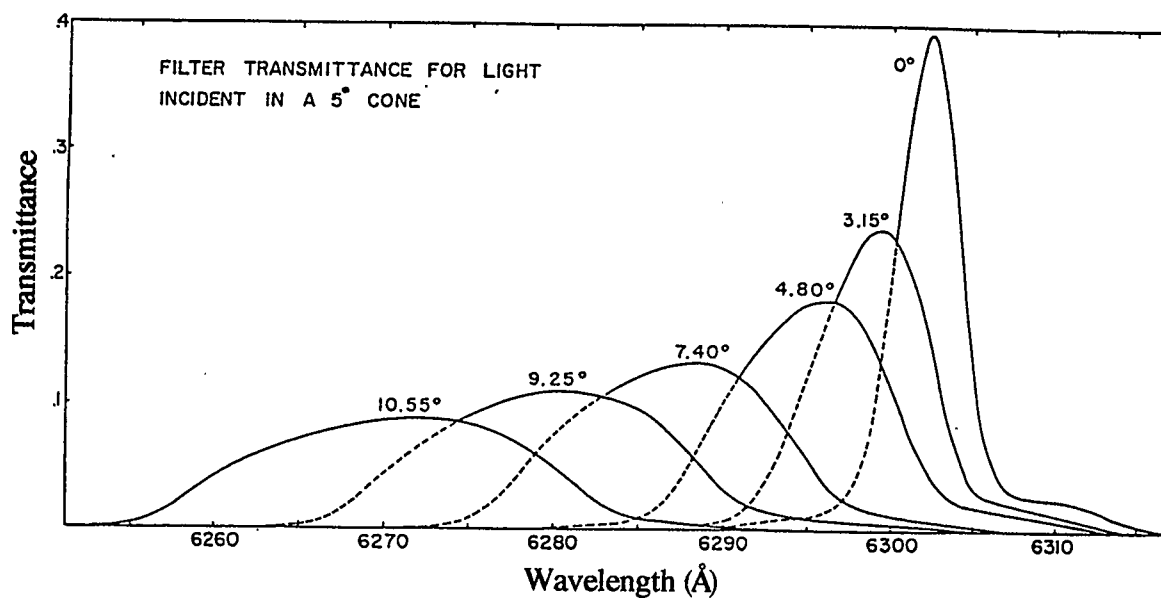
Figure 3.6 Transmittance curves for the 6300 Å filter (Wickwar, 1971)

3.4 Summary of data obtained

The data set analysed in this thesis consists of radar data obtained by L.L. Cogger at Arecibo in March and April of 1985, for a total of 7 nights. Radar data were supported by reduced photometer intensities for the same period. The radar data were processed by the staff at the observatory to yield height profiles of n_e, T_e, T_i, and v_z. In the ACF mode, a height resolution of 24 km was achieved over a range from 151 to 507 km, for a total of 20 heights. The Barker coded data were averaged over groups of 8 adjacent values, for a final resolution of 4.8 km and a total of 100 heights. Individual error estimates were given for the ACF data, but not for the Barker profiles. With the exception of the last April night, the radar beam was vertical so that information in one dimension only was received. The final night was a World Day run, employing a beam swinging technique (Hagfors and Behnke, 1974) at a 15° zenith angle, with 12 azimuth positions per rotation. No Barker profiles were obtained for this night.

The pre-processed radar and photometer data were sent to Calgary on magnetic tape. Some calibration difficulties were perceived in the radar data in the subsequent analysis. Consequently, it was decided to include additional data obtained at Arecibo in 1971 and 1976 (by L.L. Cogger) for verification of results. Time and height resolution of these earlier data are inferior, but quite adequate for photochemical modelling.

A list of the data analysed in this investigation is given in Tables 3.2. and 3.3. Table 3.2 contains the original 1985 acquisitions, and Table 3.3 lists the earlier observations of 1971 and 1976. All times are given in Universal Time (UT); local time at Arecibo is four hours earlier. Also listed in the tables are some geophysical parameters (Ap, f107, f107a) which are relevant for atmospheric modelling.

Table 3.2 Radar and Photometer Data from Arecibo, 1985

Dates	Daily Ap	f107	f107a	Radar Times	Radar Parameters	Photometer times
Mar 22/23[a]	5	75.9	73.6	2210 −1020	n_e,T_e,T_i,v_z Barker n_e profiles	0005–0030 0115–0345 0415–0935
Mar 23/24[a]	6	77.3	73.7	2215 −1000	n_e,T_e,T_i,v_z Barker n_e profiles	0215–0925
Mar 24/25[a]	5	79.6	73.7	2215 −1000	n_e,T_e,T_i,v_z Barker n_e profiles	2325–0935
Apr 20/21[a]	103	72.3	77.9	2300 −1000	$n_e,T_e,T_i,v_z,[H^+]/n_e$ Barker n_e profiles	0030–0855
Apr 21/22[a]	11	77.9	77.9	2135 −1000	$n_e,T_e,T_i,v_z,[H^+]/n_e$ Barker n_e profiles	0005–0910
Apr 22/23[a]	12	89.8	77.9	2350 −0935	$n_e,T_e,T_i,v_z,[H^+]/n_e$ Barker n_e profiles	2350–0100 0215–0915
Apr 23/24[b]	17	93.3	77.9	0330 −0930	$n_e,T_e,T_i,v_z,[H^+]/n_e$	2350–0905

[a]all measurements made in zenith (ZA = 0°)

[b]ZA = 15°; beam rotated with 12 azimuth positions per cycle.

Constants: ACF heights 151-607 km, Δh = 24 km; Δt ~ 1.5 min.

Barker profile heights 61-356 km, Δh = 4.8 km; Δt ~ 1.5 min.

Photometers: 5577 Å and 6300 Å; Δt ~ 45 - 50 s.

Ap: index of geomagnetic activity (units of 2 nT)

f107:   daily solar flux measured at 10.7 cm (2800 MHz)

f107a: f107 averaged over 81 days centred on day in question

40

Table 3.3 Radar and Photometer Data from Arecibo, 1971 and 1976

Dates	Daily Ap	f107	f107a	Times	Δt (min)	n_e Profile Heights (km)	Δh (km)
1971							
Mar 3/4	9	124	128	2325–0955	~10	177–560	11.6
Mar 26/27	15	108	124	2200–0810	"	"	"
Mar 31/Apr 1	26	103	124	0225–0705	"	"	"
Jun 2/3	31	106	113	0145–0925	"	"	"
Jun 16/17	6	88	110	2200–0925	"	"	"
Oct 18/19	2	99	110	0150–1005	"	"	"
1976							
Apr 25/26	9	74.9	73.4	0110–0915[a]	15–20	161–491	6
Apr 27/28	11	72.9	73.6	0620–0905	15	173–491	"
Apr 28/29	10	72.4	73.4	0515–0915	8	161–491	"
Apr 29/30	17	79.5	73.4	2320–0045 0500–0920	8–12	173–491	"

[a]Photometer data for Apr 25/26, 1976 from 0350 only.

Observations: 6300 Å brightness, T_i (averaged over 300-400 km altitude), n_e profiles (5577 Å brightness obtained for first 5 nights).

Note: all measurements made in zenith (ZA = 0°)

Chapter 4

Analysis of Data

4.1 Preliminary Processing

The data received from Arecibo for use in this investigation are summarized in the preceding chapter. As described in the following, some preliminary editing and smoothing were applied before using the results to model airglow emissions.

4.1.1 Radar ACF Data

Parameters with estimated errors >20% were removed from this data set, and the remaining values were averaged in groups of 3 for a temporal resolution of about 5 min. For most of the nights studied, the characteristic times for changes in the ionosphere were sufficiently long to make this resolution quite adequate. Some sample profiles may be seen in figures 4.1–4.4, with figure 4.5 showing F_2 peak parameters.

In the absence of any unusual heating mechanisms in the nocturnal F region, it is normally safe to assume thermal equilibrium between ions, electrons and neutrals (*e.g.*, Cogger *et al.*, 1970), *i.e.*,

$$T_i = T_e = T_n$$

The measured ion and electron temperatures were thus used to obtain estimates of the exospheric (neutral) temperature, T_{ex}. At each height, ion and electron temperatures were averaged. The results were then spatially averaged over the altitude range of 300 to 500 km. Temperatures found by this method are referred to as "avTi" on all following graphs.

To smooth out the resulting exospheric temperatures and facilitate calculation at any desired time, they were first fit to 10th degree polynomials. While general trends were well represented by this technique, possibly significant fluctuations were smoothed out, and the functions were not well behaved near the ends of the data. It was thus decided to use spline functions for the purpose, as described by C.H. Reinsch (1967). (Computer subroutines for cubic spline smoothing and interpolation are available in the IMSL.) This method allows the user to vary the so-called smoothing parameter to produce as much or as little smoothing as required, and makes no assumptions concerning the functional form of the data. Some results are shown in figures 4.6 and 4.7.

4.1.2 Barker Electron Density Profiles

Individual error estimates were not available for the Barker electron density profile data, so the entire set was averaged in groups of three, again for a temporal resolution of about 5 min. Since the calculation of airglow intensities is very sensitive to electron densities around and just below the F_2 peak, spline smoothing was again applied here to produce well-behaved profiles (fig. 4.7). A more analytical approach to this problem would be to fit Chapman-type functions to each profile (Burnside *et al.*, 1983), but there is a danger of smoothing out unusual features, such as waves, superimposed on the basic Chapman profiles.

The height and electron density of the F_2 layer peak were extracted from each profile after smoothing, and a few values for f_oF_2 were calculated for each night. When these were compared with entries in the log book, some significant differences were found. Differences in n_e profiles between the ACF and Barker data (see fig. 4.1) also led to the suspicion that there may have been some problems with the calibration of the radar.

To investigate this further, ionograms were obtained from Arecibo for the nights in question. These proved to be rather difficult to read (fig. 4.8), but several estimates of f_oF_2 were made and the Barker profile densitites were recalculated accordingly. Confidence in the absolute accuracy of these measurements has thus been somewhat reduced.

For Apr 23/24, 1985, the ACF n_e profiles were spline smoothed, and values calculated for Barker profile heights. This will not reproduce the true profiles, however, as the coarser resolution of the ACF data (24 km as opposed to 4.8 km) has already smeared out the electron densities.

4.1.3 Photometer Data

Photometer data appeared much less variable than the radar data, so no preliminary averaging was performed, leaving the temporal resolution at 45–50 s. Spline smoothing was applied, mainly for the purpose of calculating intensities at intermediate times (see figs.4.9–4.15).

Data from 1971 and 1976 had already been processed to obtain smoothed values at appropriate times (Cogger *et al.*, 1980), so these results were used directly in the airglow calculations.
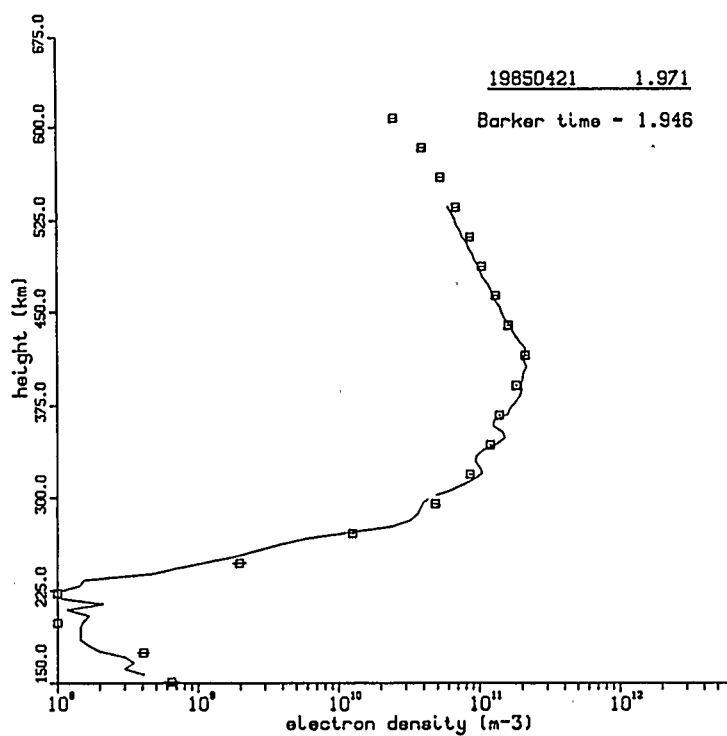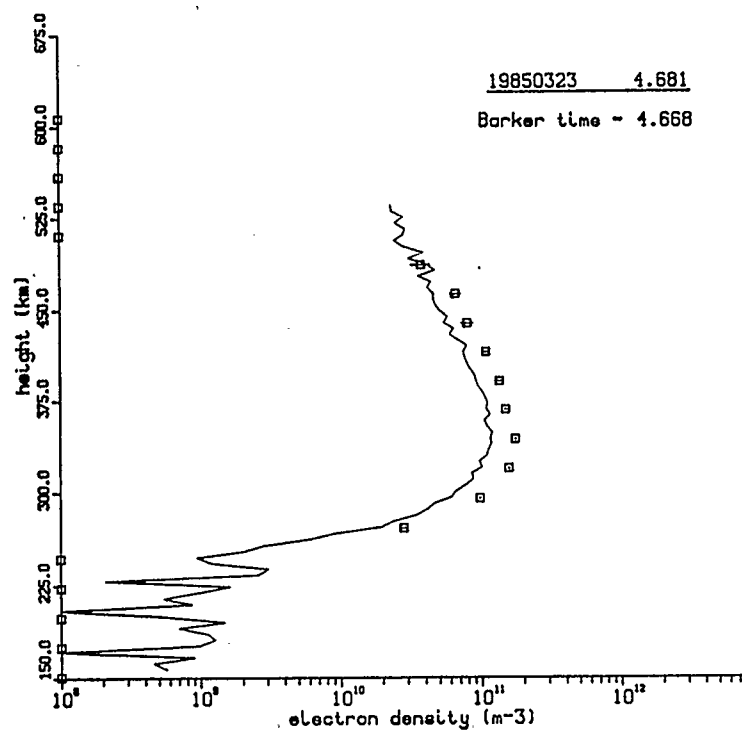
Figure 4.1 Electron density profiles: points from ACF data, solid line

shows Barker profiles
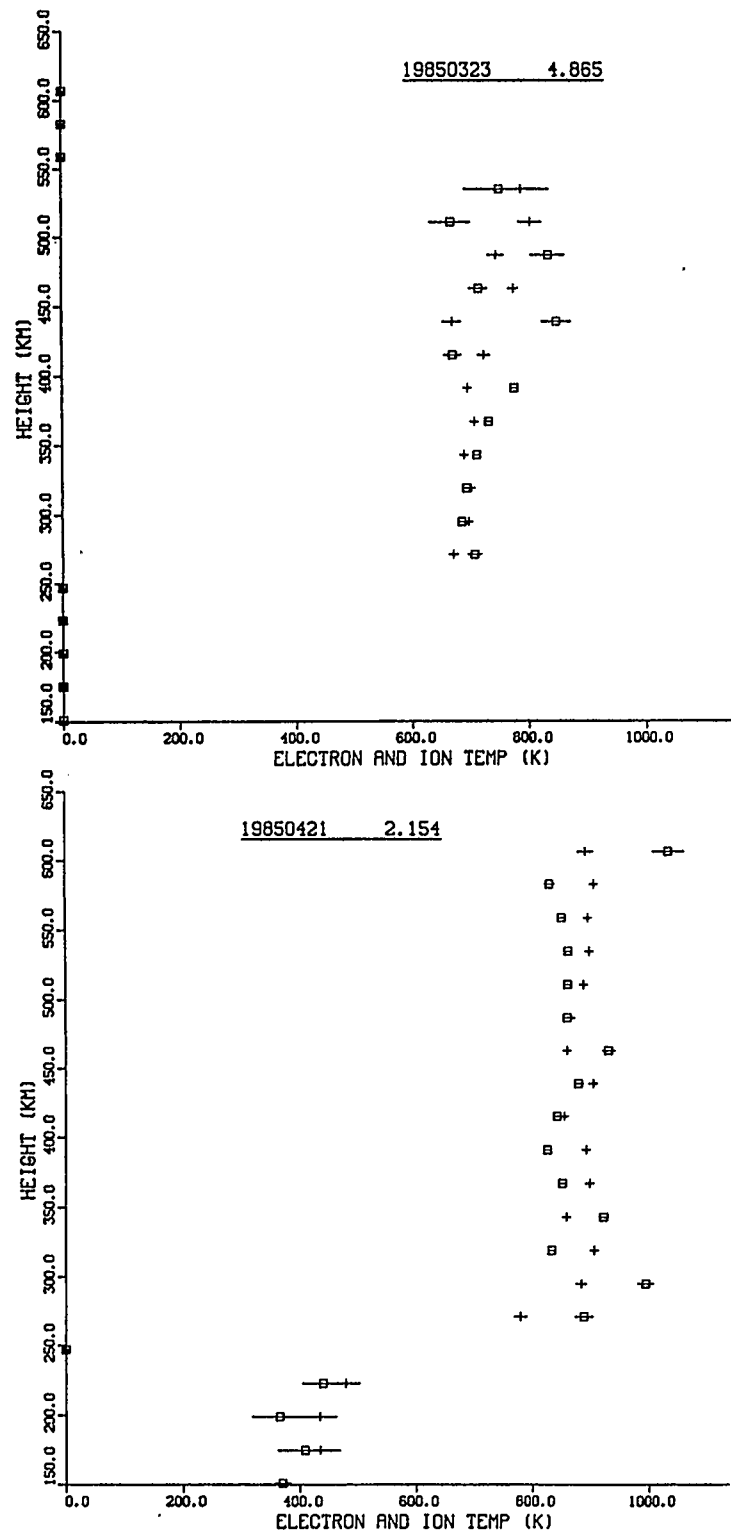
Figure 4.2 Ion (crosses) and electron (squares) temperature profiles
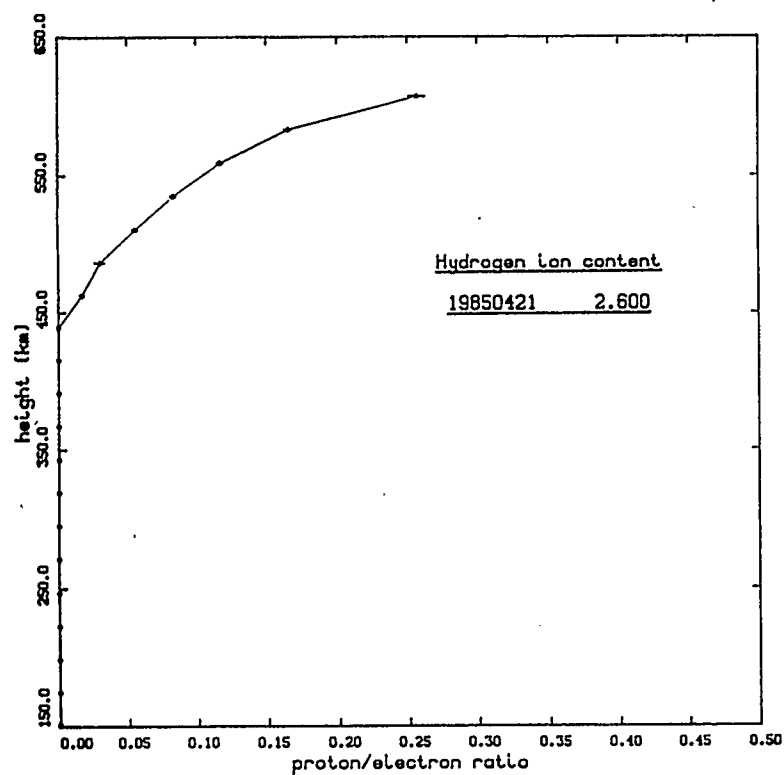
Figure 4.3 Hydrogen ion content of upper F region
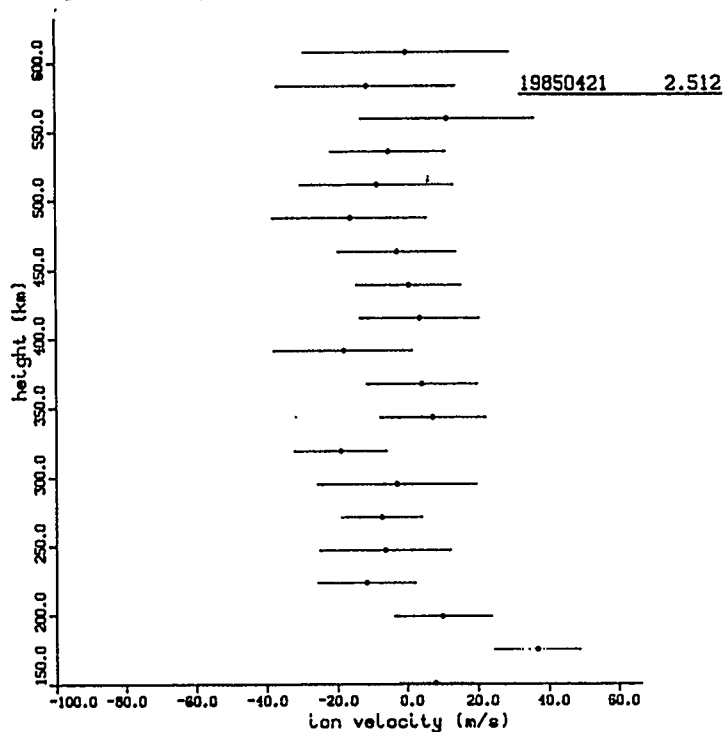
Figure 4.4 Vertical ion velocity profile
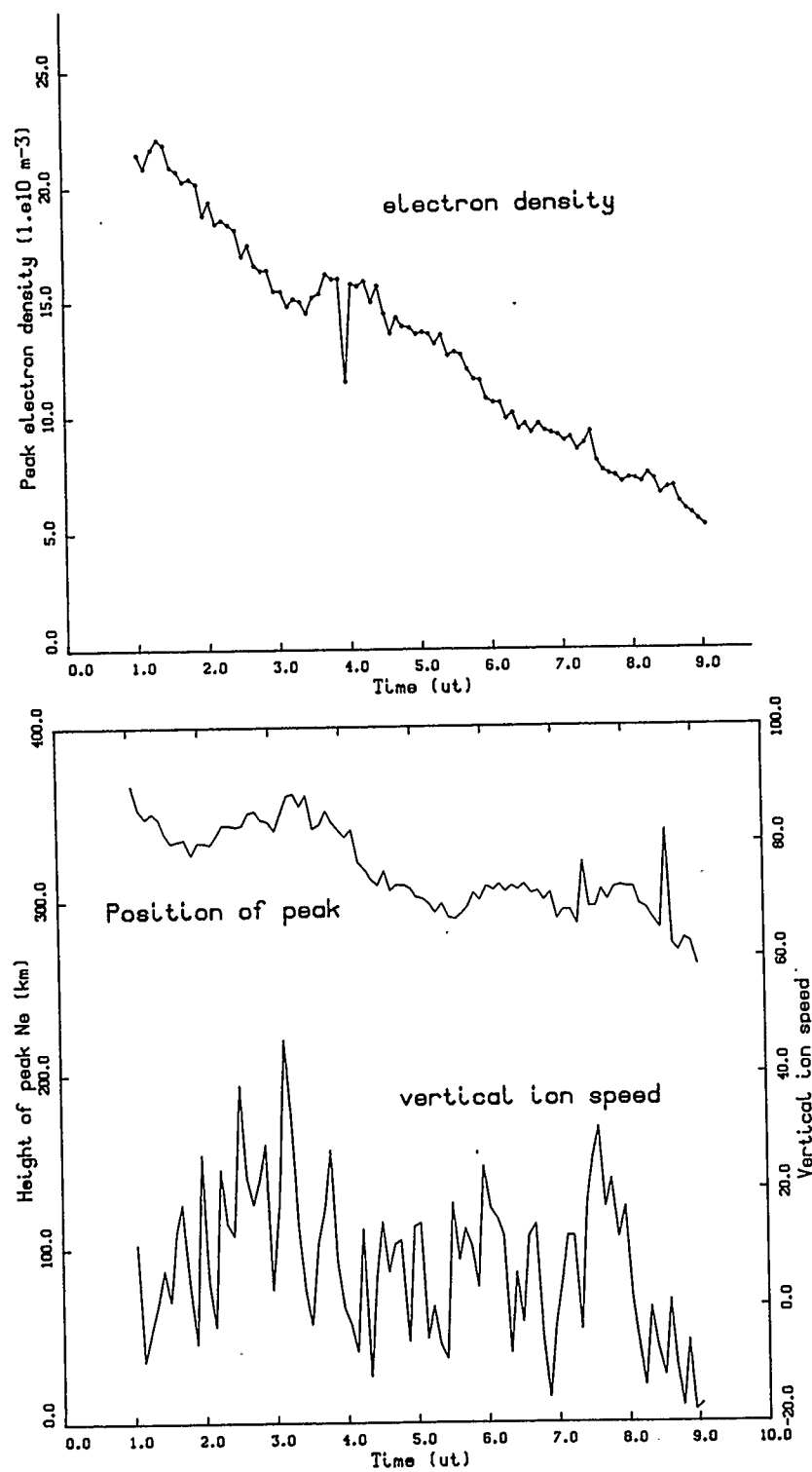
Figure 4.5 F2 peak parameters for April 22, 1985.

Top: electron density at peak (n_{max}).

Bottom: height of peak and vertical ion velocity at peak (m/s)
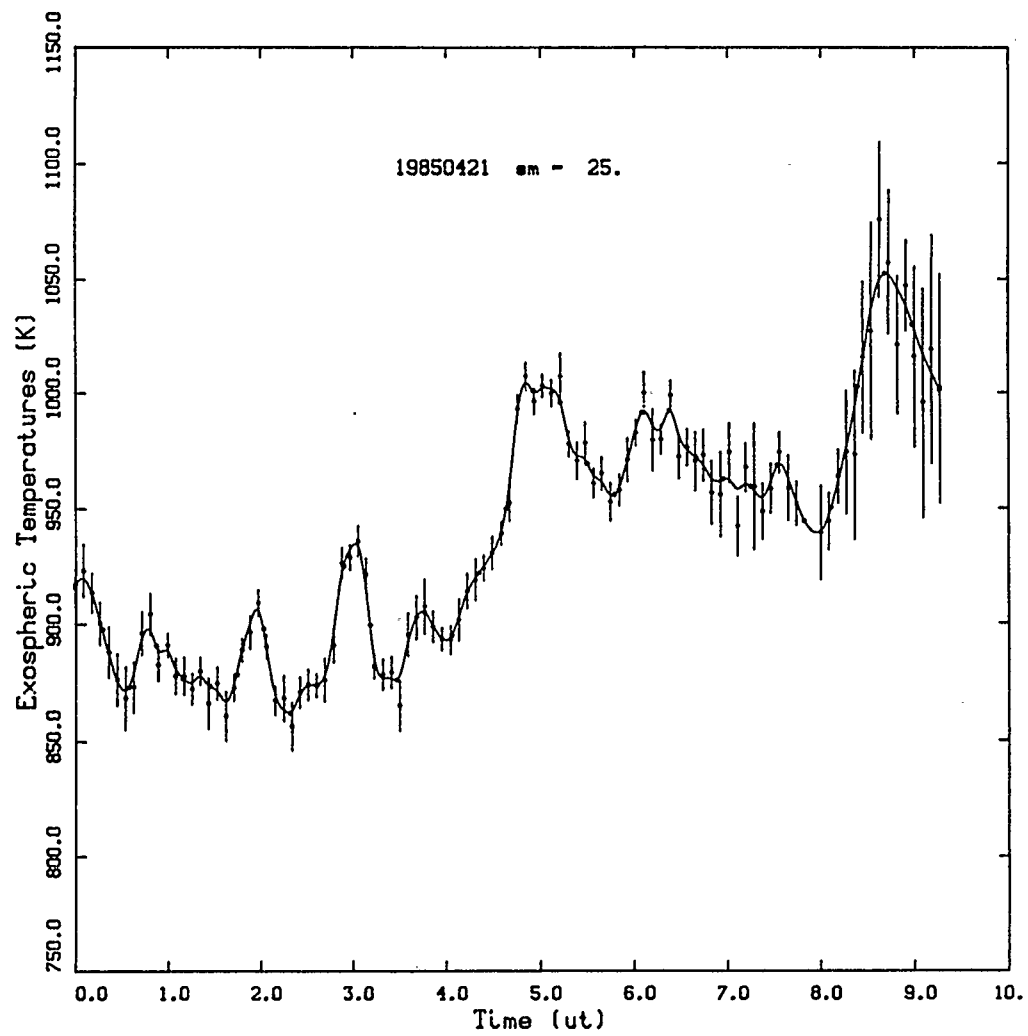
Figure 4.6 Spline smoothing of exospheric temperatures
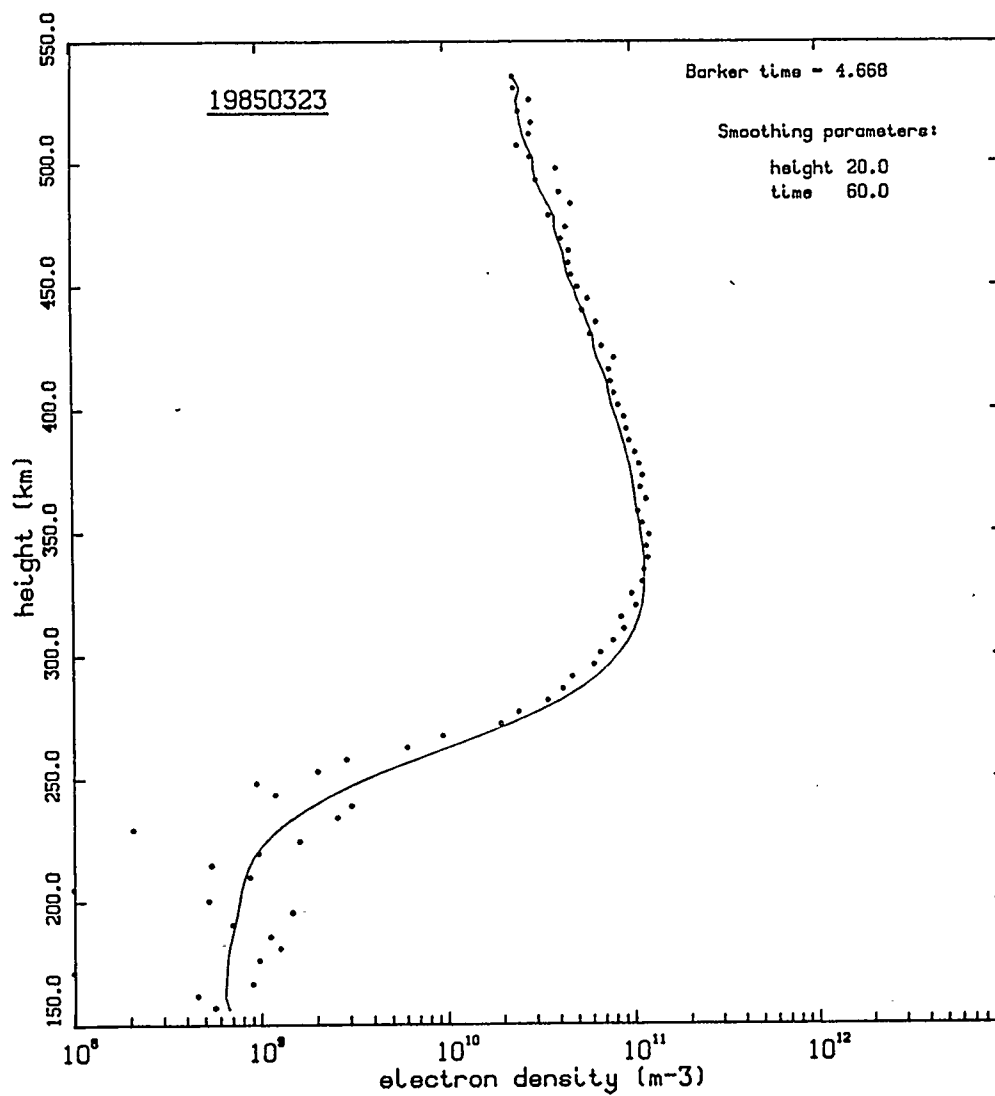
Figure 4.7 Spline smoothing of electron density profiles
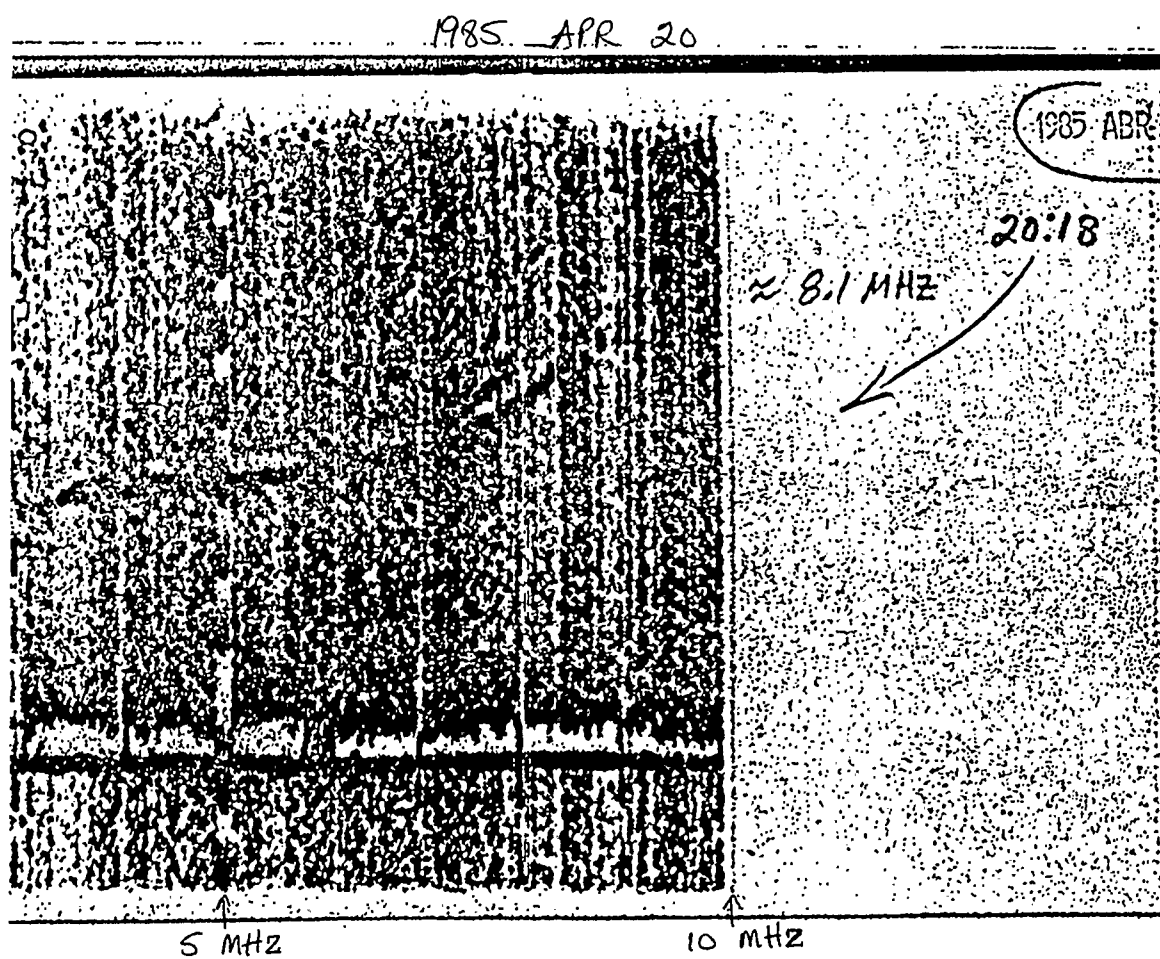
Figure 4.8 Sample ionogram from Arecibo Observatory
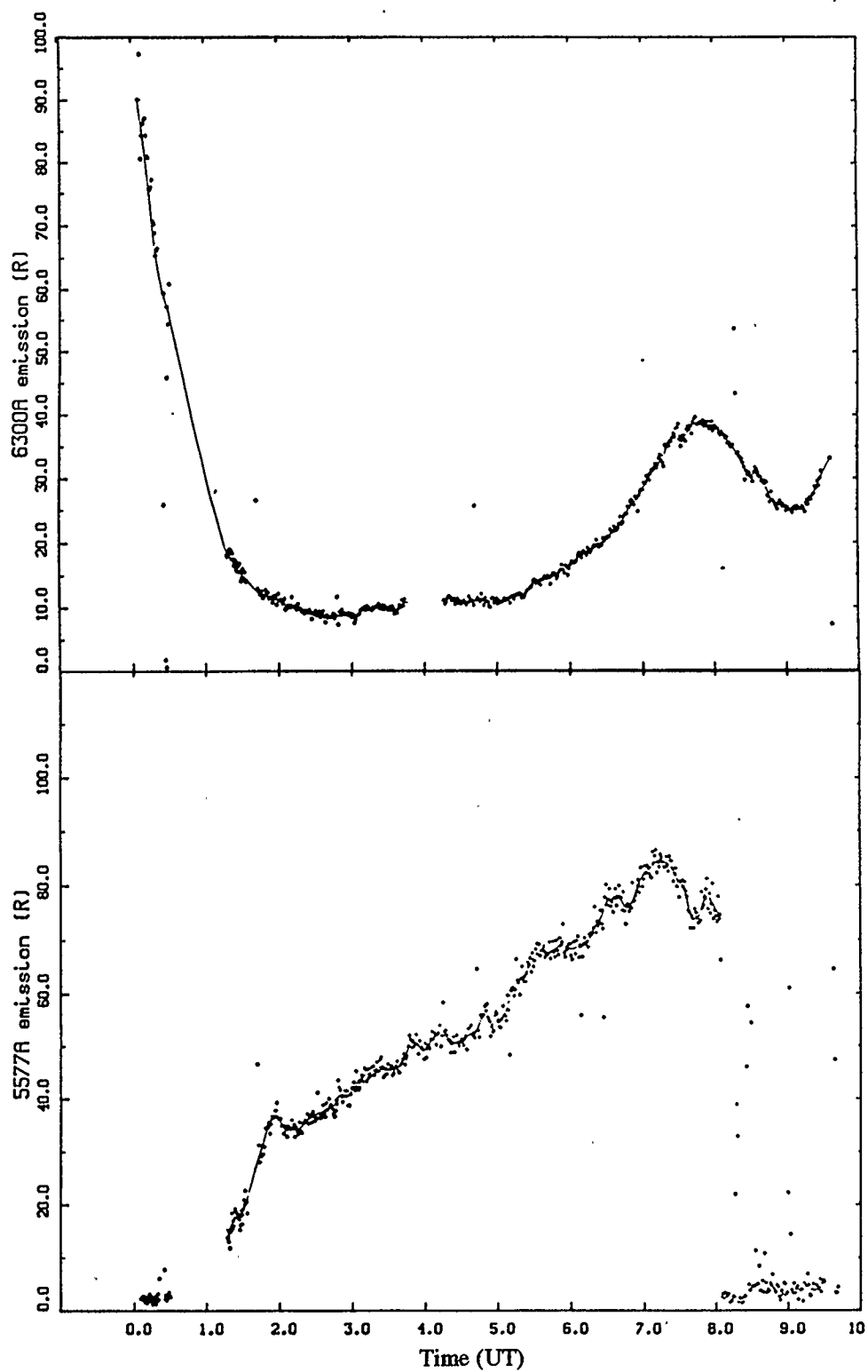
Figure 4.9 Smoothed photometer data from Arecibo – March 22/23, 1985
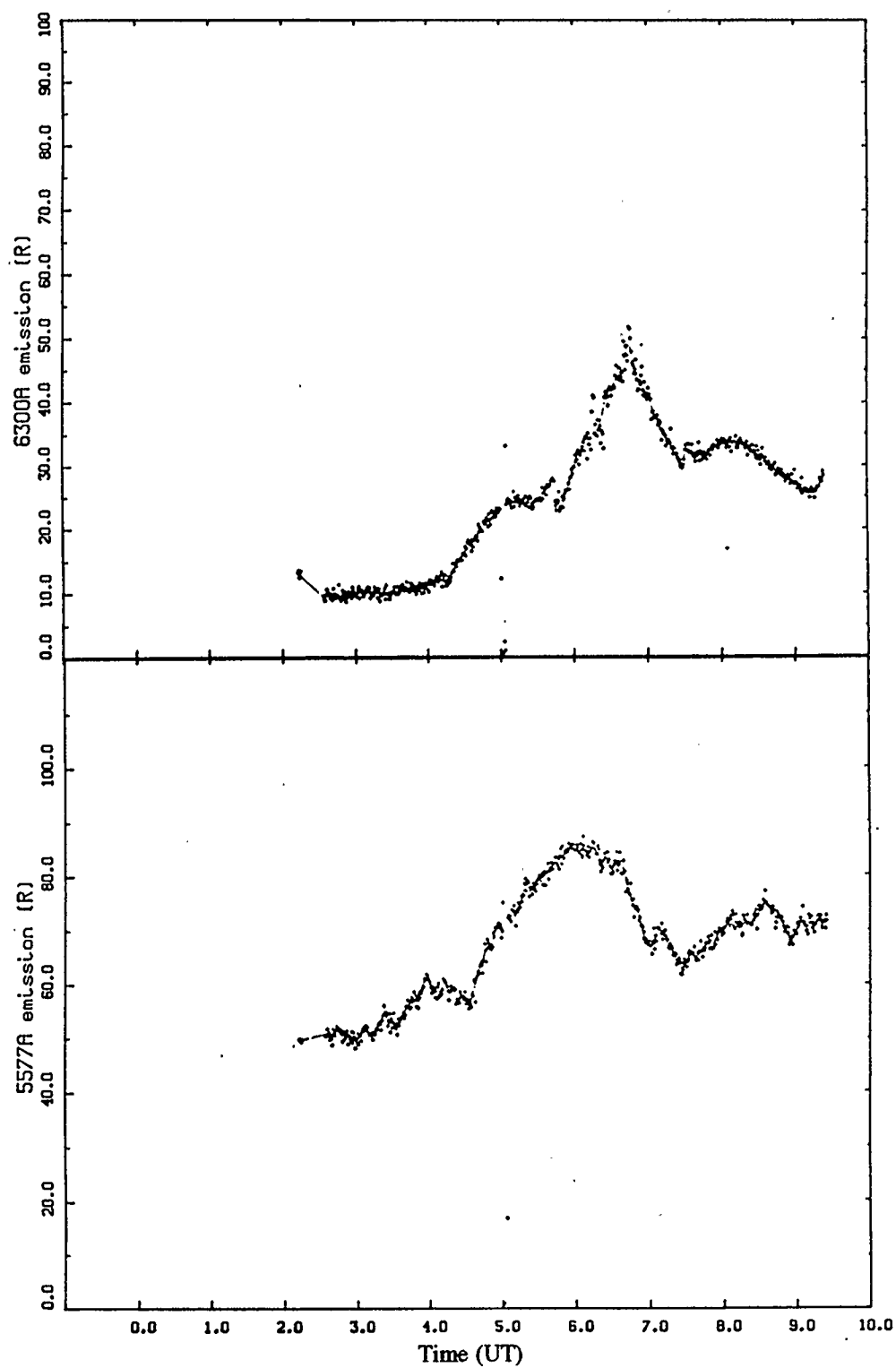
Figure 4.10 Smoothed photometer data from Arecibo – March 23/24, 1985
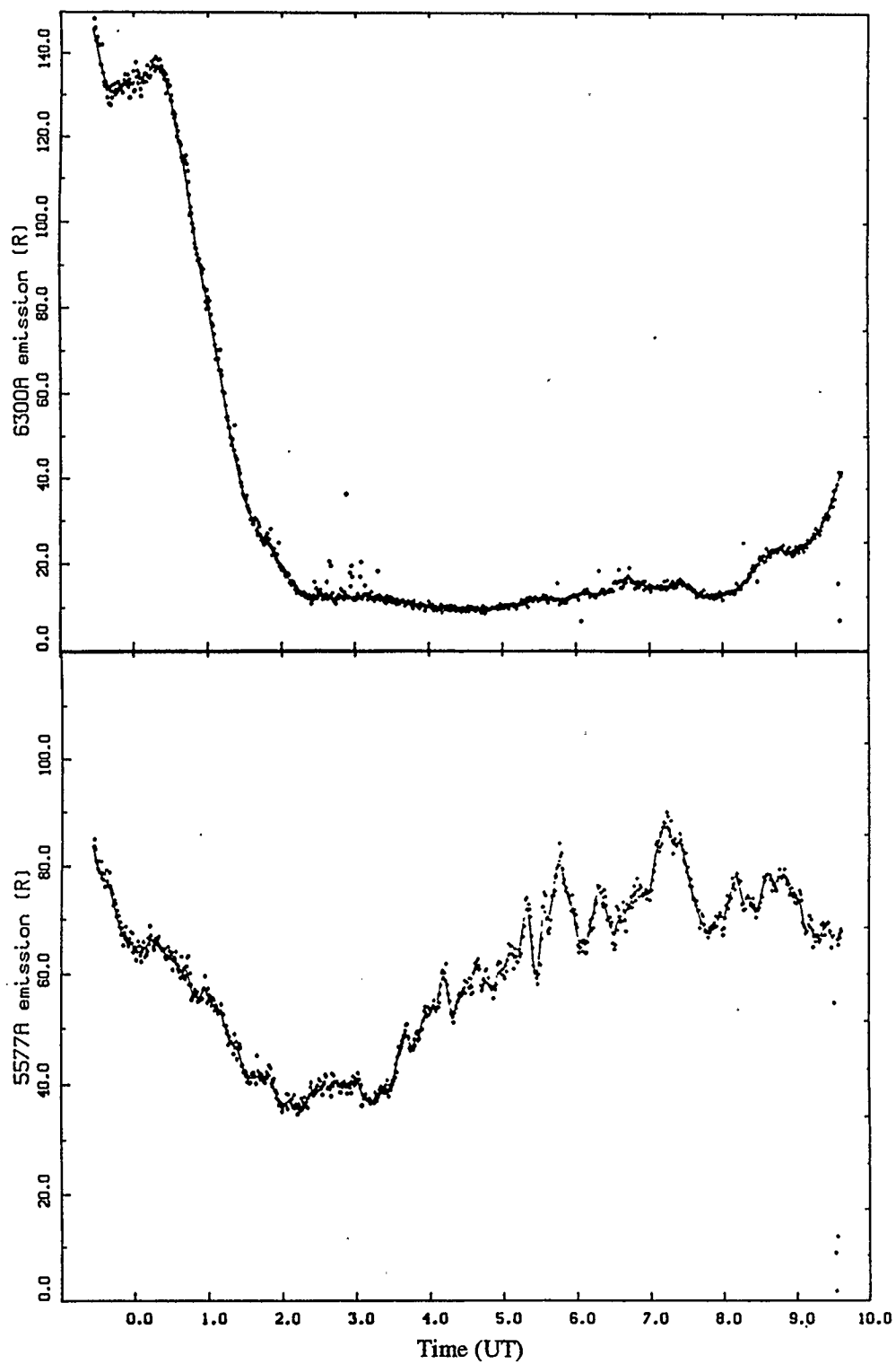
Figure 4.11 Smoothed photometer data from Arecibo – March 24/25, 1985
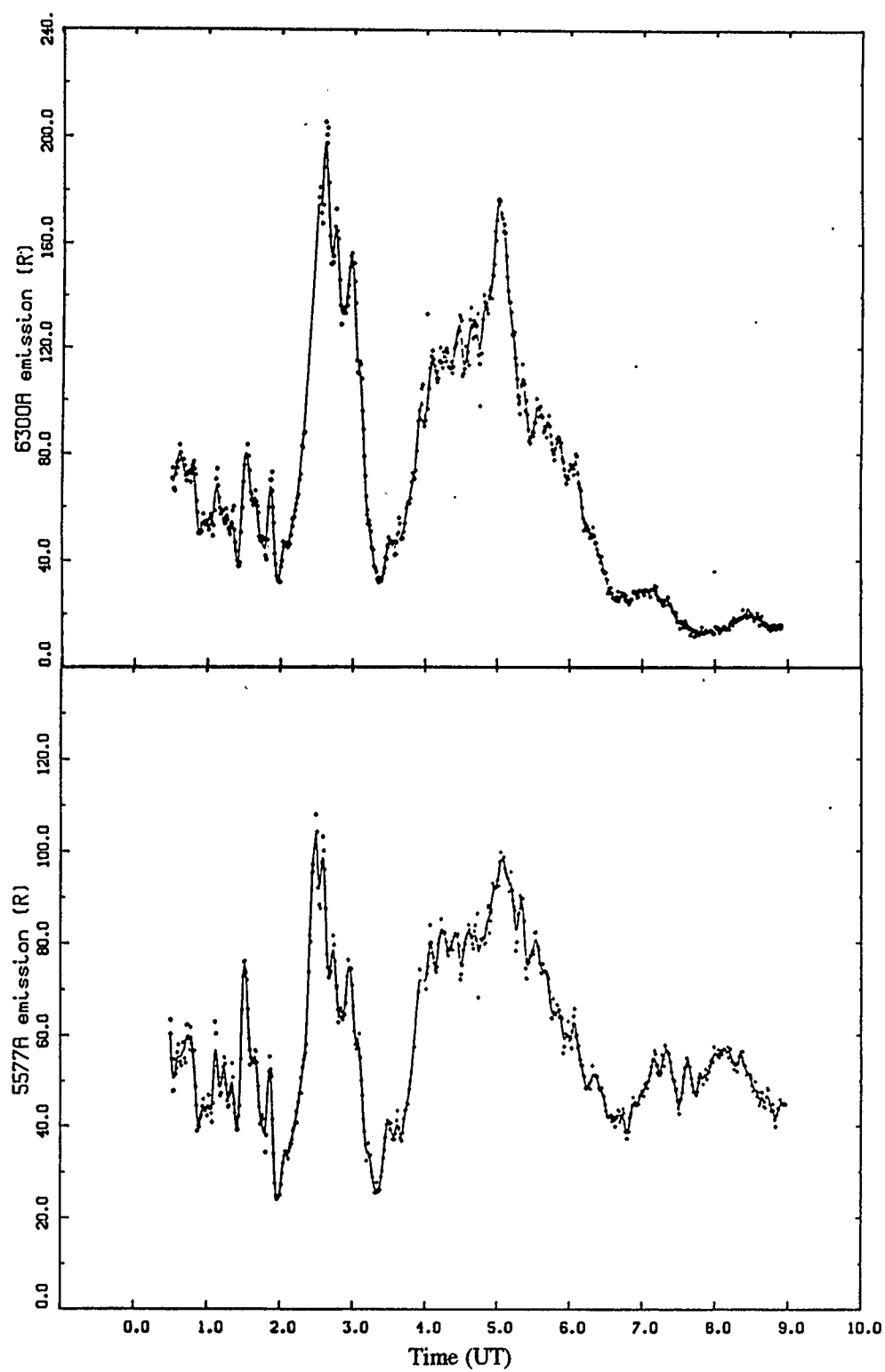
Figure 4.12 Smoothed photometer data from Arecibo – April 20/21, 1985
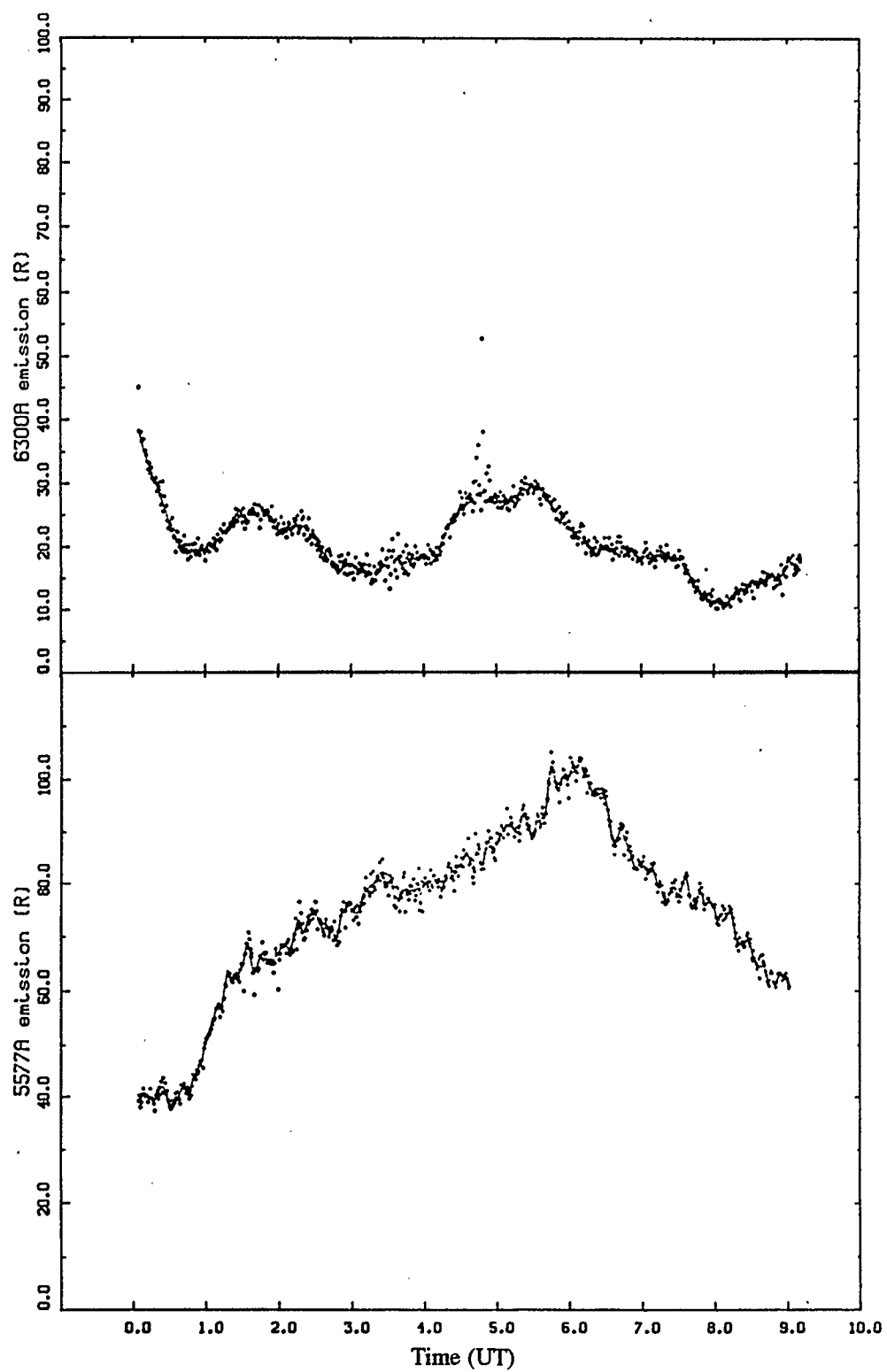
Figure 4.13 Smoothed photometer data from Arecibo – April 21/22, 1985
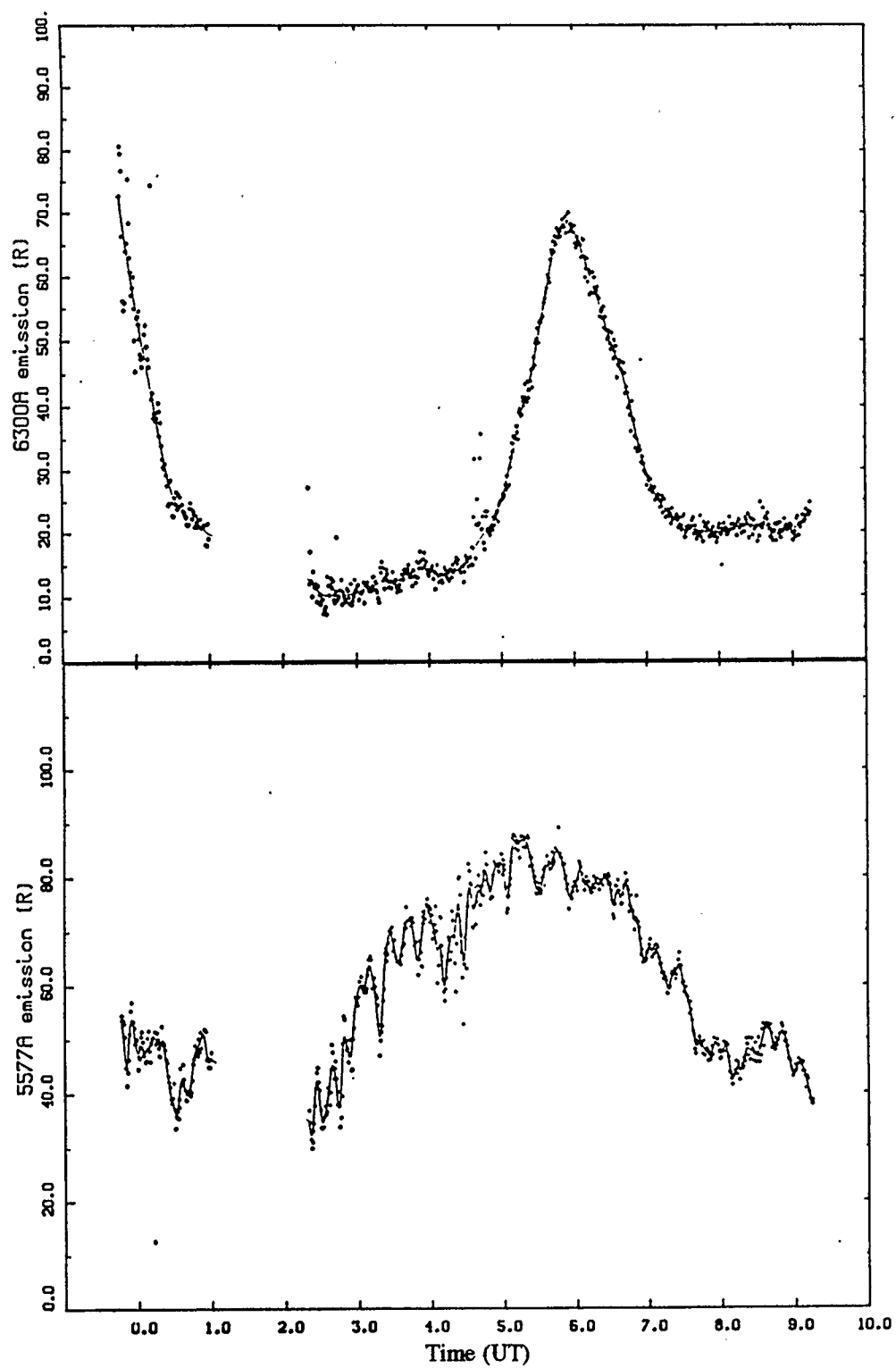
Figure 4.14 Smoothed photometer data from Arecibo – April 22/23, 1985
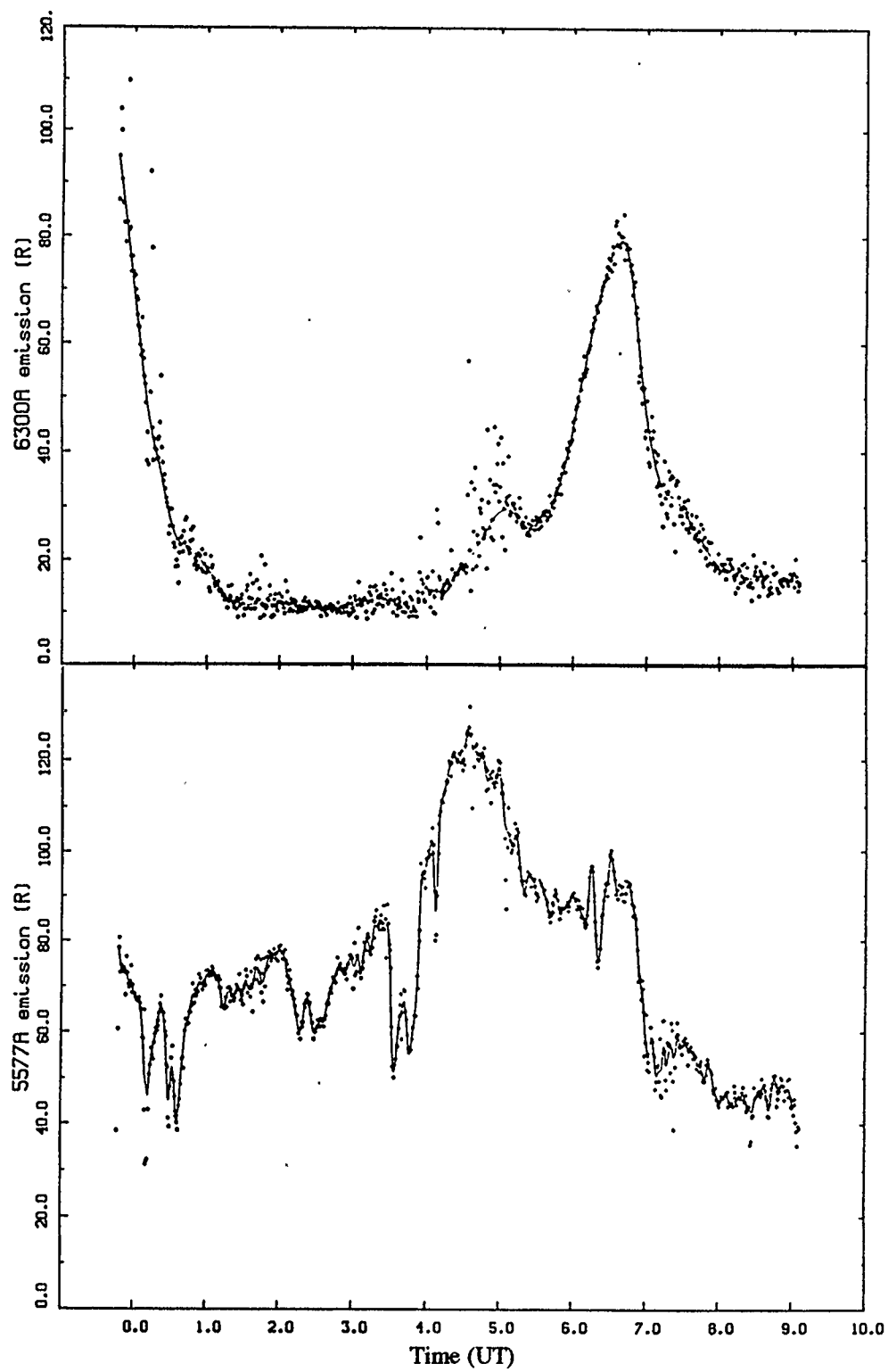
Figure 4.15 Smoothed photometer data from Arecibo – April 23/24, 1985

4.2 Model Atmosphere

In order to calculate expected airglow intensities, some knowledge of (neutral) thermospheric composition and temperature profiles is required. Rocket, satellite and ground-based measurements have enabled the construction of semi-empirical model atmospheres over the last two and a half decades. A recent model, MSIS-83, is based on mass spectrometer and incoherent scatter data from five radar facilities, seven satellites, and a substantial number of rocket flights (Hedin *et al.*, 1983). Given time and location, f107, f107a, and magnetic Ap indices (see table 3.2), values for T_{ex}, temperature profiles, and density profiles of the major neutral species may be obtained for heights greater than 85 km. Alternatively, T_{ex} may be given as input and the model re-evaluated accordingly. If measured values of T_{ex} are available, the latter is considered preferable due to the large amount of averaging inherent in the model.

For the most part, daily Ap indices were used, but another feature of the 1983 model allows the option of using 3-hour Ap values. This option was used for two nights of high activity (Apr 20/21 and Apr 21/22, 1985), when the Ap was seen to fluctuate quite rapidly and severely. See figs. 4.16–4.19 for sample output of the MSIS-83 model.

4.3 Photochemistry of Visible Atomic Oxygen Emissions

The airglow under investigation results from the forbidden transitions of atomic oxygen shown in figure 2.7. In this section equations for calculating the expected brightness of these emissions from measurable quantities will be derived. The method of Cogger *et al.* (1980), in which photochemical equilibrium is assumed, will be followed. The validity of this assumption will be examined later.
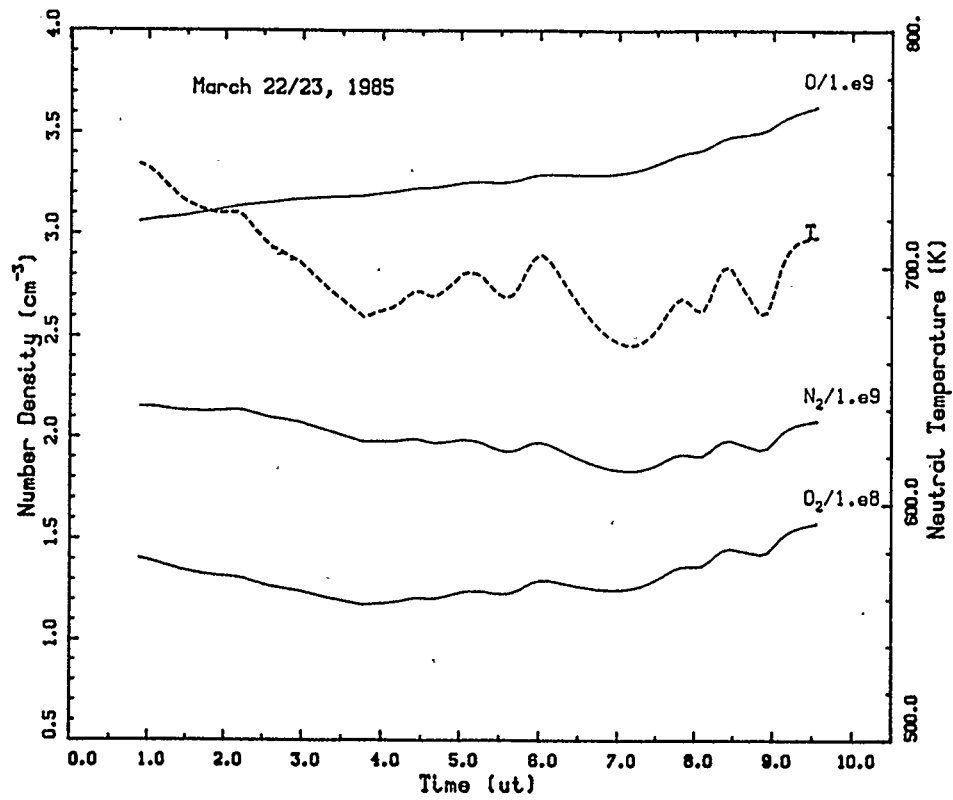
Figure 4.16 Neutral densities at 200 km, MSIS-83 model, $T_{ex} = avTi$
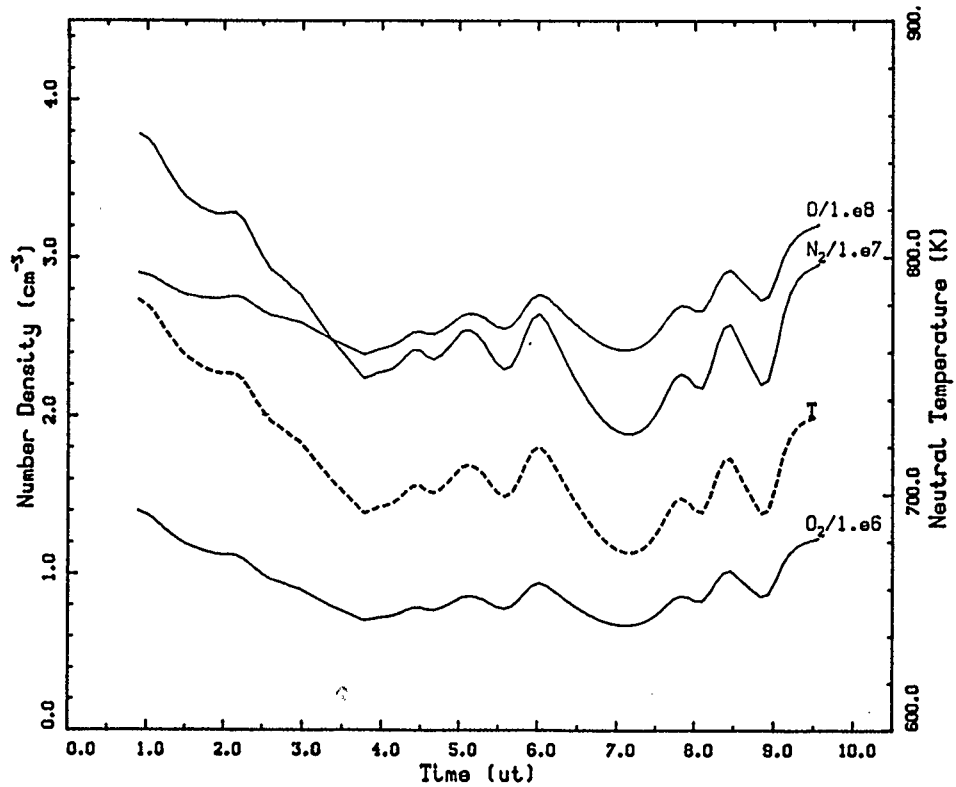
Figure 4.17 As for figure 4.16, at 300 km
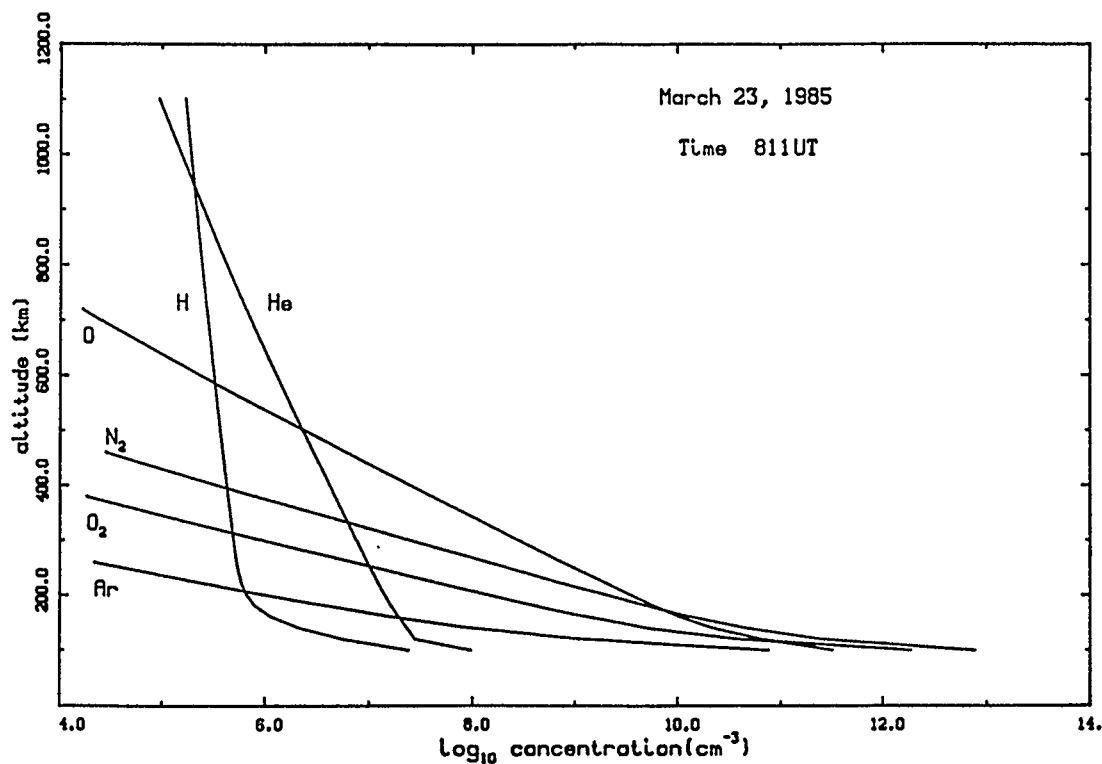
Figure 4.18 Height profiles of neutral constituents from MSIS-83 model
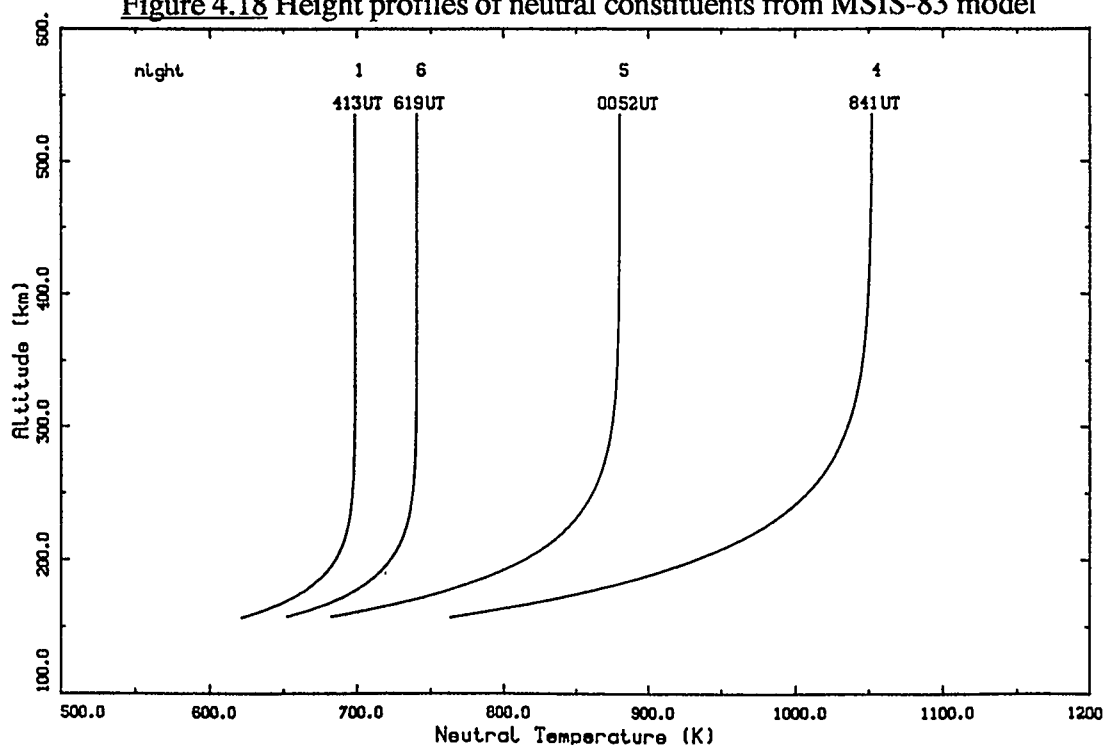
Figure 4.19 Neutral temperature profiles for 4 different times in
March/April 1985 (MSIS-83, T_{ex} = avTi)

As mentioned in section 2.4, the major source of excited oxygen atoms in the nocturnal F region is the dissociative recombination (DR) of ionized molecular oxygen:

$$O_2^+ + e \xrightarrow{\alpha_1} O + O + 6.96 \text{ eV} \qquad (4.3.1)$$

Product atoms may be in the ground state, $O(^3P)$, or may use some of the 6.96 eV excess energy to attain excited states $O(^1D)$ or $O(^1S)$. Efficiencies of production of the excited states (average number of atoms in each state resulting from one DR reaction) are β_{1D} and β_{1S} respectively. The rate at which reaction (4.3.1) proceeds is determined by the rate constant, α_1, and the concentrations of the reactants, $[O_2^+]$ and $[e]$.

Excited atoms are returned to the ground state either through emission of radiation or by collisional de-activation (quenching). The latter is considered unimportant for F region $O(^1S)$ atoms, which have lifetimes ≤ 1 s, but is a major sink for $O(^1D)$ atoms with lifetimes on the order of 10^2 s. Probability of photon emission per unit time (in the absence of quenching) is given by the Einstein coefficients A_{6300}, A_{5577}, etc. Under most quiet conditions, this mechanism has been adequate to explain observed 6300 Å airglow intensities, within experimental uncertainties (Wickwar *et al.*, 1974; Cogger *et al.*, 1974; Link and Cogger, 1988).

With production of $O(^1D)$ and $O(^1S)$ chiefly through (4.3.1), loss mechanisms may be summarized as follows.

$$O(^1S) \xrightarrow{A_{5577}} O(^1D) + 5577 \text{ Å} \quad [\text{minor source of } O(^1D)] \qquad (4.3.2)$$

$$O(^1S) \xrightarrow{A_{2972}} O(^3P) + 2972 \text{ Å} \qquad (4.3.3)$$

$$O(^1D) \xrightarrow{A_{1D}} O(^3P) + 6300/6364 \text{ Å} \qquad (4.3.4)$$

$$O(^1D) + N_2 \xrightarrow{\alpha_3} O(^3P) + N_2 \qquad (4.3.5)$$

$$O(^1D) + O_2 \xrightarrow{\alpha_4} O(^3P) + O_2 \qquad (4.3.6)$$

$$O(^1D) + O \xrightarrow{\alpha_5} O(^3P) + O \qquad (4.3.7)$$

$$O(^1D) + e \xrightarrow{k_5} O(^3P) + e \qquad (4.3.8)$$
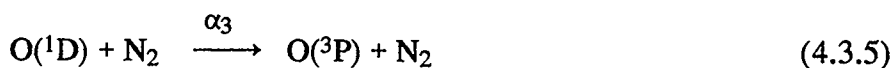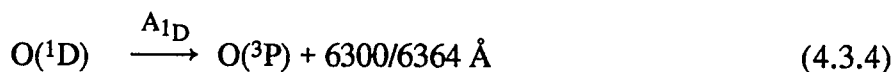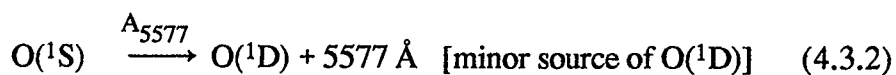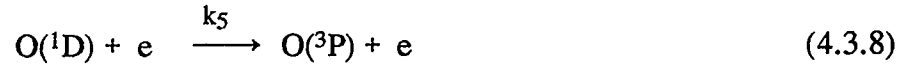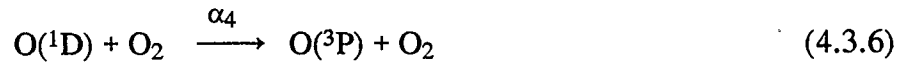
where $A_{1D} = A_{6300} + A_{6364}$ and $A_{1S} = A_{5577} + A_{2972}$.

For a steady state (equilibrium) solution, production and loss terms may be equated to derive the resulting abundance of each species, *i.e.*,

$$[O(^1D)] = \frac{\alpha_1 \beta_{1D}[O_2^+][e]}{A_{1D} + Q} \qquad (4.3.9)$$

where $Q = \alpha_3[N_2] + \alpha_4[O_2] + \alpha_5[O] + k_5[e]$ (quenching terms), and

$$[O(^1S)] = \frac{\alpha_1 \beta_{1S}[O_2^+][e]}{A_{1S}} \qquad (4.3.10)$$

Since the concentration of O_2^+ cannot be directly measured from the ground, some further assumptions must be made. Through most of the F region, O^+ is the major ion, so $[O^+] \approx [e]$. Heavier ions become significant at lower altitudes (below about 250 km), and it is assumed for the lower F region that (Cogger *et al.*, 1980)

$$[e] = [O^+] + [NO^+] + [O_2^+] \qquad (4.3.11)$$

From section 2.4, the major sources and sinks of these ions are the following:

O_2^+:
$$O^+ + O_2 \xrightarrow{k_1} O_2^+ + O \quad \text{(sink for } O^+\text{)} \qquad (4.3.12)$$

$$O_2^+ + N \xrightarrow{k_4} NO^+ + O \qquad (4.3.13)$$

$$O_2^+ + e \xrightarrow{\alpha_1} O + O \qquad (4.3.1)$$

$\text{NO}^+:$ $\qquad \text{O}^+ + \text{N}_2 \xrightarrow{k_2} \text{NO}^+ + \text{N} \quad (\text{sink for O}^+)$ $\qquad\qquad$ (4.3.14)

$$\text{O}_2^+ + \text{N} \xrightarrow{k_4} \text{NO}^+ + \text{O} \qquad\qquad (4.3.13)$$

$$\text{NO}^+ + e \xrightarrow{\alpha_2} \text{N} + \text{O} \qquad\qquad (4.3.15)$$
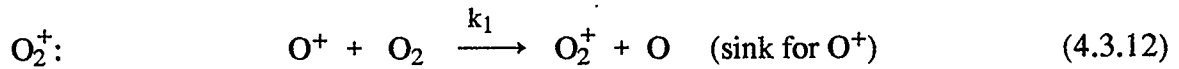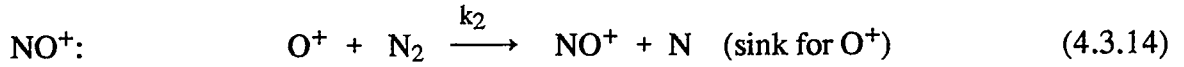
Not all of the above reactions are considered important by all authors. For this study, some recent determinations of the rate constants were obtained from the review by Sharp (1986). These are listed in Table 4.1, along with the more recent set of Link and Cogger (1988) for comparison. Figure 4.20 shows the temperature dependence of some of these coefficients.

To obtain expressions for the required concentrations, production and loss terms for each ion were equated, with the following results.

$$[\text{O}_2^+] = \frac{k_1[\text{O}^+][\text{O}_2]}{k_4[\text{N}] + \alpha_1[e]} \qquad\qquad (4.3.16)$$

$$[\text{NO}^+] = \frac{k_2[\text{O}^+][\text{N}_2] + k_4[\text{O}_2^+][\text{N}]}{\alpha_2[e]} \qquad\qquad (4.3.17)$$

Now (4.3.11) may be rewritten thus:

$$[e] = [\text{O}^+] + [\text{NO}^+] + [\text{O}_2^+]$$

$$= [\text{O}^+]\left\{ 1 + \frac{k_1[\text{O}_2]}{k_4[\text{N}] + \alpha_1[e]} + \frac{k_2[\text{N}_2] + k_4[\text{O}_2^+][\text{N}]/[\text{O}^+]}{\alpha_2[e]} \right\}$$

$$= [\text{O}^+]\left\{ 1 + \frac{k_1[\text{O}_2]}{k_4[\text{N}] + \alpha_1[e]}\left(1 + \frac{k_4[\text{N}]}{\alpha_2[e]} \right) + \frac{k_2[\text{N}_2]}{\alpha_2[e]} \right\}.$$

With the definition $B = [\text{O}^+]/[e]$, a quantity which is close to unity in most of the F region, (4.3.16) and (4.3.9) become

$$[\text{O}_2^+] = \frac{k_1[\text{O}_2][e] B}{k_4[\text{N}] + \alpha_1[e]} \qquad\qquad (4.3.19)$$
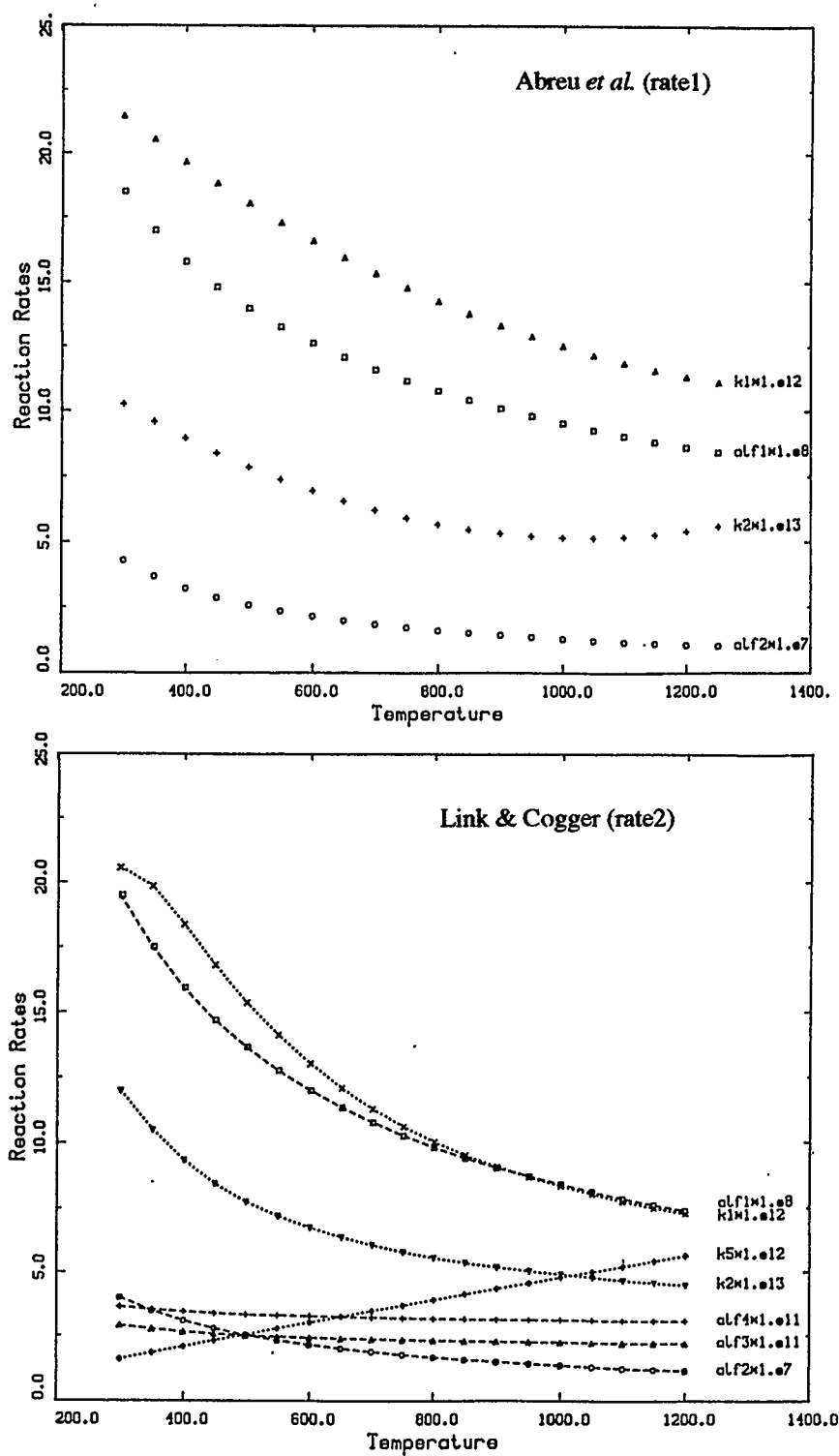
Figure 4.20 Temperature dependence of reaction rate coefficients

Table 4.1 F-Region Reaction Rate Coefficients

$$(t_i = T_i/300; \quad t_e = T_e/300; \quad t = T_n/300)$$

Reaction	Link & Cogger, 1988 (rate2)	Present Study (rate1)	Reference
	Rate Coefficient (cm³ s⁻¹)		
(4.3.1) α_1	$1.95 \times 10^{-7} t_e^{-0.7}$ ($\beta_{1D} = 1.1$)	$1.85 \times 10^{-7} t_e^{-0.55}$ ($\beta_{1D} = 1.2$)	Sharp (1986)
(4.3.5) α_3	$2.0 \times 10^{-11} e^{111.8/T_n}$	2.3×10^{-11}	
(4.3.6) α_4	$2.9 \times 10^{-11} e^{67.5/T_n}$	4.0×10^{-11}	
(4.3.7) α_5	...	8×10^{-12}	
(4.3.8) k_5	$1.6 \times 10^{-12} t_e^{0.91}$	...	
(4.3.12) k_1	$3.23 \times 10^{-12} e^{(3.72/t_i - 1.87/t_i^2)}$	$2.82 \times 10^{-11} - 7.74 \times 10^{-12} t + 1.073 \times 10^{-12} t^2 - 5.17 \times 10^{-14} t^3 + 9.65 \times 10^{-16} t^4$	Cogger et al. (1980)
(4.3.13) k_4	...	1.8×10^{-10}	
(4.3.14) k_2	$2.78 \times 10^{-13} e^{(2.07/t_i - 0.61/t_i^2)}$	$1.533 \times 10^{-12} - 5.92 \times 10^{-13} t + 8.60 \times 10^{-14} t^2$	
(4.3.15) α_2	$4.00 \times 10^{-7} t_e^{-0.9}$	$4.3 \times 10^{-7} t_e^{-1}$	Sharp (1986)

Atomic Transition	Einstein Coefficient (s⁻¹)		Reference
(4.3.2) A_{5577}	...	1.06	Sharp (1986)
(4.3.3) A_{2792}		0.045	
(4.3.4) A_{6300}	.00563	.00515	Link et al. (1981)
A_{1D}	.00745	.00681	

and
$$[O(^1D)] = \frac{\alpha_1 \beta_{1_D} k_1 [O_2][e] B[e]/(k_4[N] + \alpha_1[e])}{A_{1_D} + Q}$$

$$= \frac{\beta_{1_D} k_1 [O_2][e] B/\left(1 + \frac{k_4[N]}{\alpha_1[e]}\right)}{A_{1_D} + Q}$$

or
$$[O(^1D)] = \frac{\beta_{1_D} k_1 [O_2][e] BF}{A_{1_D} + Q} \qquad (4.3.20)$$

where
$$F = \left(1 + \frac{k_4[N]}{\alpha_1[e]}\right)^{-1}.$$

The volume emission rate for each wavelength is the Einstein probability multiplied by the number density of the relevant species:

$$\eta_{6300} = A_{6300} [O(^1D)] \qquad (4.3.21)$$

Let $D = \dfrac{A_{6300}}{A_{1_D} + \alpha_3[N_2] + \alpha_4[O_2] + \alpha_5[O] + k_5[e]}$ = fraction of $O(^1D)$ atoms which emit

6300 Å radiation. Then

$$\eta_{6300} = \beta_{1_D} k_1 [O_2][e] BDF \qquad (4.3.22)$$

Likewise,
$$\eta_{5577} = A_{5577} [O(^1S)]$$

$$= \frac{A_{5577}}{A_{1_S}} \alpha_1 \beta_{1_S} [O_2^+][e]$$

$$= \frac{A_{5577}}{A_{1_S}} \alpha_1 \beta_{1_S} [O_2][e] BF \qquad (4.3.23)$$

These expressions are then integrated over height to obtain column intensities as observed from the Earth's surface. Neutral densities are taken from the MSIS-83 model, with the exception of atomic nitrogen, which is assumed to be in diffusive equilibrium with the value $[N] = 1.5 \times 10^7$ cm^{-3} at a height of 200 km (Cogger et al., 1980).
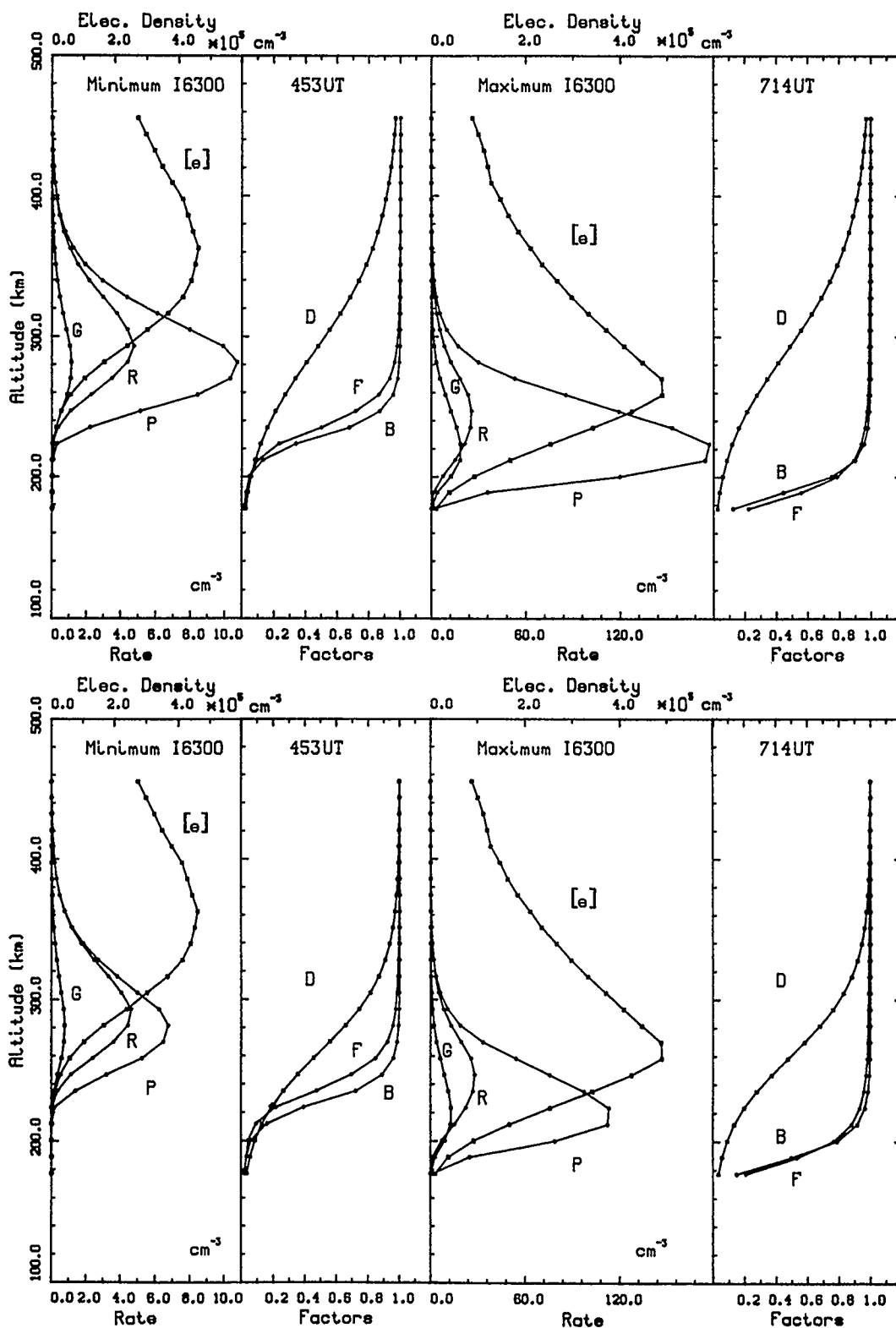
Figure 4.21 Airglow emission rate profiles and contributing factors for March 3/4 1971. G = 5577 Å emission rate, R = 6300 Å emission rate, P = O(^{1}D) production rate, [e] = electron concentration (other parameters defined in text). Top: rates compiled for this work. Bottom: Link and Cogger rates.
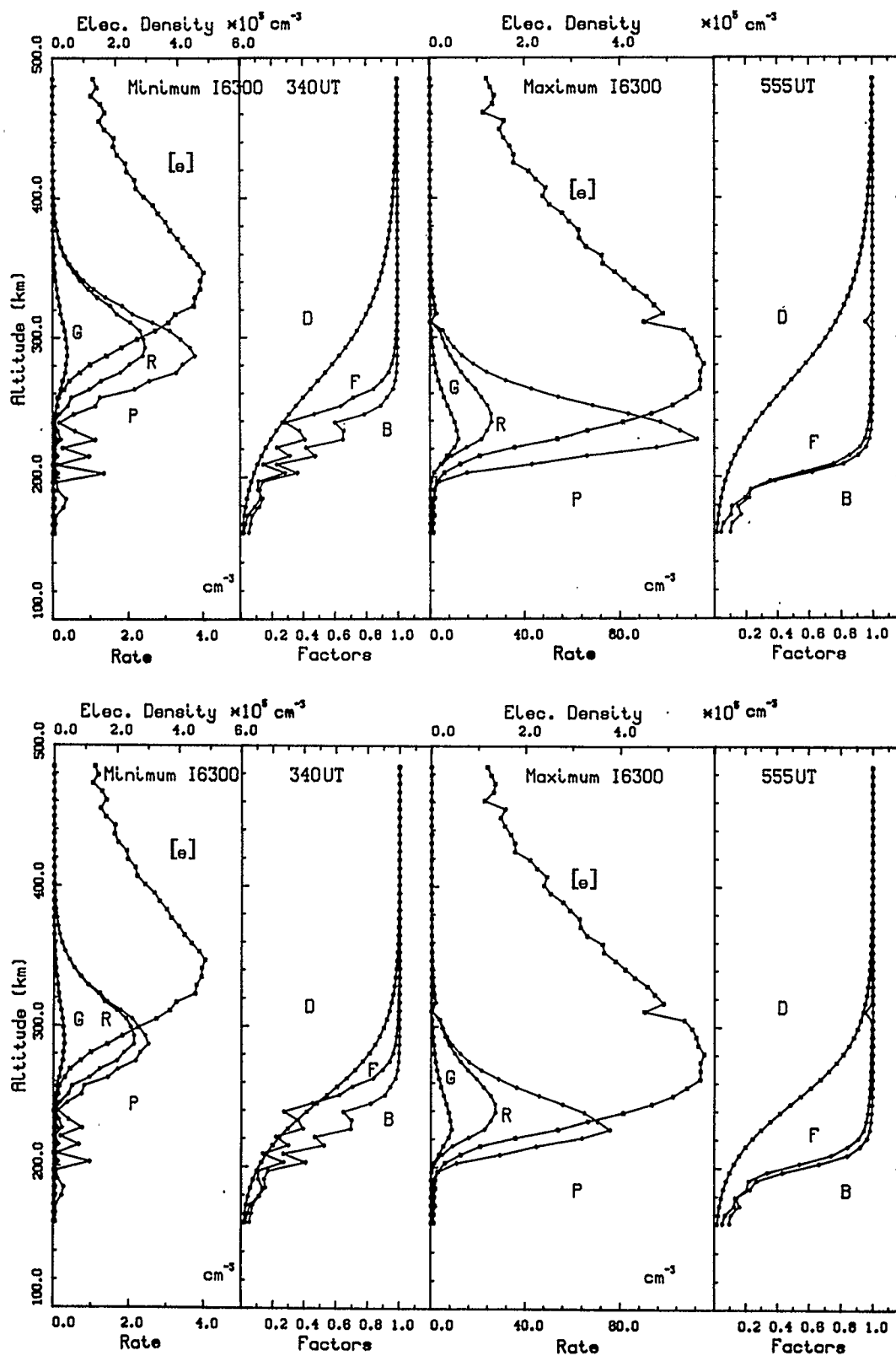
Figure 4.22 As in figure 4.21, but for April 25/26, 1976.
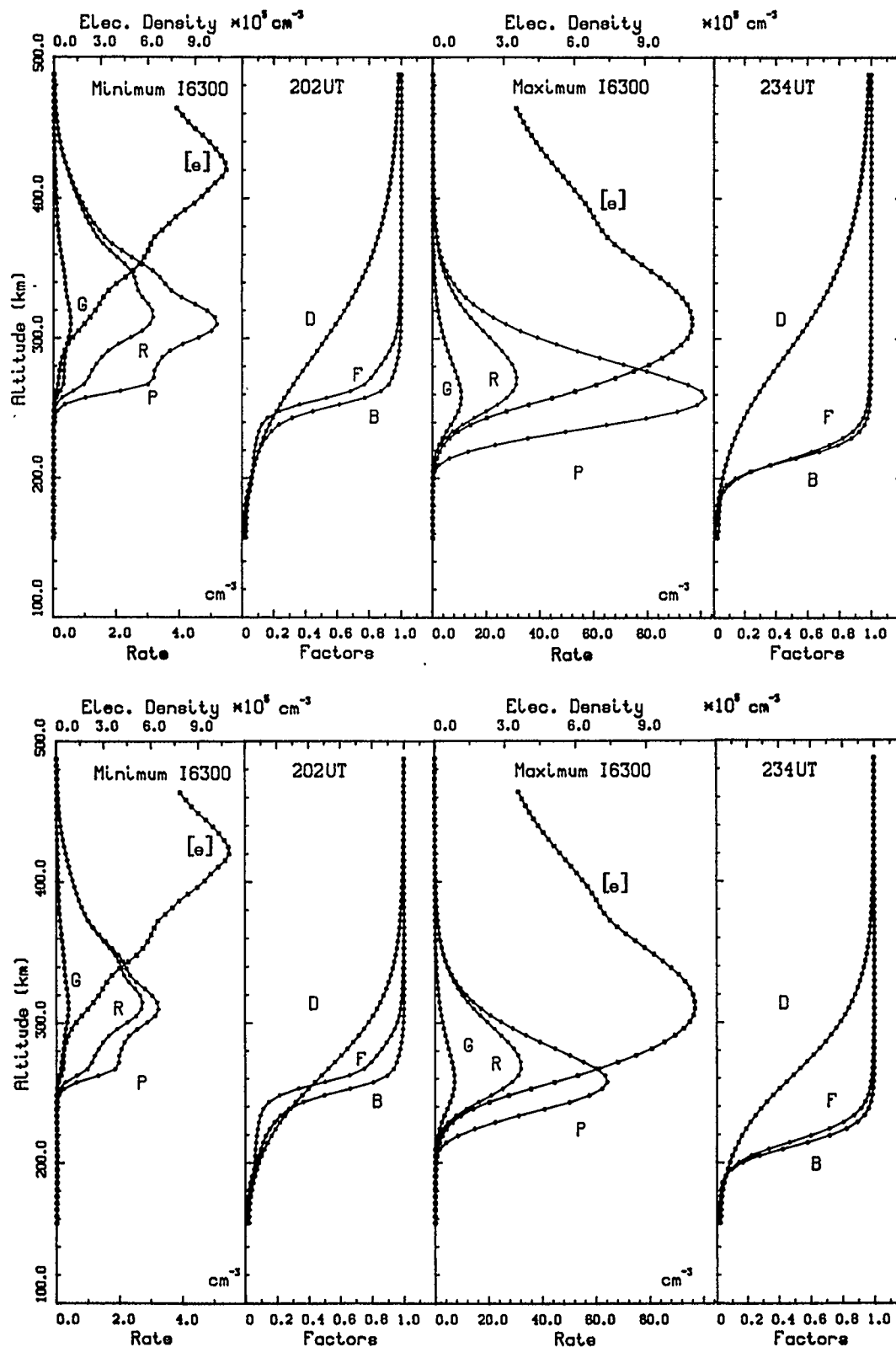
Figure 4.23 As in figure 4.21, but for April 20/21, 1985.
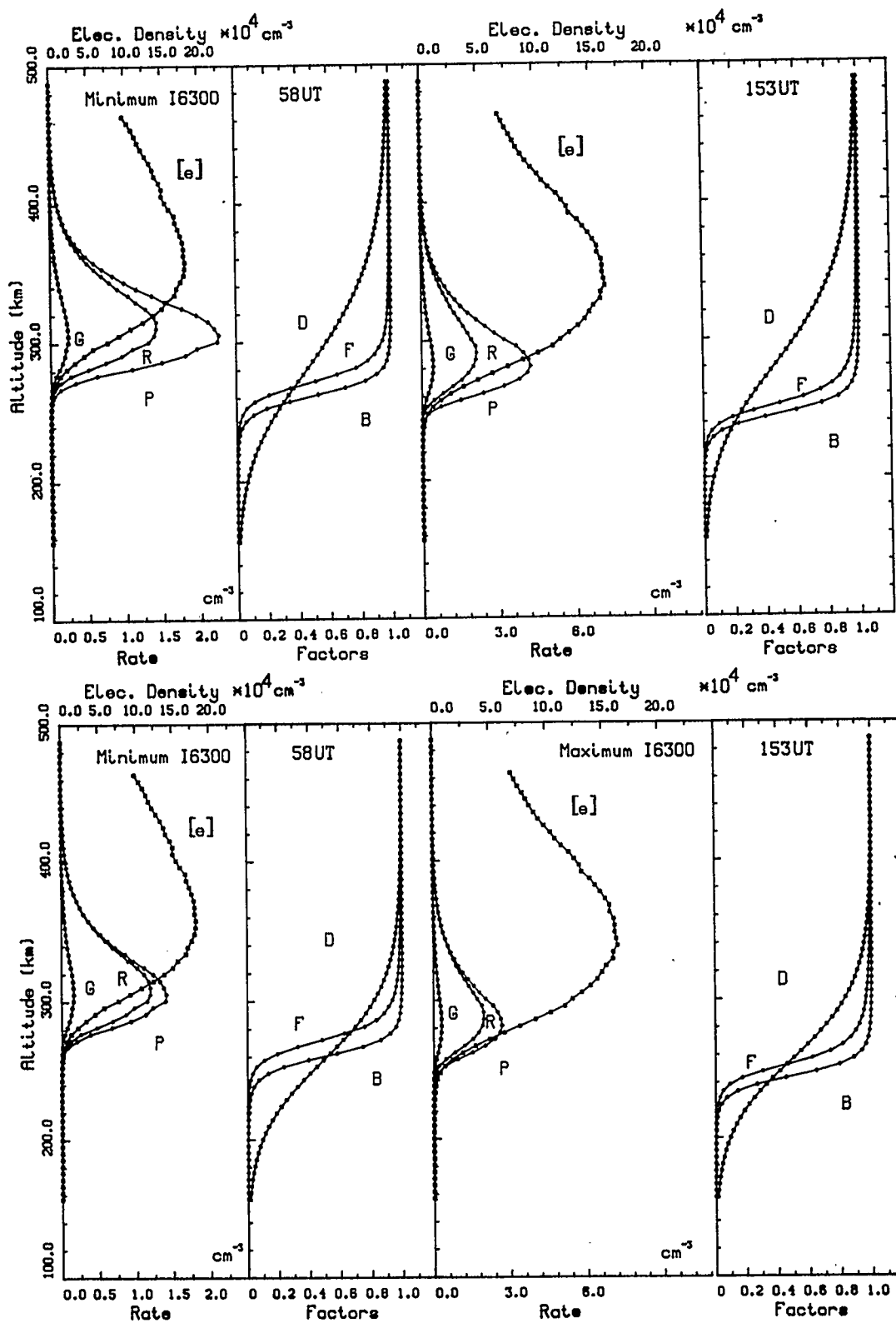
Figure 4.24 As in figure 4.21, but for April 21/22, 1985.

Some sample altitude profiles of the factors B, D, and F, together with calculated emission rates, are given in figures 4.21–4.24.

4.4 Atmospheric Extinction and Contamination

Since the light is emitted some distance above the Earth's surface, it will undergo some scattering and absorption before reaching the photometers at Arecibo. The magnitude of this extinction would be quite similar to that of starlight passing through the Earth's atmosphere, but since airglow is emitted from an extended source, light may be scattered into, as well as out of, the field of view. A description of the radiative transfer relevant to airglow photometery may be found in Chamberlain (1961).

In general, there are too many unknowns to calculate the extinction coefficient for airglow on a given night. It would be helpful to have measurements of point source (starlight) extinction taken several times during airglow observations (Rao and Kulkarni, 1973), but these are not generally available. For practical purposes, Torr et al. (1977) calculated a minimum net extinction for a clear sky over Arecibo of 20%, in agreement with a previous value used by Cogger et al. (1980). The calculated brightnesses at 6300 Å will therefore be reduced by 20% for comparison with observed values. This value should perhaps be somewhat higher for 5577 Å emissions (Ahlquist and Charlson, 1969), but the difference would be insignificant relative to calibration uncertainties (sec 3.3).

Another factor to be considered is contamination of the photometric measurements by emission features at nearby wavelengths. This problem has been investigated by Hernandez (1974) and Burnside et al. (1977) for the case of the oxygen red line. Contamination at this wavelength is mainly due to molecular bands of OH, originating in

the mesosphere. From fig. 2 of Burnside *et al.*, it may be deduced that for intensities in the region of 10-50 R, a bandwidth of 6 Å results in an overestimation of 6300 Å brightness by about 2.5 R. The data from the 1970s used in this study had already been corrected by 5 R (Cogger *et al.*, 1980), and these were not changed. Due to the smaller value suggested by Burnside *et al.*, the 1985 data were not initially corrected for contamination. Rather, a small intercept was anticipated when plotting calculated *vs.* observed brightnesses. These plots, however, revealed substantially larger intercepts than expected based on the above, generally in the 5-10 R range. In the interest of consistency, the original 5 R correction was also applied to the more recent data.

4.5 Photochemical Model Results

The results of this equilibrium model are illustrated for most of the 1971/1976 data in figs. 4.25–4.32. It is evident that the general trends in the photometer data are well represented by the model, in accordance with earlier work. In these figures, model calculations using both measured ion temperatures and MSIS-83 exospheric temperature values are shown, for the original set of reaction rate coefficients compiled for this work (rate 1). There is little difference in the results, but for some nights the MSIS-83 temperatures, somewhat surprisingly, yield intensity values closer to those observed. This is particularly true for the 1971 data, including June 2/3, 1971, a night of some magnetic disturbance.

The very close agreement between calculated and observed 6300 Å brightness seen for the 1976 data seems to resolve one of the two major discrepancies found by Cogger *et al.* in 1980. Clearly, use of the new rate coefficients, in combination with the MSIS-83 model atmosphere, yields quite satisfactory calculations of 6300 Å brightnesses based on the same equilibrium model used by Cogger *et al.*
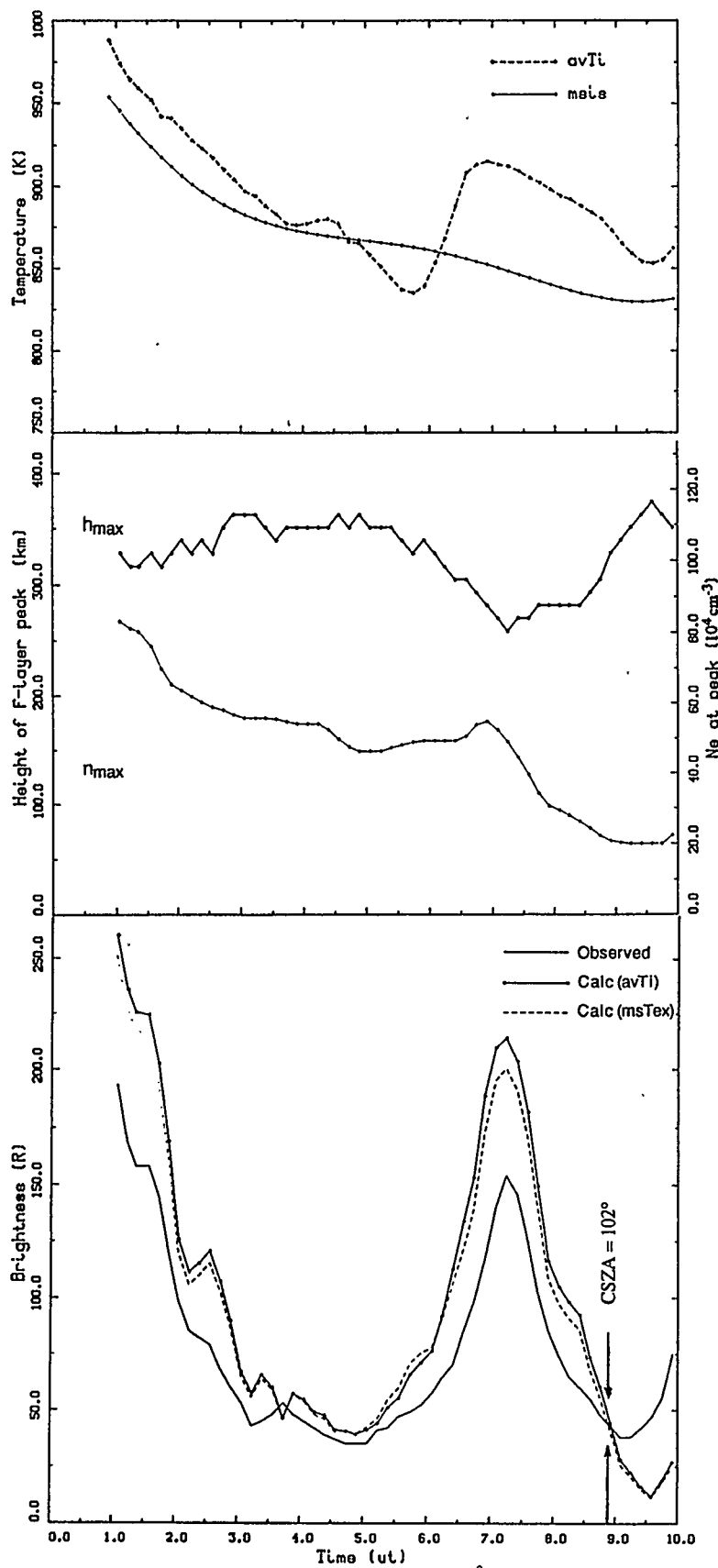
Figure 4.25 F-region parameters and 6300 Å brightness, March 3/4, 1971.
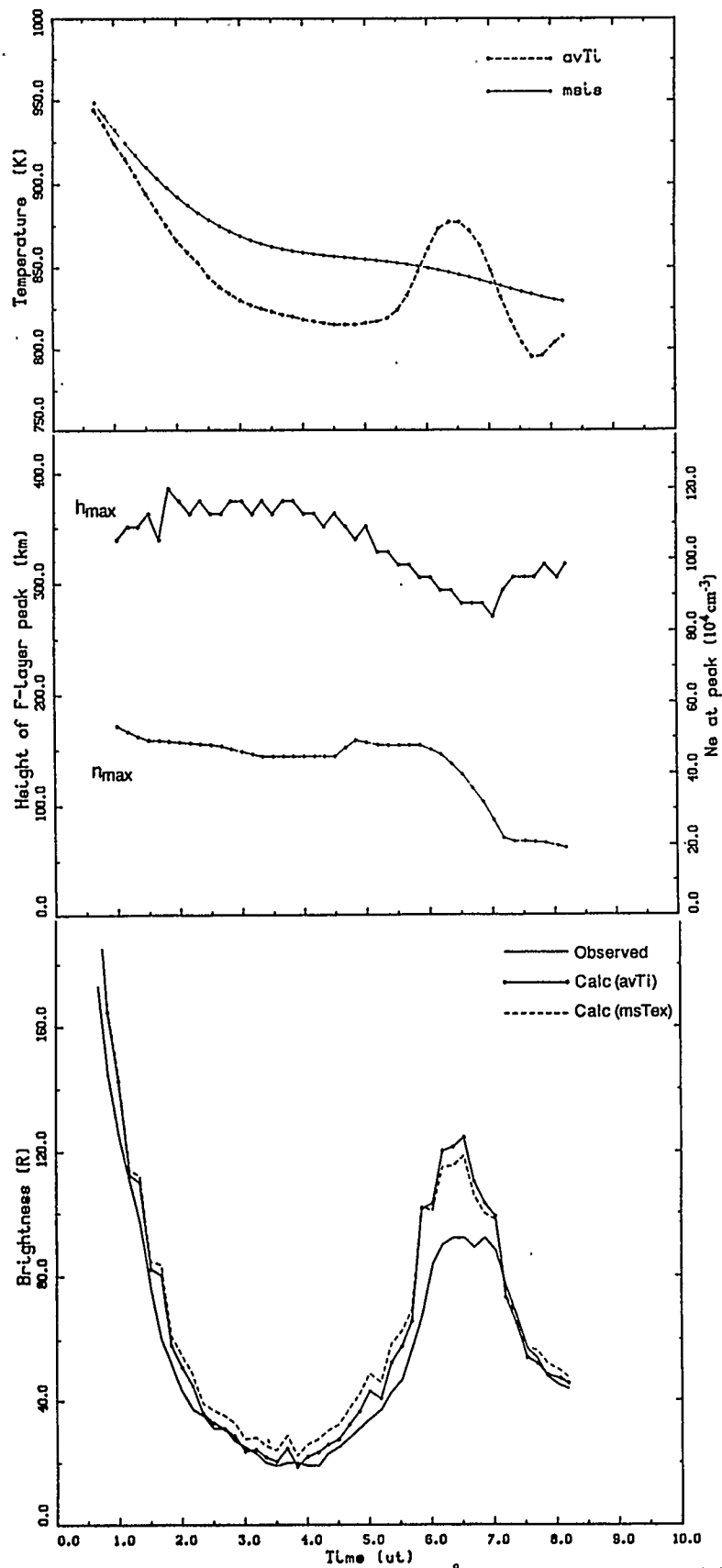
<u>Figure 4.26</u> F-region parameters and 6300 Å brightness, March 26/27, 1971.
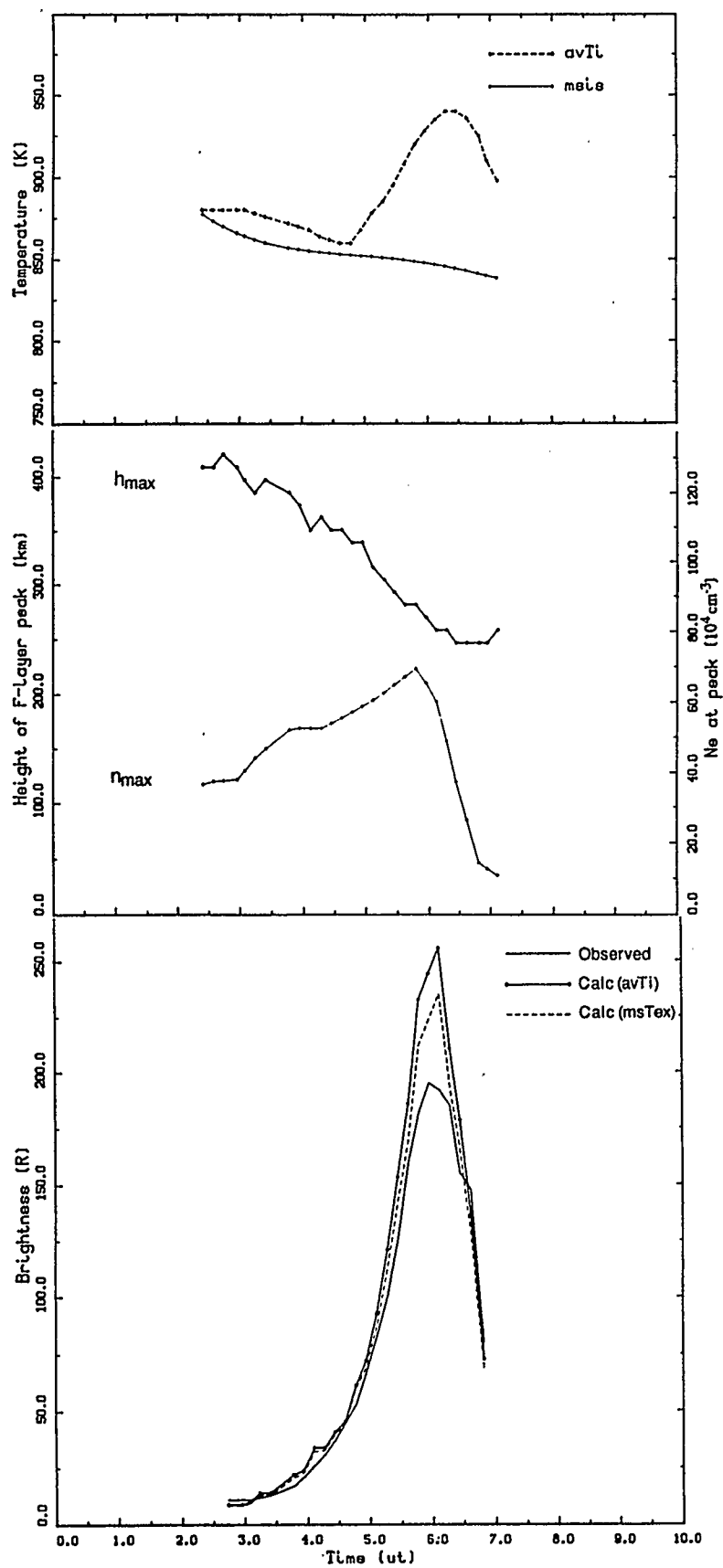
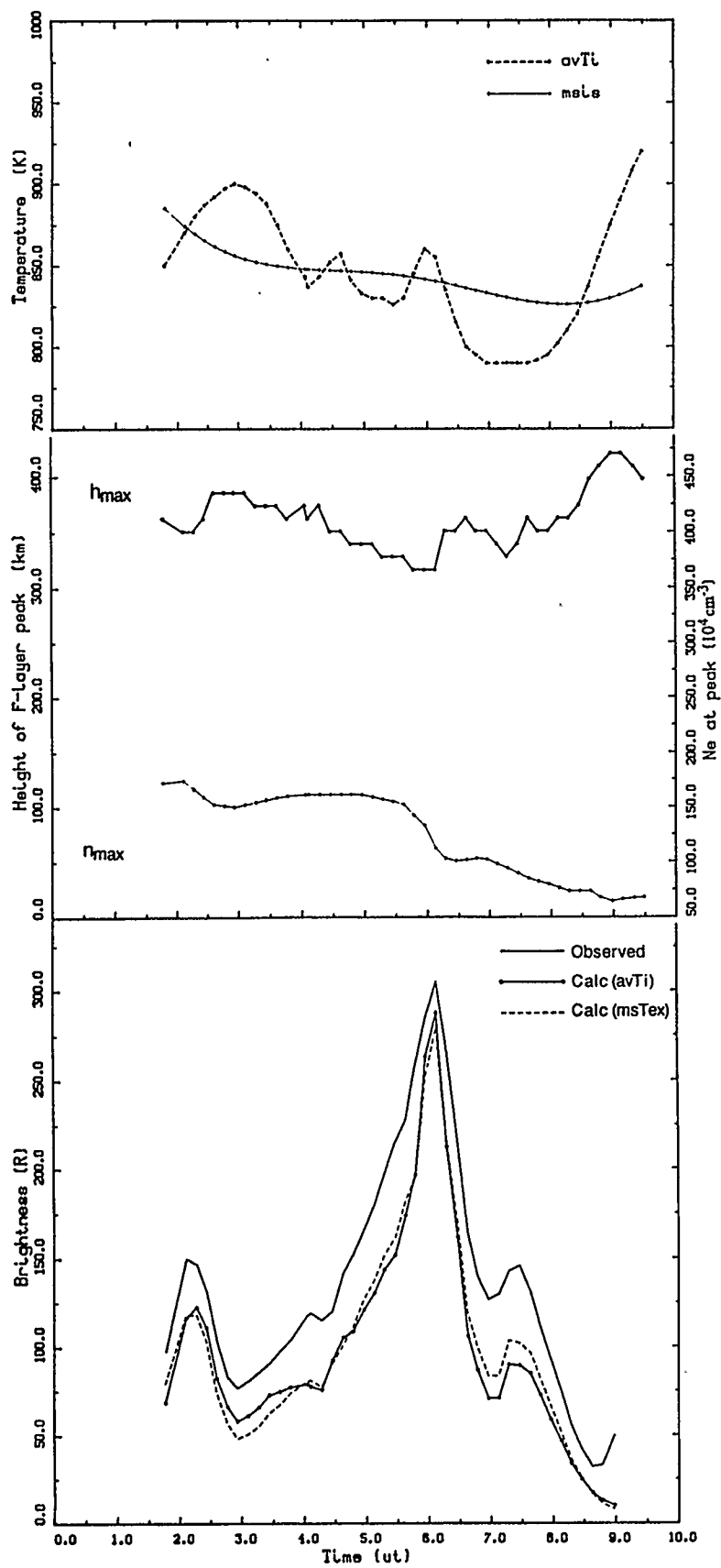Figure 4.27 F-region parameters and 6300 Å brightness, March 31/April 1, 1971.

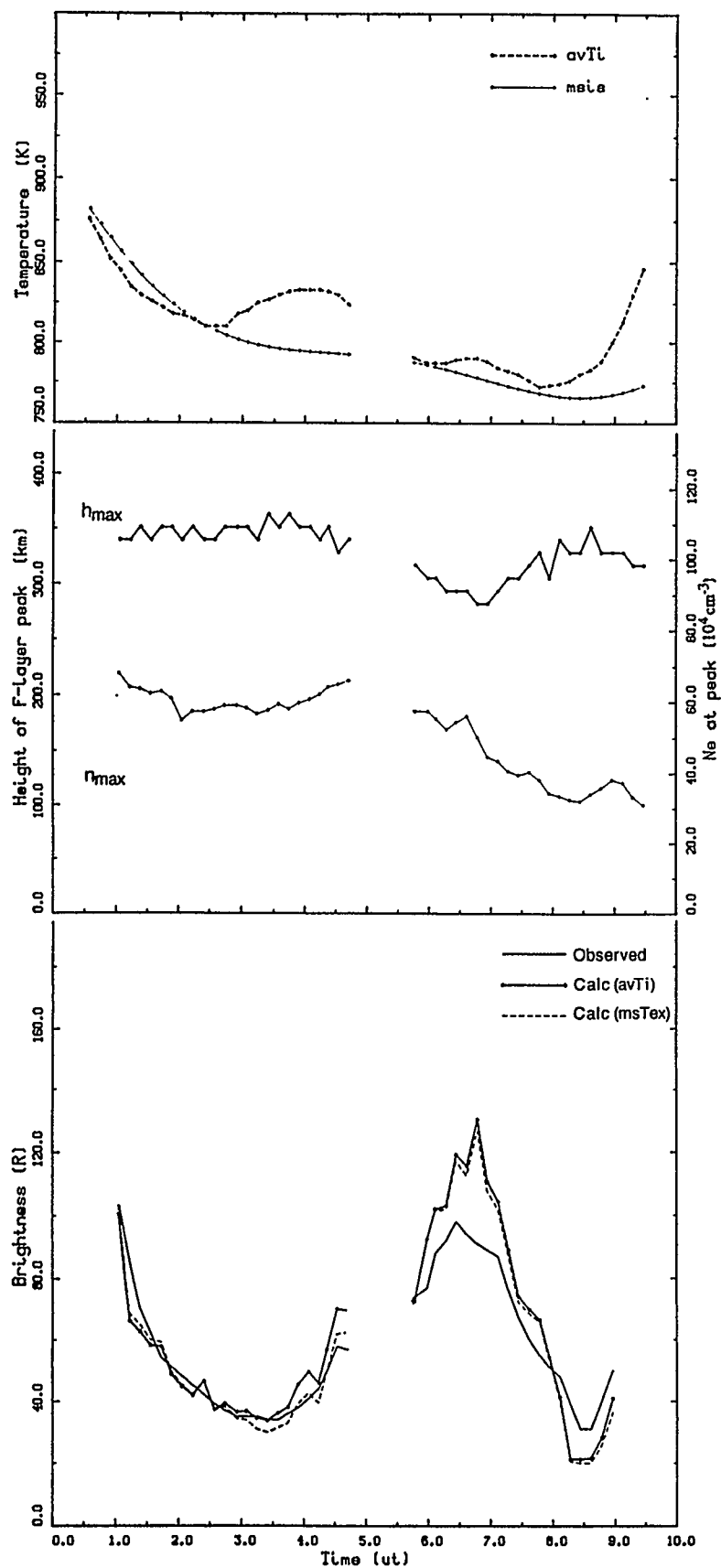Figure 4.28 F-region parameters and 6300 Å brightness, June 2/3, 1971.

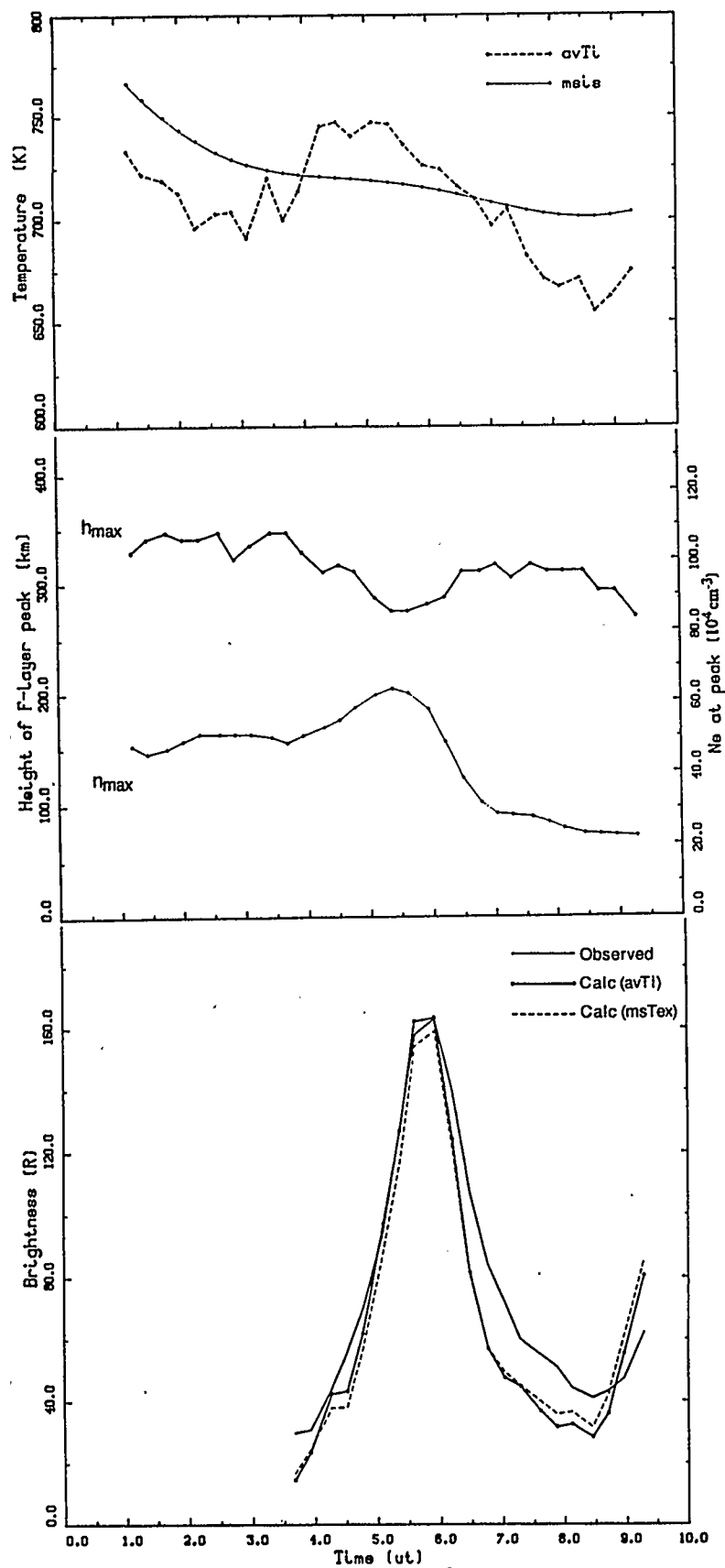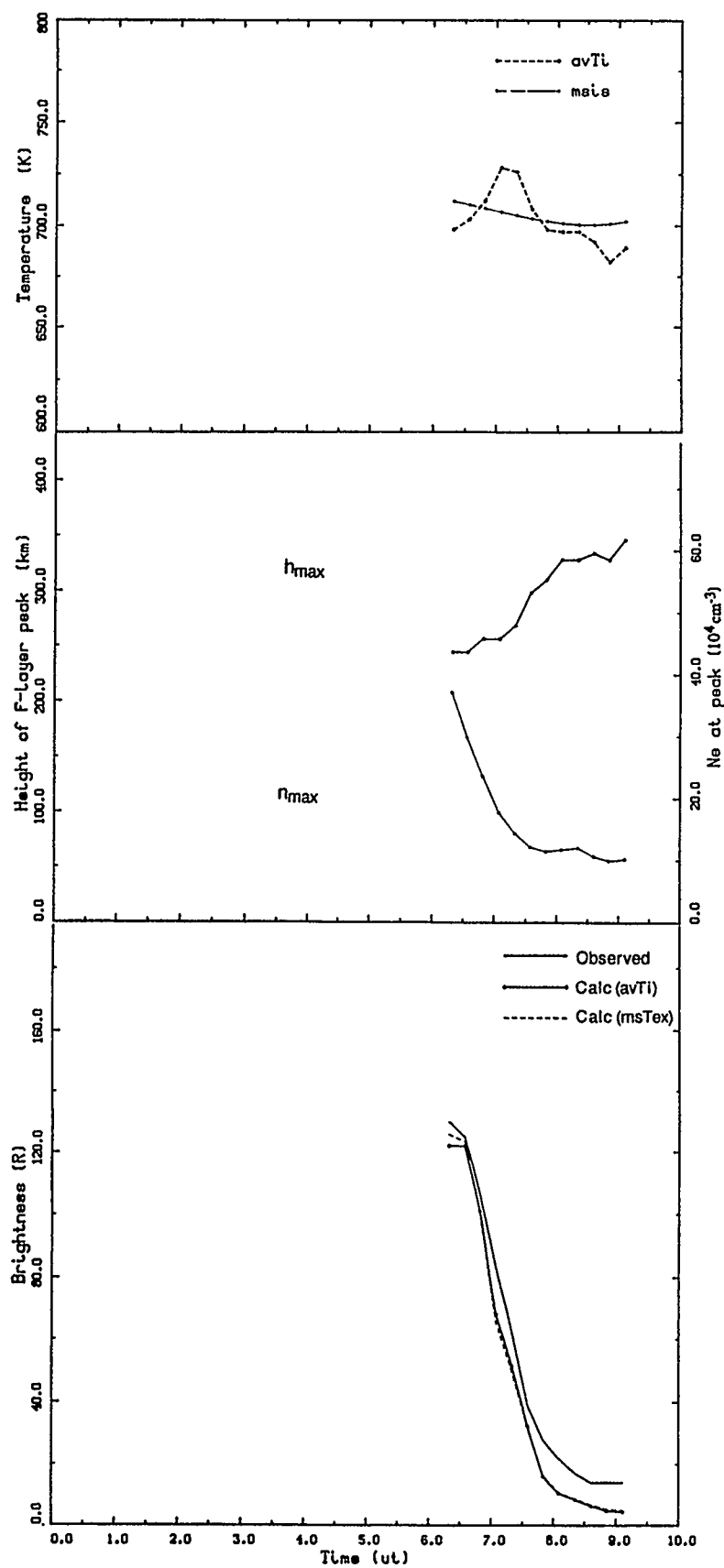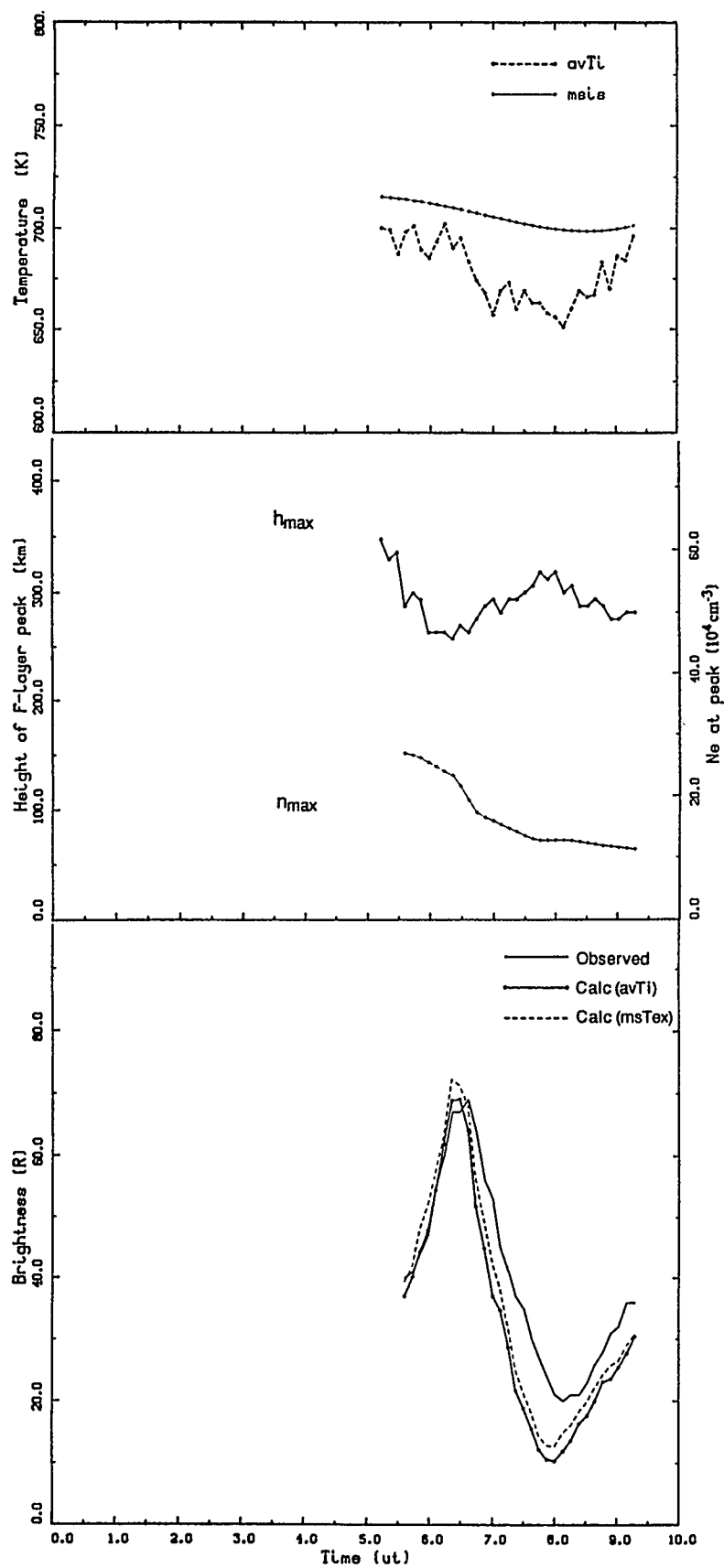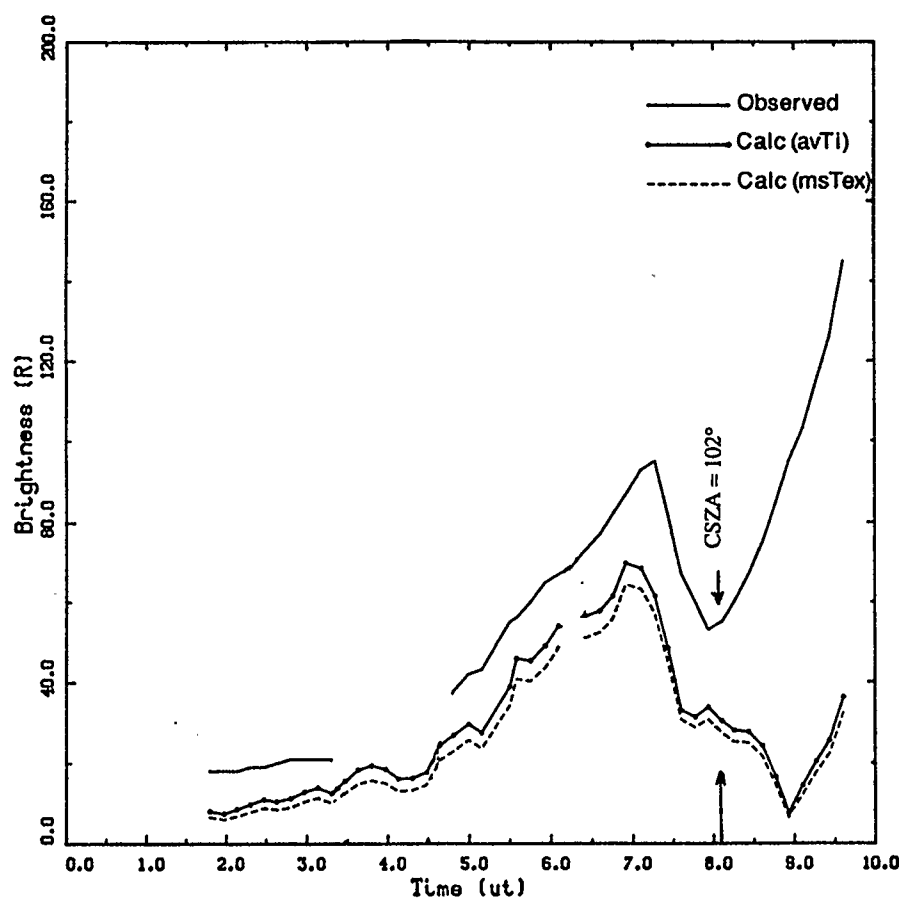Figure 4.29 F-region parameters and 6300 Å brightness, June 16/17, 1971.

Figure 4.30 F-region parameters and 6300 Å brightness, April 25/26, 1976.

Figure 4.31 F-region parameters and 6300 Å brightness, April 27/28, 1976.

Figure 4.32 F-region parameters and 6300 Å brightness, April 28/29, 1976.

Figure 4.33 Observed and model 6300 Å brightness, Oct. 18/19, 1971.
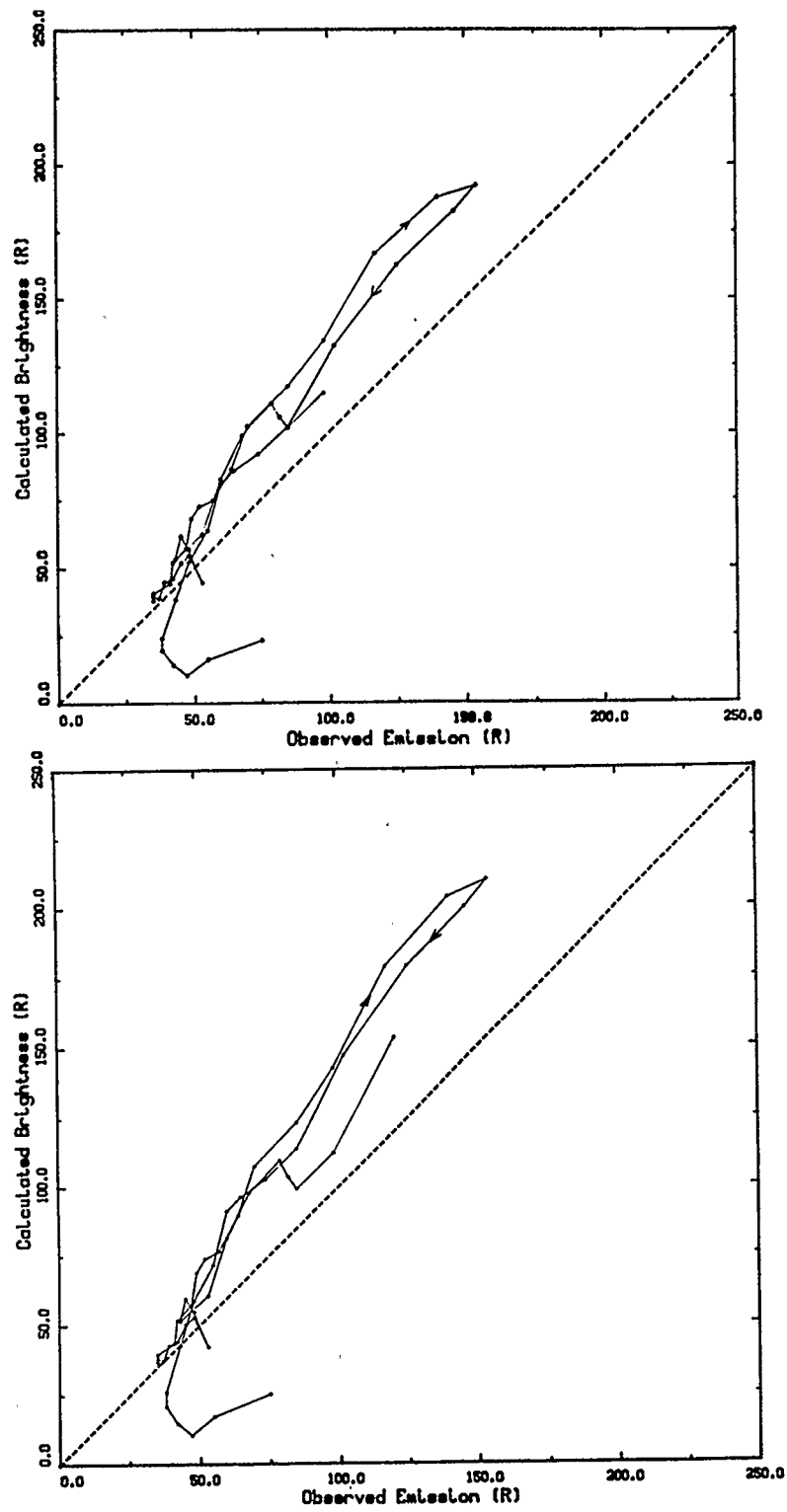
Figure 4.34 Calculated *vs.* Observed 6300 Å brightness, March 3/4, 1971.
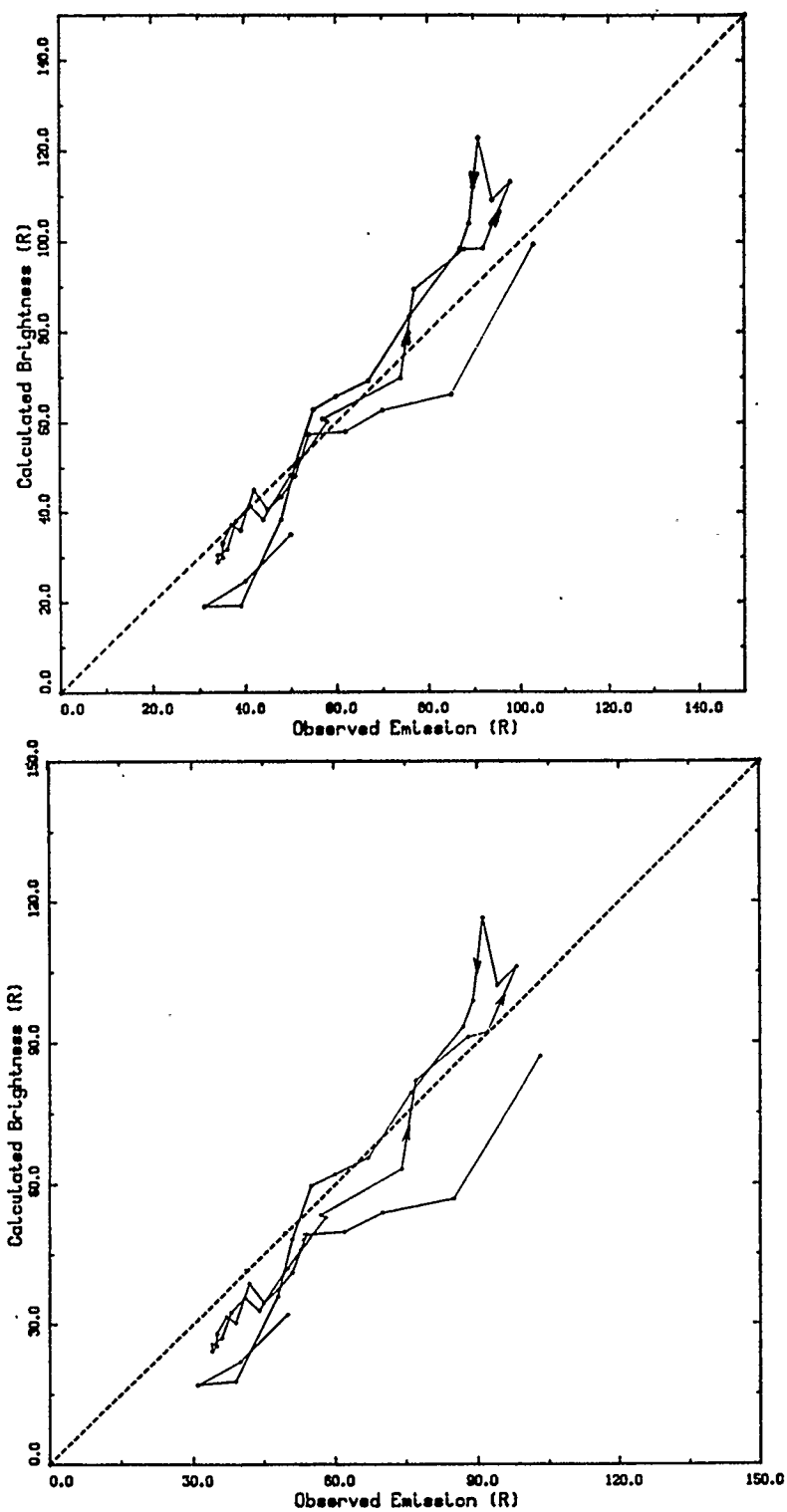Top: rate1. Bottom: rate2.
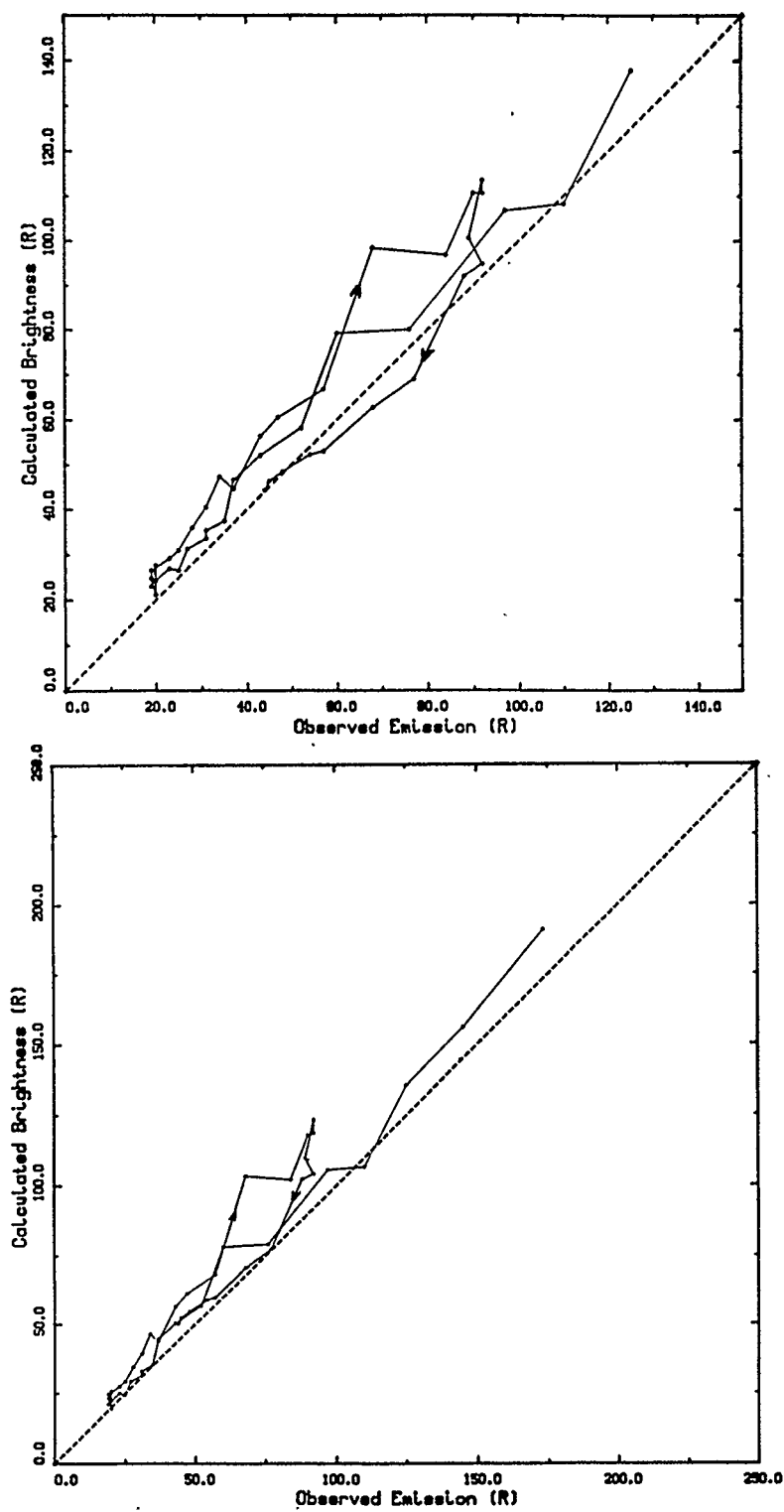
Figure 4.35 Calculated *vs.* Observed 6300 Å brightness, March 26/27, 1971.
Top: rate1. Bottom: rate2.
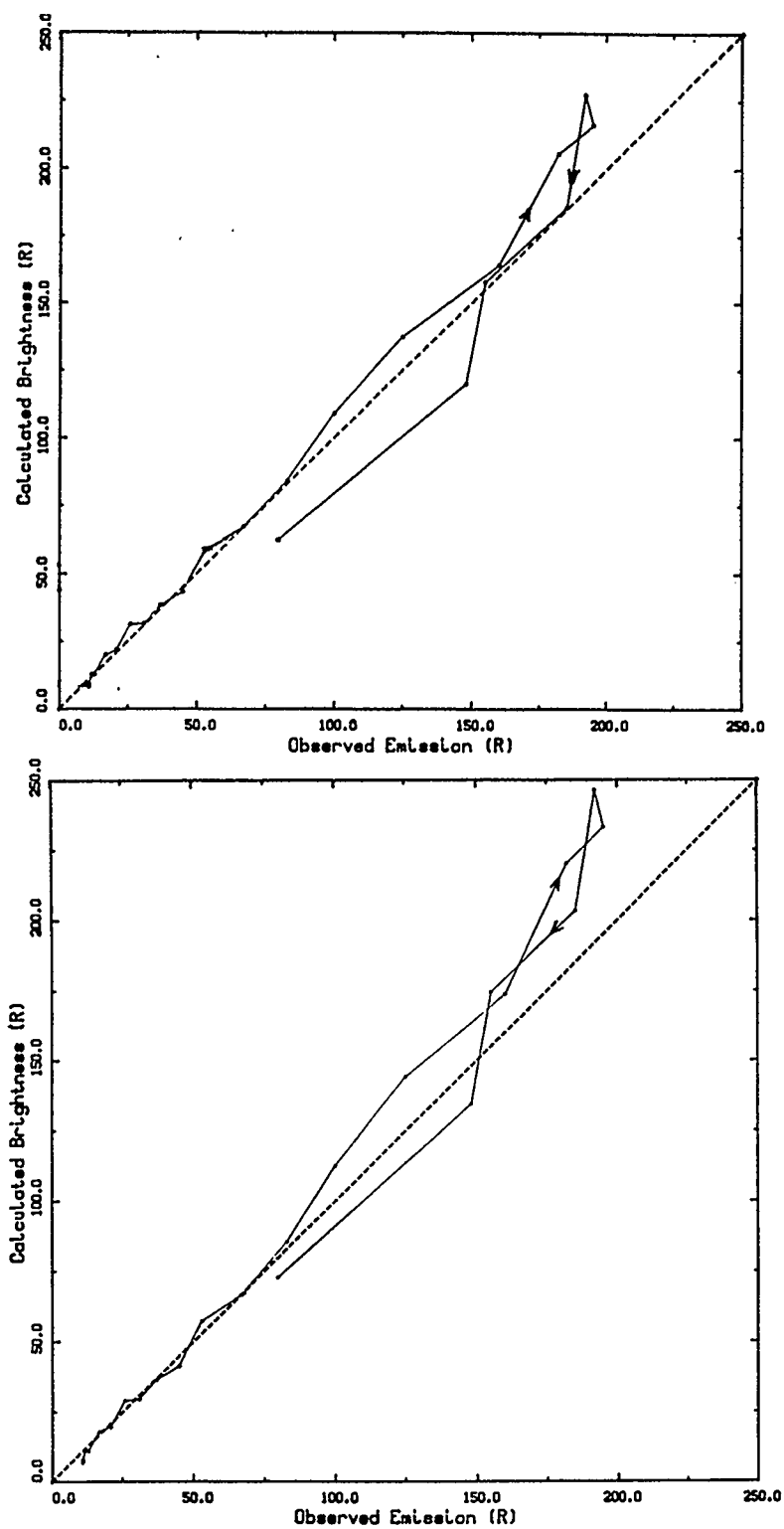
Figure 4.36 Calculated *vs.* Observed 6300 Å brightness, March 31/April 1, 1971.
Top: rate1. Bottom: rate2.
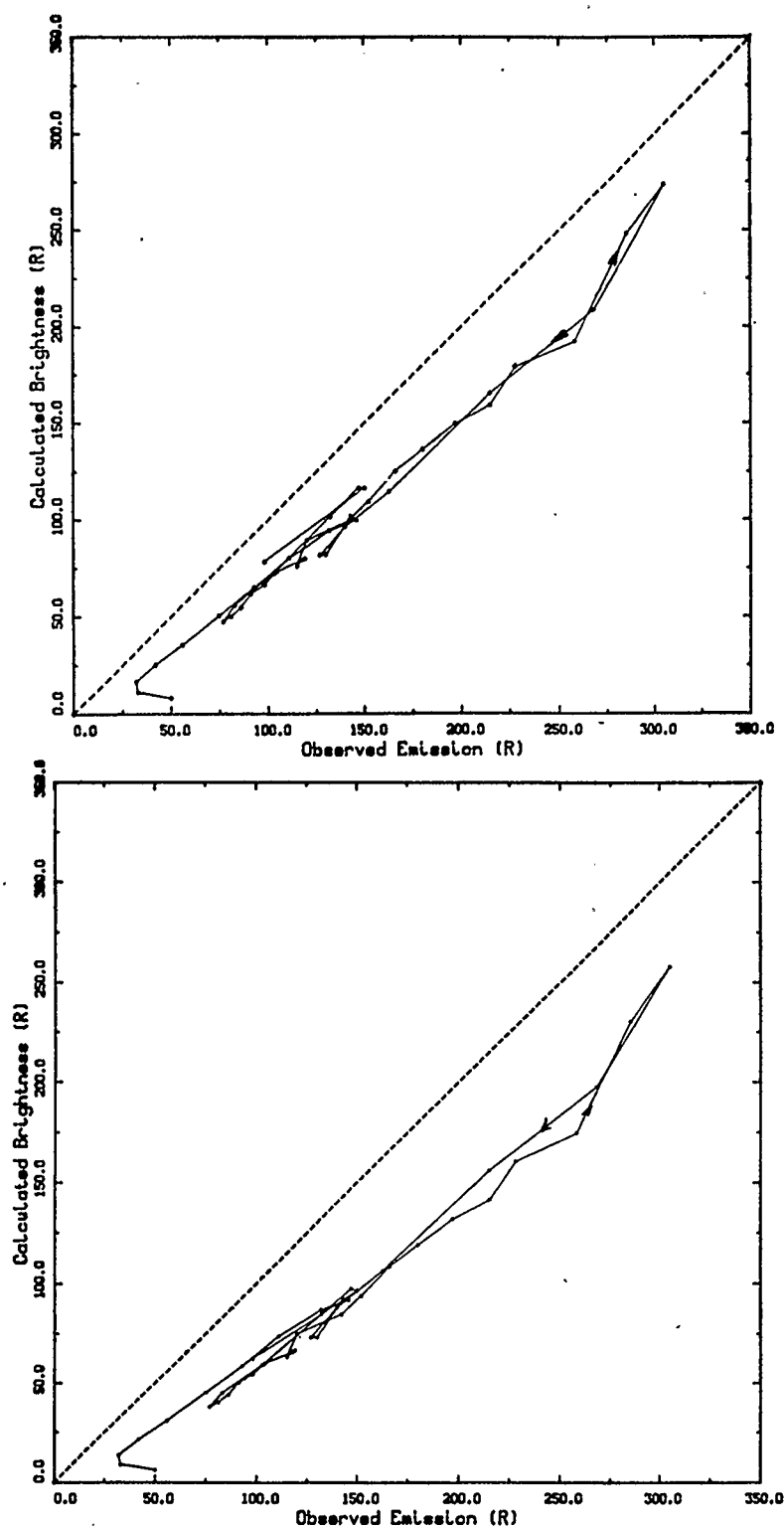
Figure 4.37 Calculated *vs*. Observed 6300 Å brightness, June 2/3, 1971.
Top: rate1. Bottom: rate2.

Figure 4.38 Calculated vs. Observed 6300 Å brightness, June 16/17, 1971.
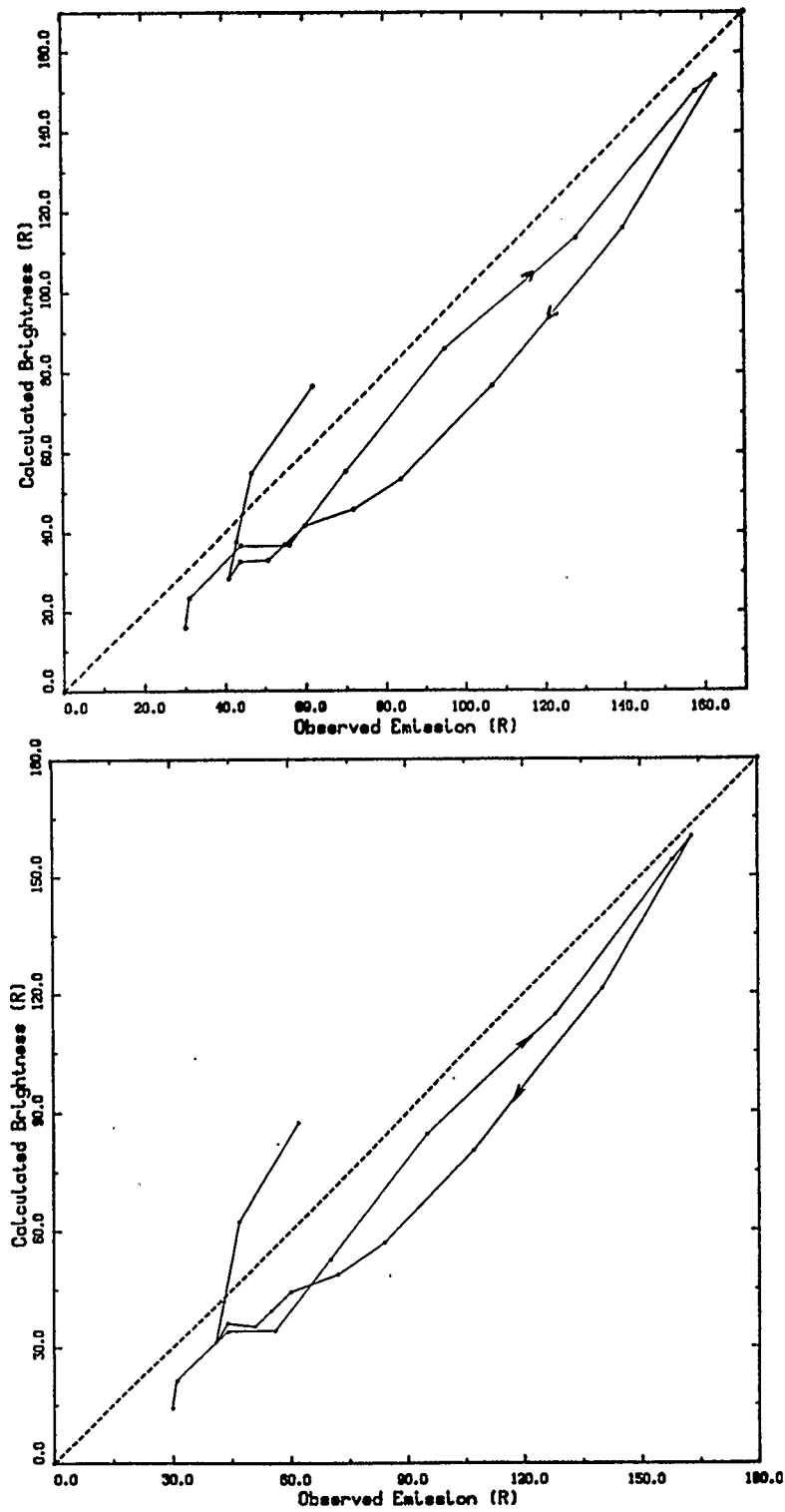Top: rate1. Bottom: rate2.

Figure 4.39 Calculated *vs.* Observed 6300 Å brightness, April 25/26, 1976.
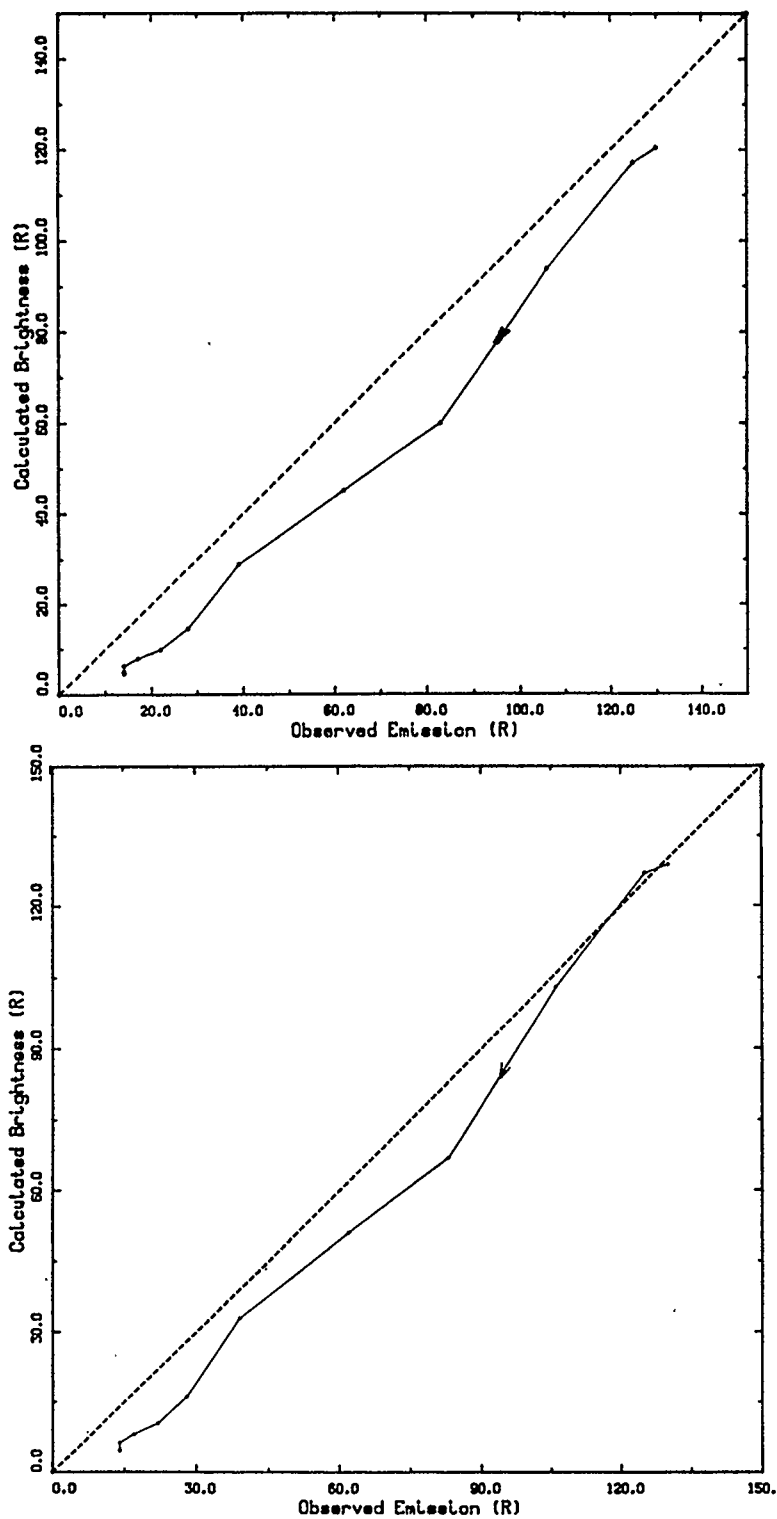Top: rate1. Bottom: rate2.

Figure 4.40 Calculated *vs.* Observed 6300 Å brightness, April 27/28, 1976.
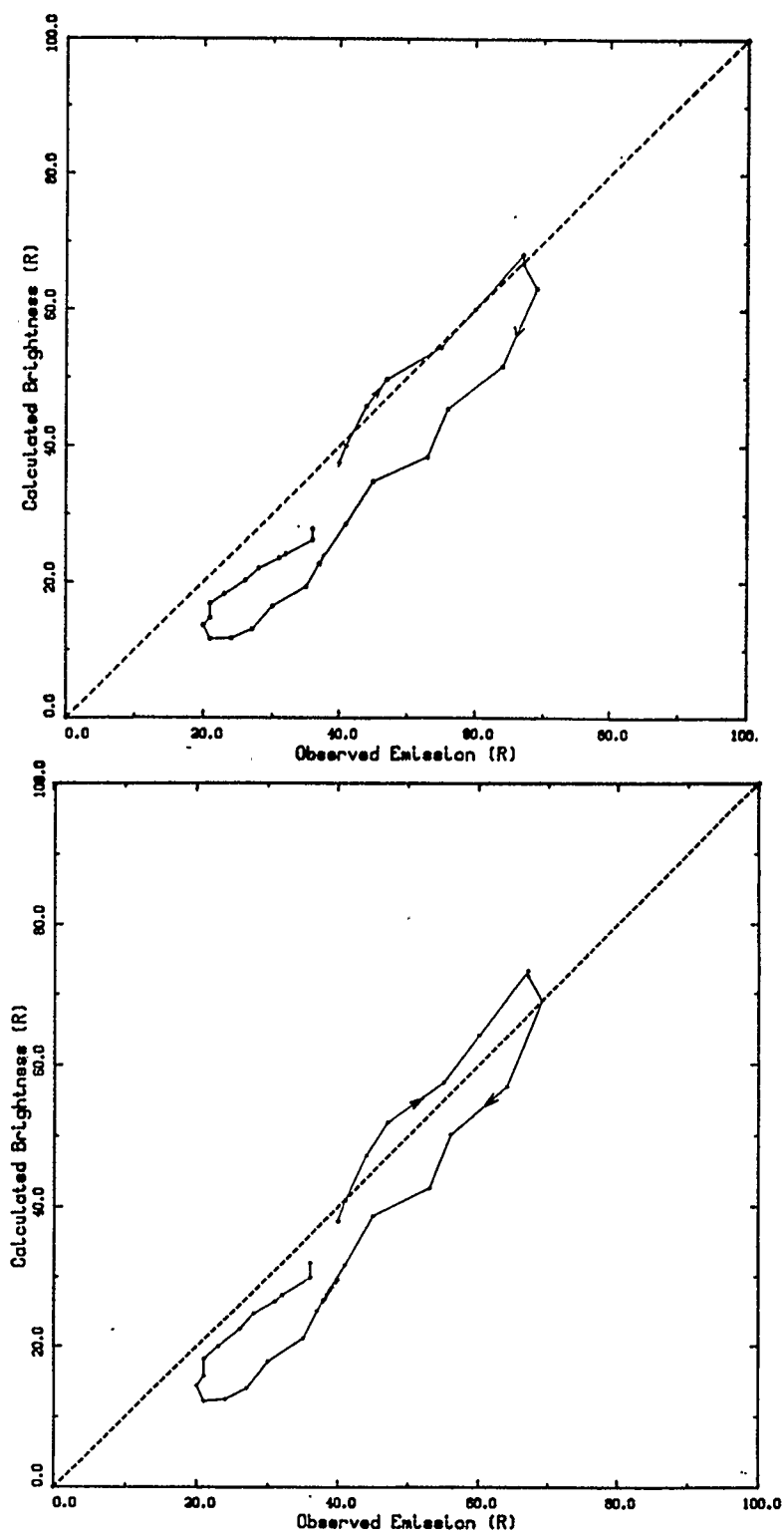Top: rate1. Bottom: rate2.

Figure 4.41 Calculated *vs.* Observed 6300 Å brightness, April 28/29, 1976.
Top: rate1. Bottom: rate2.

In 1971 and 1976, post-midnight enhancements of the red line were observed on 9 of the 10 nights studied. These are often seen to coincide with sizable increases in measured ion and electron temperatures which do not appear in the MSIS-83 model. (Note that 4.00 ut corresponds to midnight, local time [AST]). The plots of h_{max} vs. time clearly show the F layer descent responsible for the increase in red line intensity, typically beginning near local midnight, and frequently accompanied by an increase in peak electron density.

Possible evidence of conjugate photoelectrons may be seen in the 6300 Å brightness plots for March 4, 1971 and especially for Oct. 19, 1971 (fig. 4.33). The times for which the conjugate solar zenith angle is 102° are shown on these plots, and, particularly for Oct. 19, coincide with increases in observed brightnesses not reflected in the model.

The graphs of calculated vs. observed brightness found in figs. 4.34–4.41 illustrate results for the two different sets of rate coefficients used in the analysis. Results of a simple linear regression analysis of these graphs are shown in table 4.2. There appears to be no compelling reason to choose one set of rates over the other based on their ability to reproduce low latitude red line emissions using this equilibrium model.

The characteristic loop structure noted by Cogger et al. (1980) remains a significant feature of most of these graphs. The plotted points proceed in a clockwise sense in most cases, the notable exceptions being the two nights from June, 1971. In general, the clockwise loops appear slightly larger for the first rate set, while the second set (rate2) seems to enhance loops running counterclockwise.

Relevant quantities as functions of time are shown for the data acquired in 1985 in figs. 4.42–4.48. All I_{6300} calculations in this group used measured ion and electron temperatures as input to the MSIS-83 model atmosphere, as these were found to reproduce observed intensity fluctuations more faithfully than did MSIS-83 exospheric temperatures.

Table 4.2 Linear Regression Results on Calculated *vs.* Observed 6300 Å

Brightness, 1971 and 1976

Dates	rate1			rate2		
	slope	b/g (R)*	corr.	slope	b/g (R)*	corr.
1971						
Mar 3/4	1.45	10.	0.964	1.43	11	0.959
Mar 26/27	1.12	−3	0.981	1.13	−2	0.977
Mar 31/Apr 1	1.12	3	0.991	1.18	6	0.991
Jun 2/3	0.89	23	0.991	0.83	31	0.989
Jun 16/17	1.31	12	0.960	1.21	15	0.952
1976						
Apr 25/26	0.96	7	0.958	0.97	9	0.954
Apr 27/28	1.03	10	0.996	1.07	11	0.997
Apr 28/29	1.21	12	0.932	1.24	13	0.932

* b/g ("background") is the intercept on the observed brightness axis.

Table 4.3 Linear Regression Results for 1985

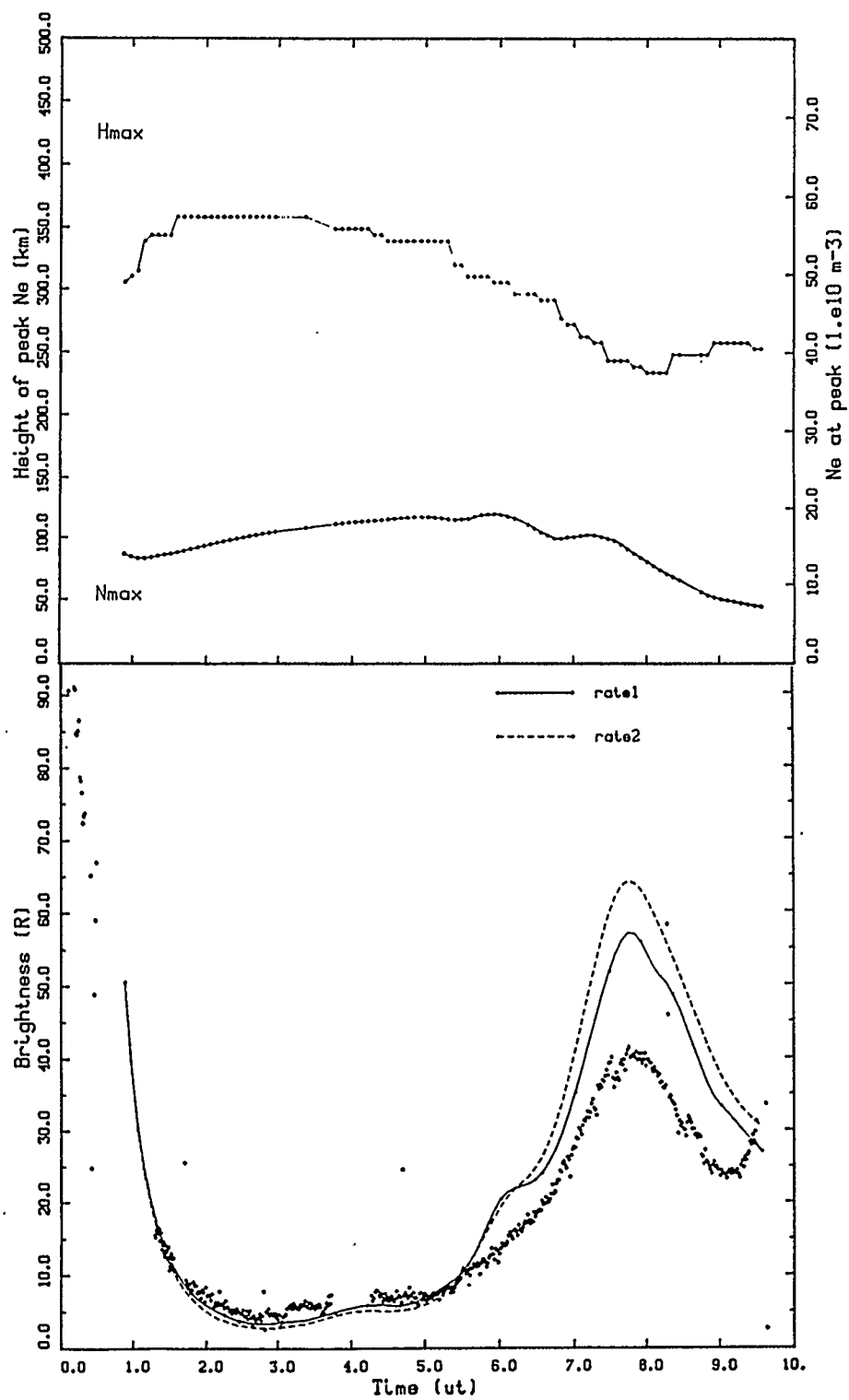| Dates (1985)	rate1			rate2		
	slope	b/g (R)*	corr.	slope	b/g (R)*	corr.
Mar 22/23	1.44	3	0.985	1.68	4	0.984
Mar 23/24	1.46	4	0.961	1.67	5	0.965
Mar 24/25	1.32	3	0.995	1.33	3	0.995
Apr 22/23	0.92	4	0.996	1.01	4	0.996
Apr 23/24	1.12	−1	0.976	1.22	0	0.977

Figure 4.42 F region parameters and 6300 Å brightness, March 22/23, 1985.
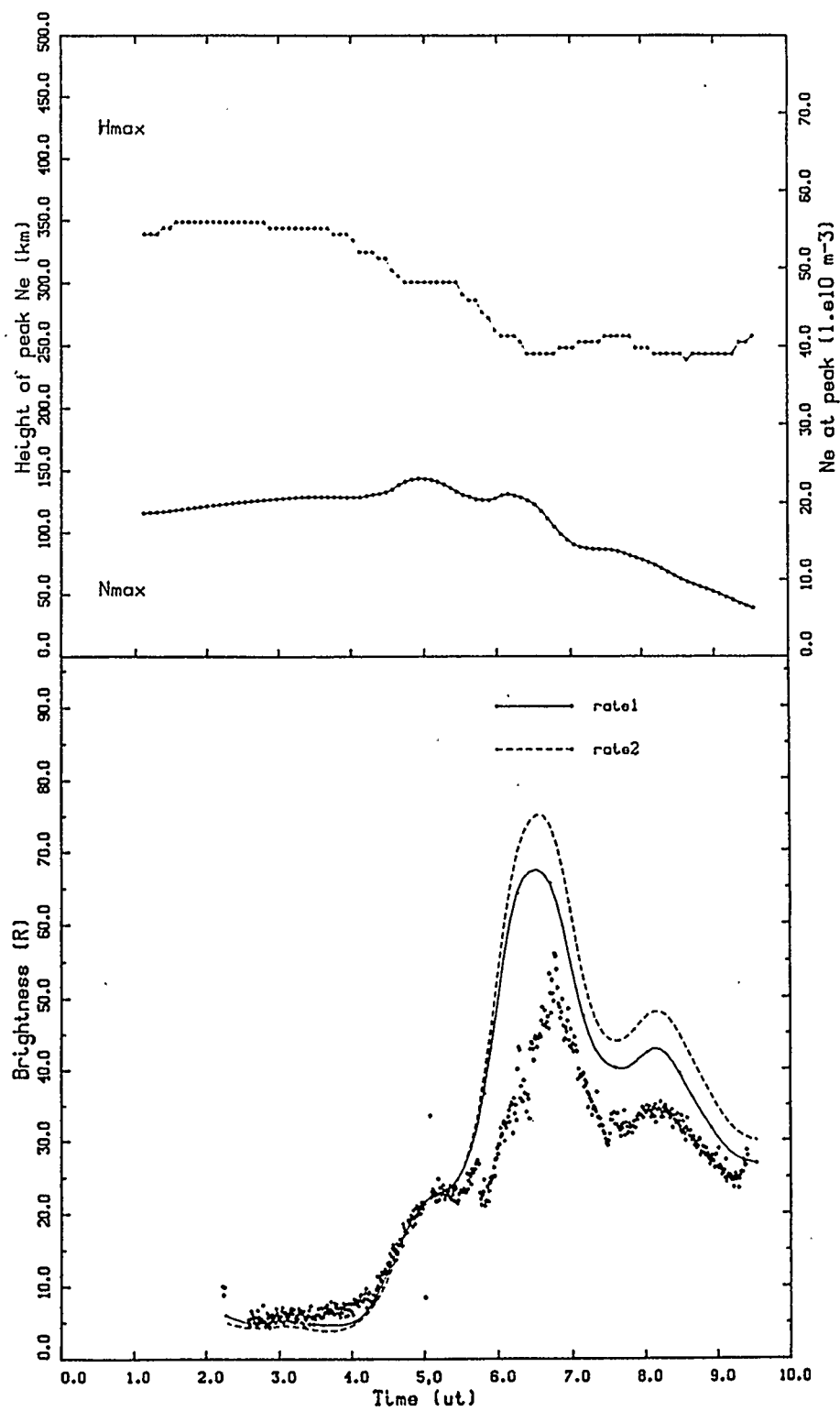
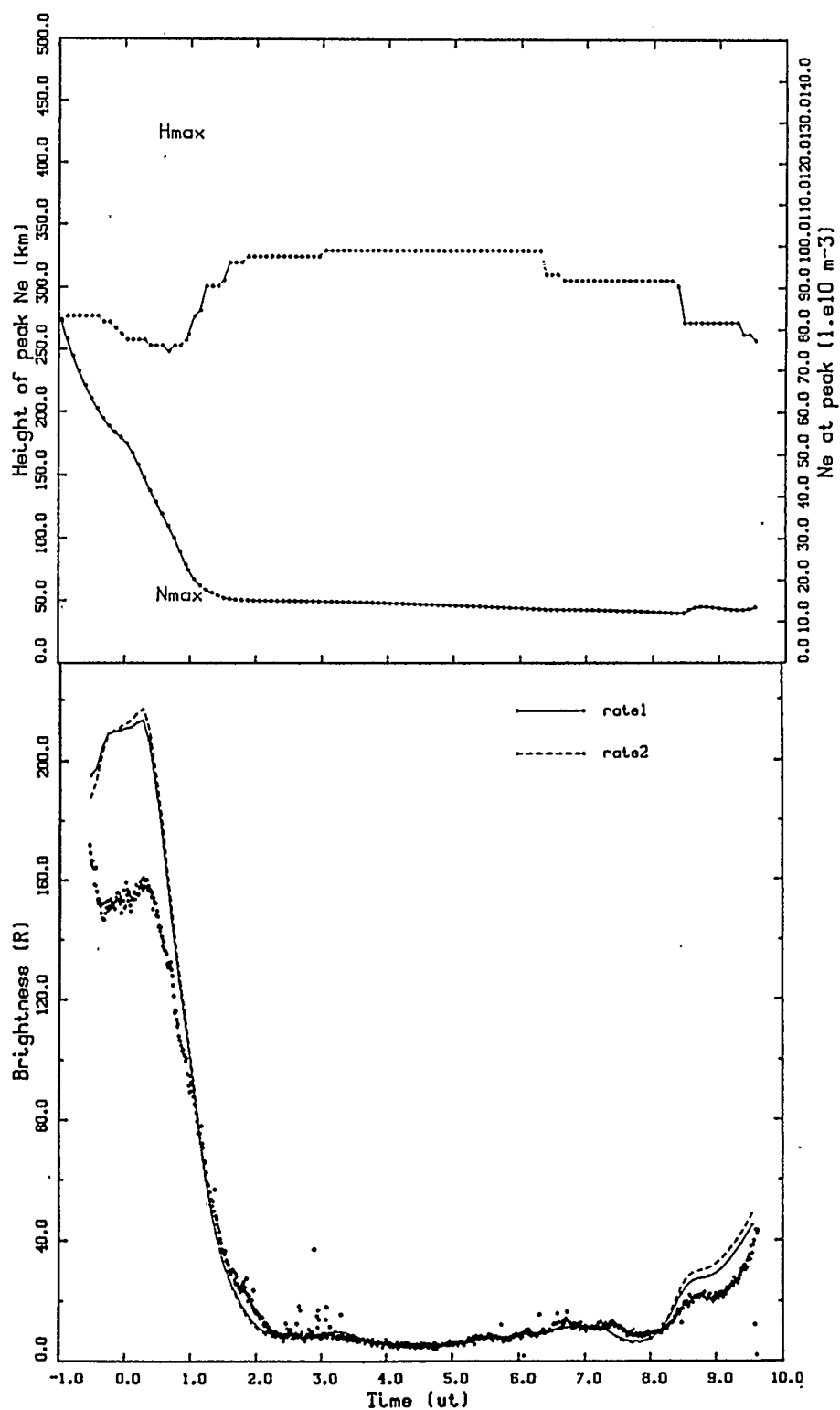Figure 4.43 F region parameters and 6300 Å brightness, March 23/24, 1985.

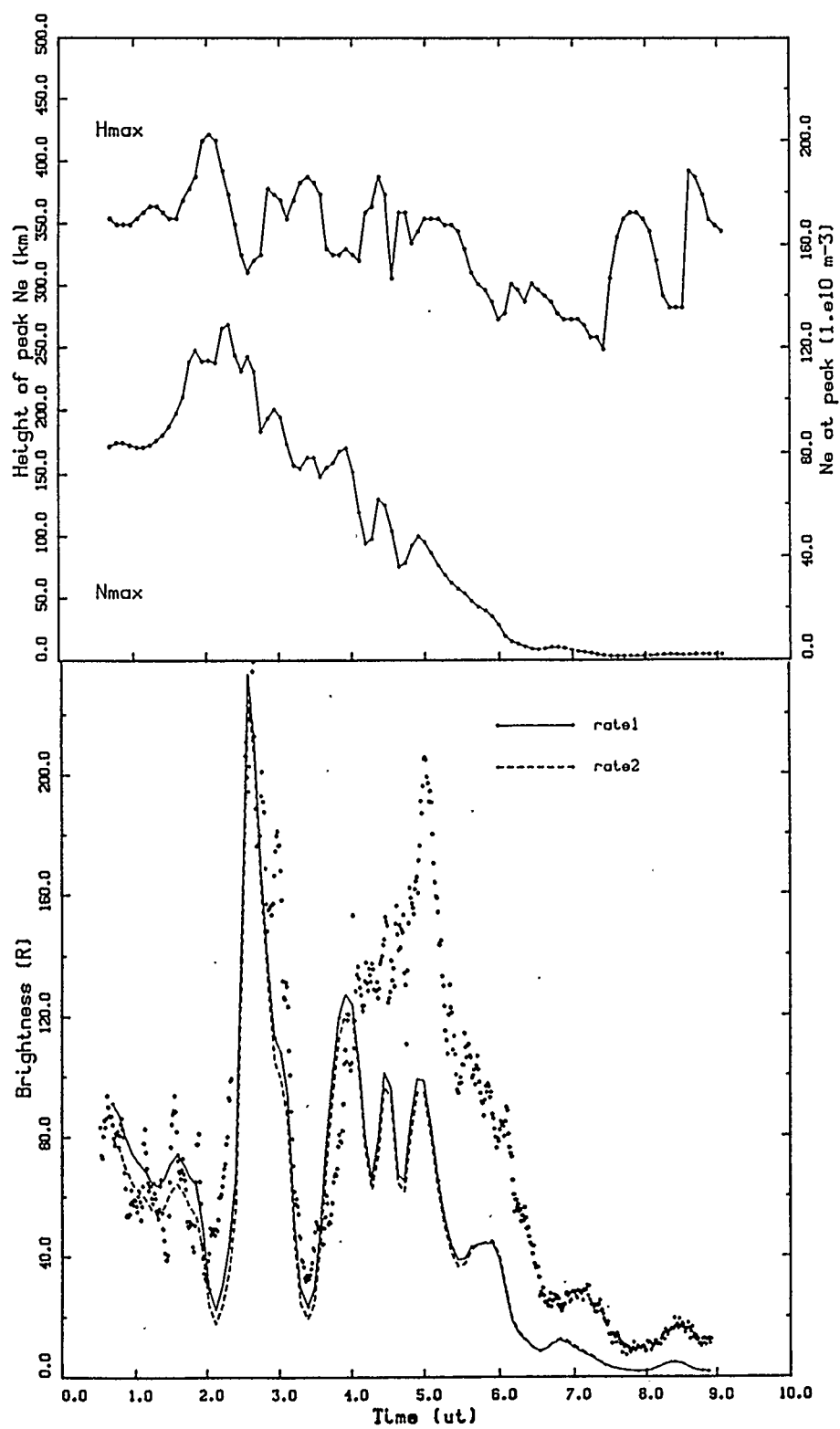Figure 4.44 F region parameters and 6300 Å brightness, March 24/25, 1985.

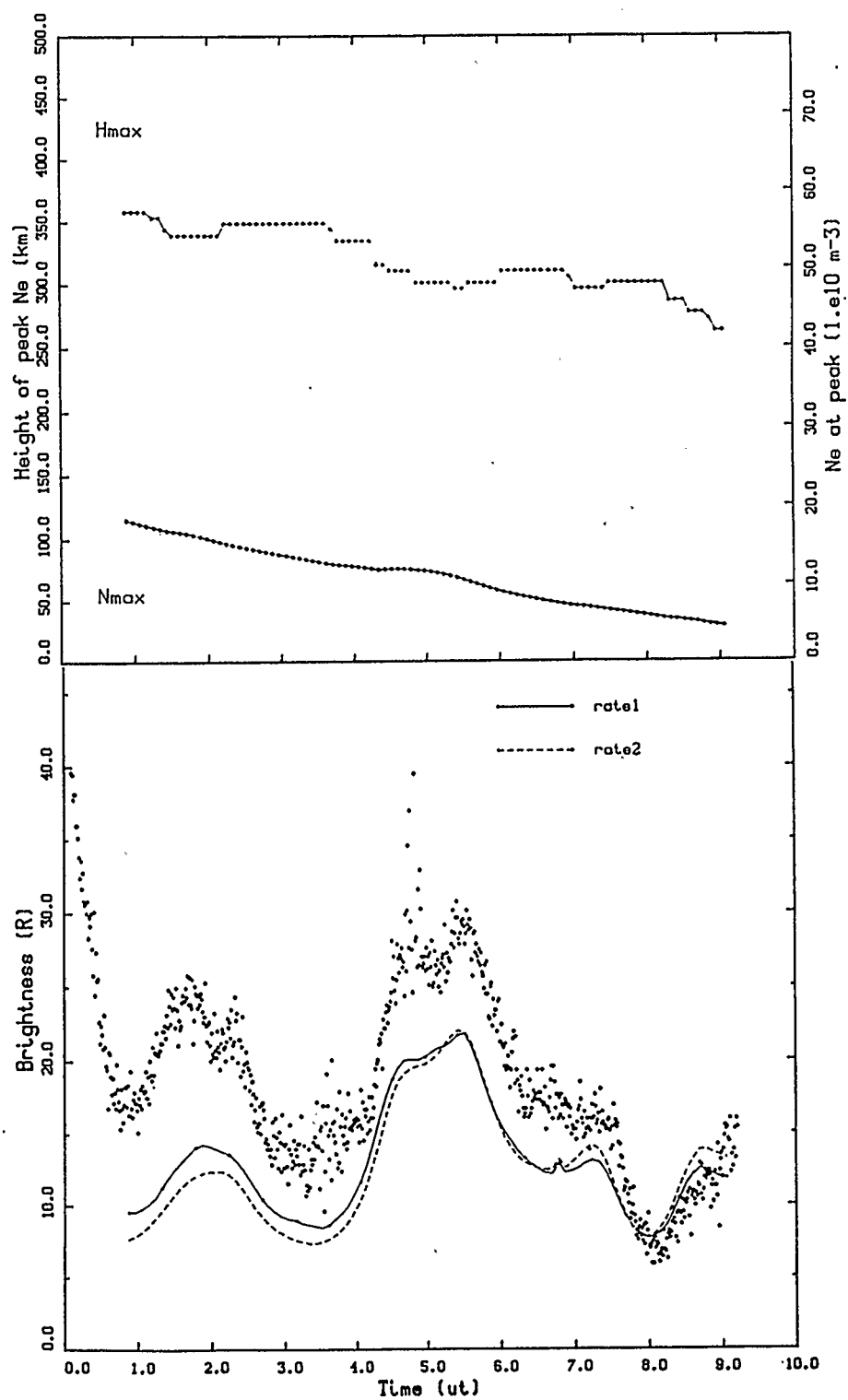Figure 4.45 F region parameters and 6300 Å brightness, April 20/21, 1985.

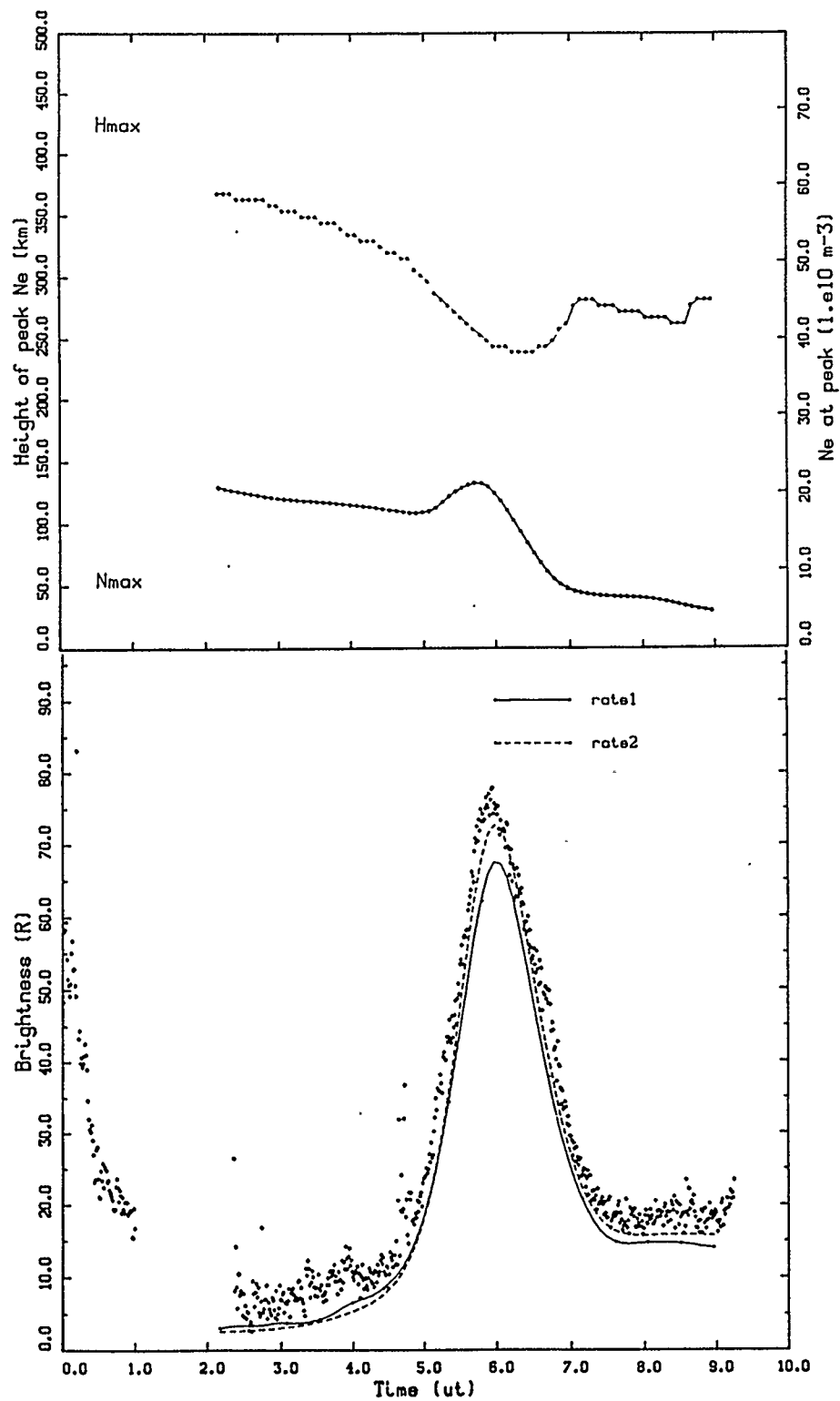Figure 4.46 F region parameters and 6300 Å brightness, April 21/22, 1985.

Figure 4.47 F region parameters and 6300 Å brightness, April 22/23, 1985.
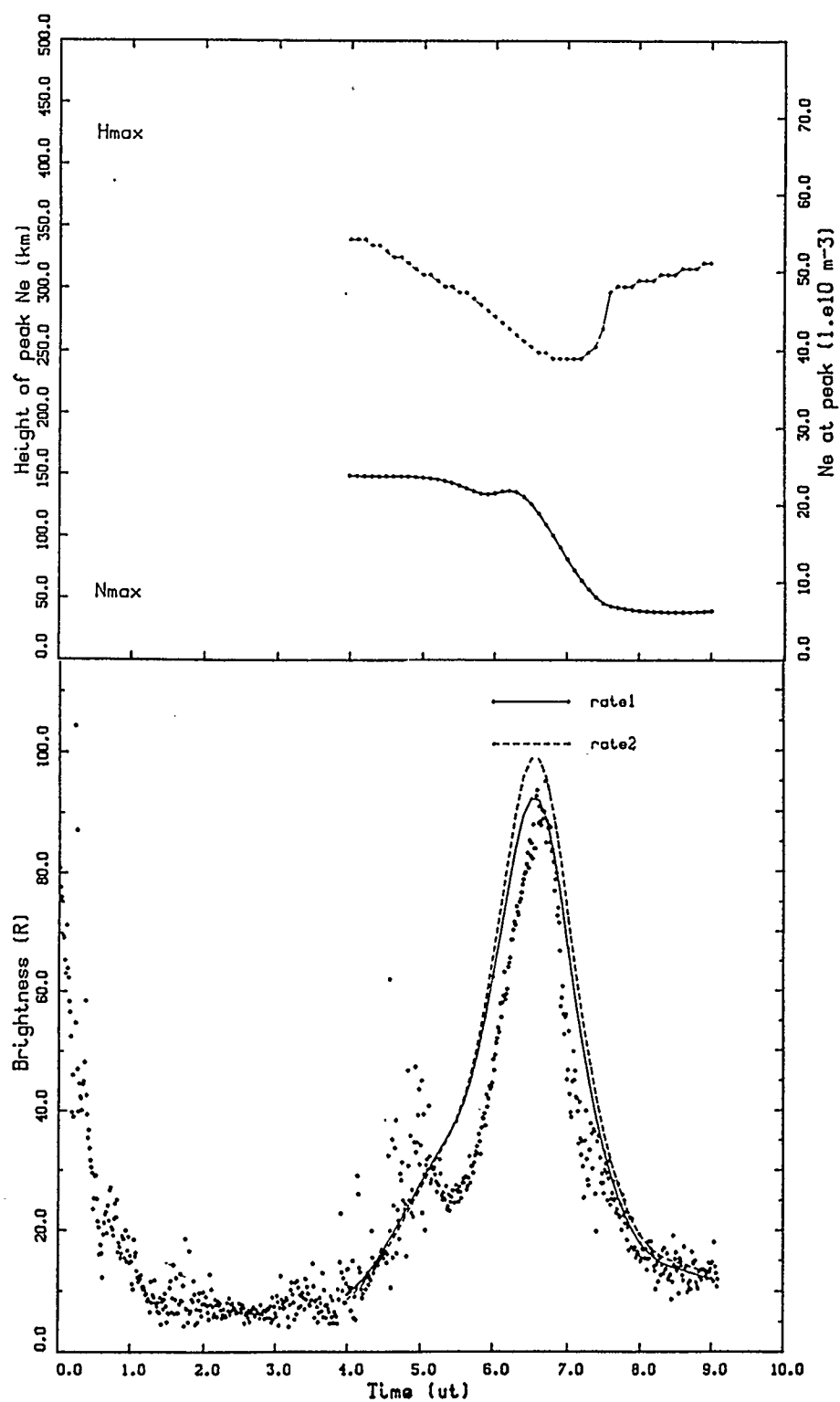
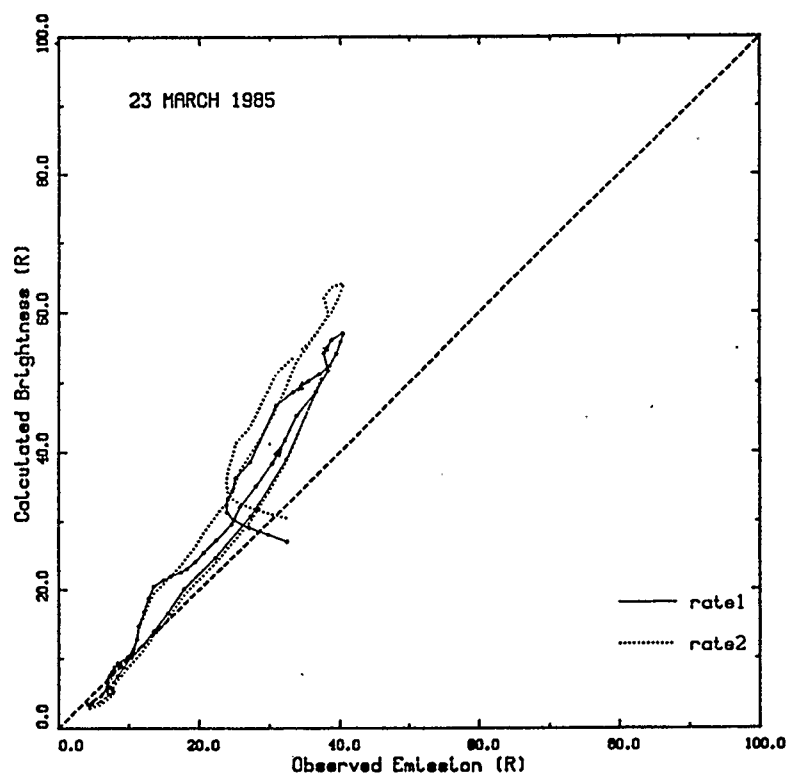Figure 4.48 F region parameters and 6300 Å brightness, April 23/24, 1985.

Figure 4.49 Calculated *vs.* Observed 6300 Å brightness, March 22/23, 1985.
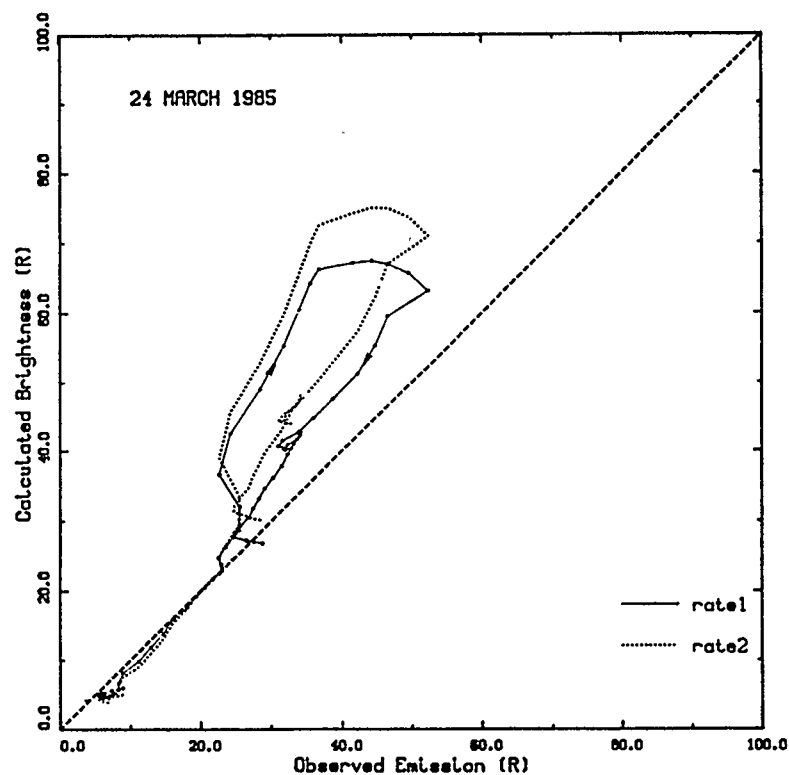

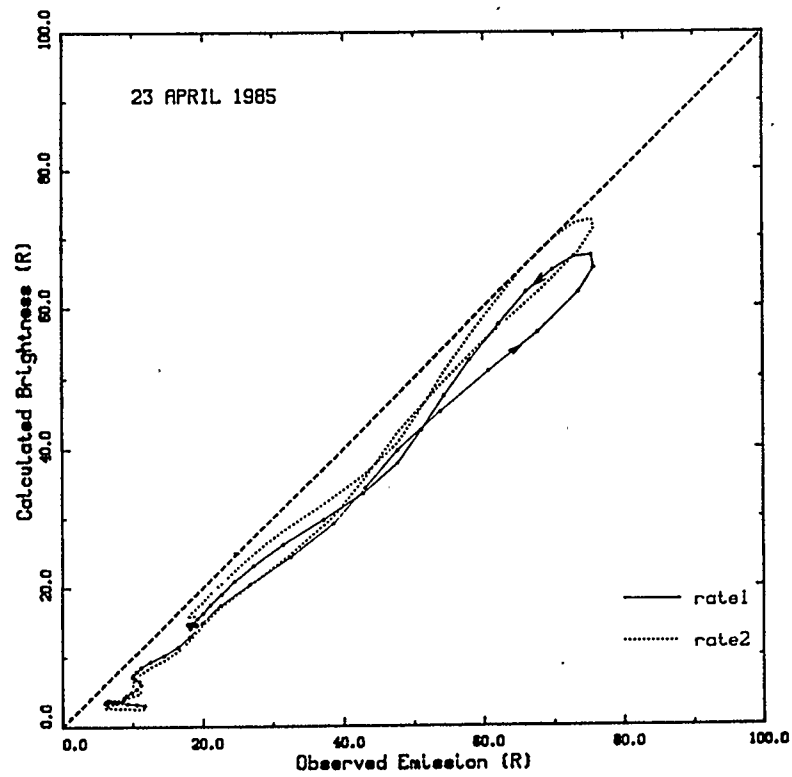Figure 4.50 Calculated *vs.* Observed 6300 Å brightness, March 23/24, 1985.

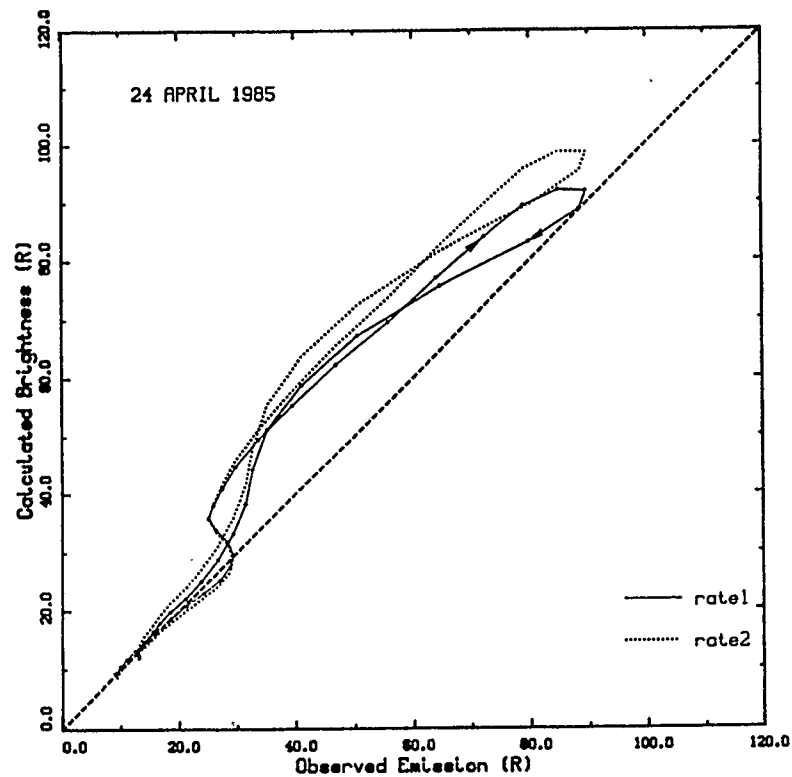**Figure 4.51** Calculated vs. Observed 6300 Å brightness, April 22/23, 1985.

Figure 4.52 Calculated vs. Observed 6300 Å brightness, April 23/24, 1985.

Model results using both sets of rate coefficients are illustrated. As with the earlier data, the general trends of the red line intensity are quite well followed for both rate sets, but our original calculations (based on rate1) appear generally somewhat closer to the actual values.

The behaviour of the OI red line varied considerably from one night to the next, reflecting the complex and dynamic behaviour of the upper atmosphere. This is particularly evident with the greater temporal resolution of this more recent data. Of the three nights in March, 1985, two show post-midnight increases of quite different character, while the third was remarkably quiet. For all three, the calculated brightness fluctuations were significantly greater than those observed, but relatively low electron densities on these nights made measurements of F-region parameters difficult, and hence made a good fit harder to achieve. In fact, on Mar 22/23, 1985, quite a nice fit was obtained before the electron densities were recalibrated.

Plots of calculated *vs.* observed brightness for Mar 22/23 and Mar 23/24, 1985, may be found in figs. 4.49–4.50, and corresponding linear regression results in table 4.3. These graphs are somewhat surprising, in that while fig. 4.50 shows a large, clockwise hysteresis loop associated with the triangular structure seen in fig. 4.43, the post-midnight sense of 4.49 is mainly counterclockwise, with a small clockwise loop at the top. The greater sensitivity of rate1 to thermospheric and ionospheric densities is demonstrated by the bulge in calculated I_{6300} at about 0600 ut of Mar 22/23, which leads to the larger counterclockwise loop in fig. 4.49, as compared with that of rate2.

The four nights of observations taken in April, 1985, captured a remarkable variety of ionospheric activity, as illustrated by the red line intensity variations. The effects of a major geomagnetic disturbance and its aftermath are clearly evident in figs. 4.45 and 4.46, followed by a return to quiet conditions with large post-midnight red line enhancements in

figs. 4.47 and 4.48. The results of Apr 20/21 and Apr 21/22 will be examined more closely in section 4.9.

Apr 22/23 and Apr 23/24, 1985, display classic features of post-midnight ionospheric behaviour: a post-midnight temperature bulge, rapid descent of the F-layer peak with a corresponding increase in peak electron density, and the resulting rapid increase in red line production. From these figures, and the linear regression results of table 4.3, it is clear that the gross size and shape of the peaks are quite successfully reproduced by the equilibrium model. Figures 4.51 and 4.52 illustrate differences in some finer features, including small wave-like structures and significant hysteresis loops. A direct comparison of the two nights is not really possible, since the radar data were obtained in somewhat different fashions (sections 3.4 and 4.1.2), but it may be worth noting that while the brightness is increasing the slopes of both are close to unity, but the two graphs show quite different behaviour on the downslopes. A counterclockwise loop is produced in fig. 4.51, and a clockwise loop in fig. 4.52.

Brightness calculations at 6300 Å were also performed using double the original estimate of atomic nitrogen density. In all cases, the results were affected by less than 10%, thereby verifying the relative insensitivity of this model to atomic nitrogen.

To sum up, this model seems to have been more successful in reproducing red line intensity data from the 1970s than that from 1985, but the fits are all quite reasonable except for the periods following intense geomagnetic activity. It was also found that, apart from such periods, there was very little difference in results whether or not measured ion and electron temperatures were used to estimate exospheric temperatures as input to the MSIS-83 model atmosphere. Most of the nights studied showed the classic post-midnight red line enhancement as a direct result of the lowering and compression of the F layer. One

puzzling result has emerged, however. Although for the spring months of 1971 and 1976, the red line hysteresis loops tended to proceed in a clockwise direction, this no longer appeared generally true in 1985. The problem of the loop structure will be addressed further in section 4.8.

4.6 Comparison of Reaction Rate Coefficients

As seen in table 4.2, there is little difference in the slopes of calculated *vs.* observed brightness for the two different sets of rate coefficients rate1 and rate2. In comparison with the results of Cogger *et al.* (1980), these slopes are a factor of 2 to 3 smaller (mean factor about 2.4) and most slopes are consistent with unity within observational uncertainty.

The relative temperature dependence of the rates is shown in fig. 4.20; some representative rate values are given in table 4.4, with the corresponding values from Cogger *et al.* (1980) for comparison. According to the T_n profiles shown in fig. 4.19, only variations over the range 600–1100 K need be considered in the nighttime F region. In addition to the coefficients listed in table 4.4, rate1 also includes quenching by atomic oxygen, which becomes quite significant at higher altitudes. Quenching by electrons is included in rate2, but this is generally negligible (Link and Cogger, 1988). The most significant differences from the Cogger *et al.* (1980) rates are the reduction of A_{6300} and α_3 (N_2 quenching) in both rate1 and rate2, the addition of atomic oxygen quenching to rate1, and the reduction of k_1 by 25 - 35% in rate2. This last change is consistent with the suggestion of Cogger *et al.* (1980) that k_1 had likely been overestimated.

Table 4.4 Values of Rate Coefficients at various Temperatures

Coefficient	Cogger et al. (1980)			rate1			rate2		
T (K) =	300	700	1000	300	700	1000	300	700	1000
α_1 (10^{-7} cm³/s)	1.6	1.0	0.83	1.85	1.16	0.95	1.95	1.08	0.84
β_{1_D}		1.3			1.2			1.1	
k_1 (10^{-11} cm³/s)	2.15	1.54	1.25	2.15	1.54	1.25	2.05	1.13	0.83
k_2 (10^{-12} cm³/s)	1.03	0.62	0.52	1.03	0.62	0.52	1.20	0.60	0.46
α_2 (10^{-7} cm³/s)	4.2	2.0	1.5	4.3	1.8	1.3	4.0	1.9	1.4
α_3 (10^{-11} cm³/s)		3.0			2.3		2.9	2.3	2.2
α_4 (10^{-11} cm³/s)	(included in α_3)				4.0		3.6	3.2	3.1
A_{6300}		.0069			.00515			.00563	

The main difference between the two new rate sets is that production and quenching rates of O(^{1}D) atoms are substantially higher for rate1 than for rate2, as is clearly shown in the emission profiles illustrated in figs. 4.21–4.24. The effect of this is to render calculation of 6300 Å brightness using rate1 much more sensitive to the densities of relevant species than they would be using rate2, and in particular more responsive to perturbations in the neutral atmosphere.

Link and Cogger (1988) discussed the relative merits of the rate1 and rate2 values of some of the coefficients listed in table 4.4. In particular, they felt that the expression used for k_1 in rate2 (due to Chen et al., 1978) may be more appropriate for ionospheric conditions than the expression due to St. Maurice and Torr (1978) used in rate1. This is due to the different methods of obtaining temperature variations used by the two authors. Link and

Cogger (1988) noted that, with the reduced values of k_1 proposed by Chen *et al.*, introduction of quenching by atomic oxygen is not necessary to obtain reasonable agreement between observed and calculated brightnesses. In contrast, however, Yee *et al.* (1985) concluded that quenching by atomic oxygen should be considered in modelling the 6300 Å airglow.

Clearly, the simple photochemical model applied to the present data set is not sufficient to allow a meaningful decision to be made on the matter of reduced k_1 *vs.* O quenching. Further calculations involving the oxygen green line at 5577 Å and dynamic effects may shed some light on this matter.

4.7 Comparison of Red and Green Line Emissions

The photometers at Arecibo were used to measure the total surface brightness of the oxygen green line at 5577 Å. Under normal conditions, most of this emission originates in the E region, for which at present there seems to be no adequate model. Nonetheless, an attempt was made to extricate the F-region contribution to the total, as follows.

It is assumed that quenching is negligible for the F-region green line; therefore its brightness should be compared with that of the red line with quenching effects removed, called "red line production" (P_{6300}). It is also assumed that, under quiet conditions, there is negligible correlation of E- and F-region green line brightness.

A substantial uncertainty in the calculation of I_{5577} lies in the value for β_{1S}, the number of $O(^1S)$ atoms produced per dissociative recombination of O_2^+ (see section 4.3). This value is thought to depend on the vibrational distribution of the O_2^+ molecules, with $O(^1S)$ resulting chiefly from the $v = 1,2$ levels (Guberman, 1987). Early estimates of β_{1S} range

from 0.1 (Zipf, 1970) to 0.09–0.23 (Abreu *et al.*, 1983) in the F region. Much lower values (.01–.06) have recently been obtained by Zipf (1988), and it was hoped that the following analysis would help to establish a reasonable range of β_{1S} values.

F-region 5577 Å column integrated intensities were calculated for a range of β_{1S} values. These were then subtracted from the total observed green line intensities, the result presumed to represent E-region emissions. Then the calculated effect of quenching was removed from observed red line intensities, so the first term in 4.7.4 represents photometer data, the second a calculation based on radar data.

$$I_{5577} \text{ (F region)} = \int_{\text{F region}} \eta_{5577} \, dh = \int_{\text{F region}} \frac{A_{5577}}{A_{1S}} \beta_{1S} k_1 [O_2][e] \, BF \, dh$$

$$= P_{5577} \qquad\qquad (4.7.1)$$

$$p(6300) = \beta_{1D} k_1 [O_2][e] \frac{A_{6300}}{A_{1D}} \frac{B}{F} = \eta_{6300} \frac{A_{6300}}{A_{1D}} \frac{1}{D} \qquad (4.7.2)$$

$$\text{where} \quad \frac{1}{D} = \frac{A_{1D} + \alpha_3[N_2] + \alpha_4[O_2] + \alpha_5[O]}{A_{6300}} = \frac{A_{1D} + Q}{A_{6300}}$$

$$\frac{A_{6300}}{A_{1D}} \cdot \frac{1}{D} = 1 + \frac{Q}{A_{1D}} \implies p(6300) = \eta_{6300}\left(1 + \frac{Q}{A_{1D}}\right) \qquad (4.7.3)$$

$$P_{6300} = \int p(6300) \, dh = \int \eta_{6300}\left(1 + \frac{Q}{A_{1D}}\right) dh$$

$$= I_{6300} + \int \eta_{6300} \frac{Q}{A_{1D}} \, dh \qquad (4.7.4)$$

The resulting calculated red line production was correlated with estimated E-region 5577 Å intensities for various β_{1S}. The value of β_{1S} which resulted in zero correlation was then taken as a reasonable estimate of β_{1S}. It was anticipated that the best results would be obtained for the nights when a large post-midnight enhancement was observed, particularly if the photochemical model reproduced the observations satisfactorily.

For several of the 1971 nights, photometric observations of 5577 Å intensities were retrieved from old files, and are shown together with corresponding 6300 Å intensities in figures 4.53 and 4.54. Corresponding plots for 1985 are found in figures 4.9–4.15. Figure 4.55 shows examples of the observed green line intensities, and the calculated E-region contributions for various values of β_{1S}. Finally, the data were divided into three types: post-twilight decay and post-midnight peaks for quiet nights, and major peaks from nights of high geomagnetic activity. Plots of the correlation between F-region red line production and estimated E-region green line intensity as a function of β_{1S} may be found in figures 4.56 and 4.57. The results are summarized in table 4.5, along with some ionospheric parameters for the relevant times.

There are several drawbacks to this approach. Results rely heavily on both the atmospheric model, used to obtain neutral densities, and radar measurements of ionospheric parameters, especially electron densities. Well-behaved height profiles of all parameters are assumed, which does not allow for wave structure in temperatures and neutral densities. Calculations using doubled atomic nitrogen densities in most cases made little difference, but up to a 25% change in I_{5577} was found in some post-twilight calculations. The most reliable results should therefore be obtained for large post-midnight peaks on quiet nights, for which a good fit between calculated and observed 6300 Å intensities was achieved. Unfortunately, 5577 Å intensities were not available for many of the nights to which these conditions would apply.
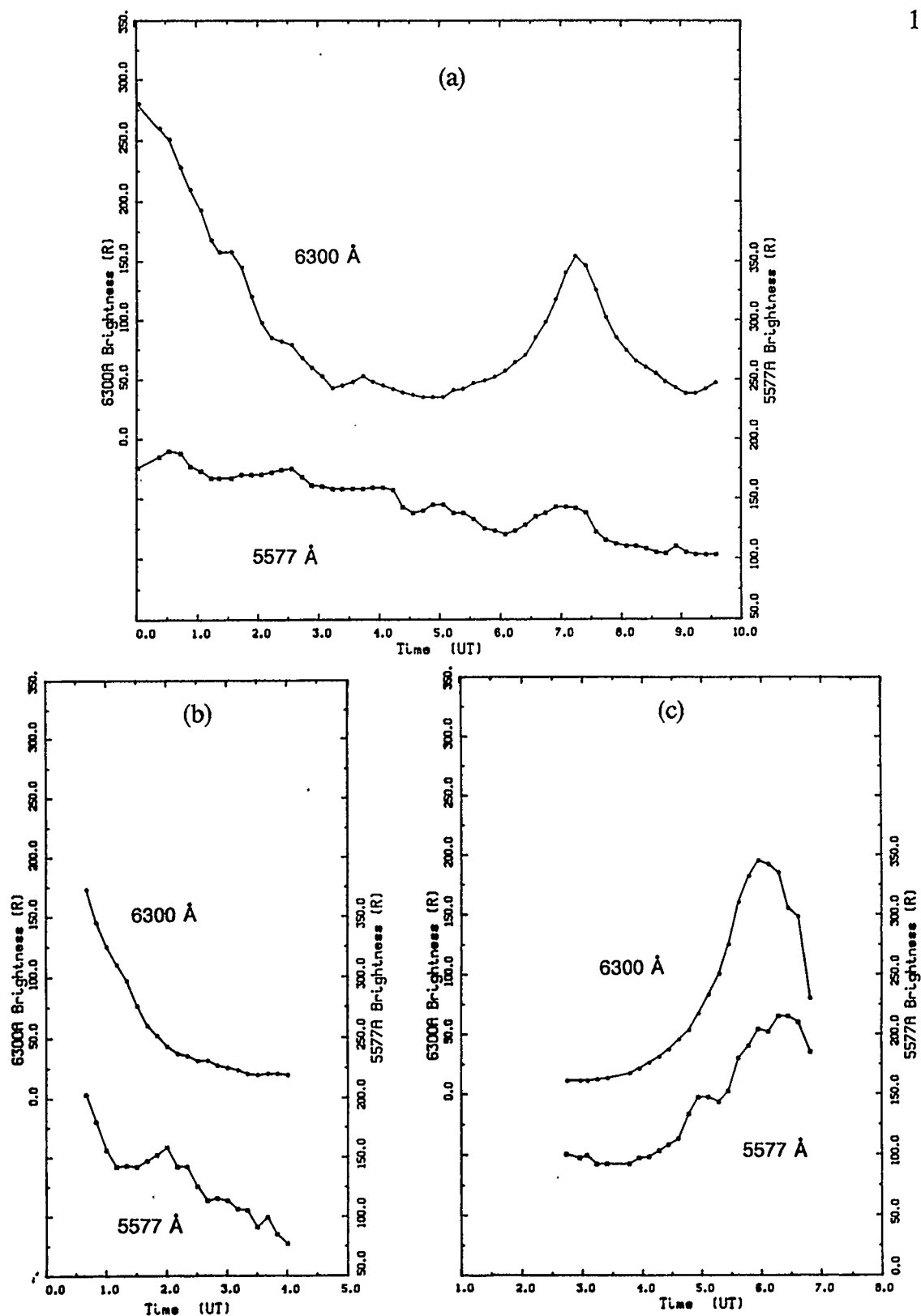
Figure 4.53 1971 Photometer data from Arecibo. (a) March 3/4, 1971
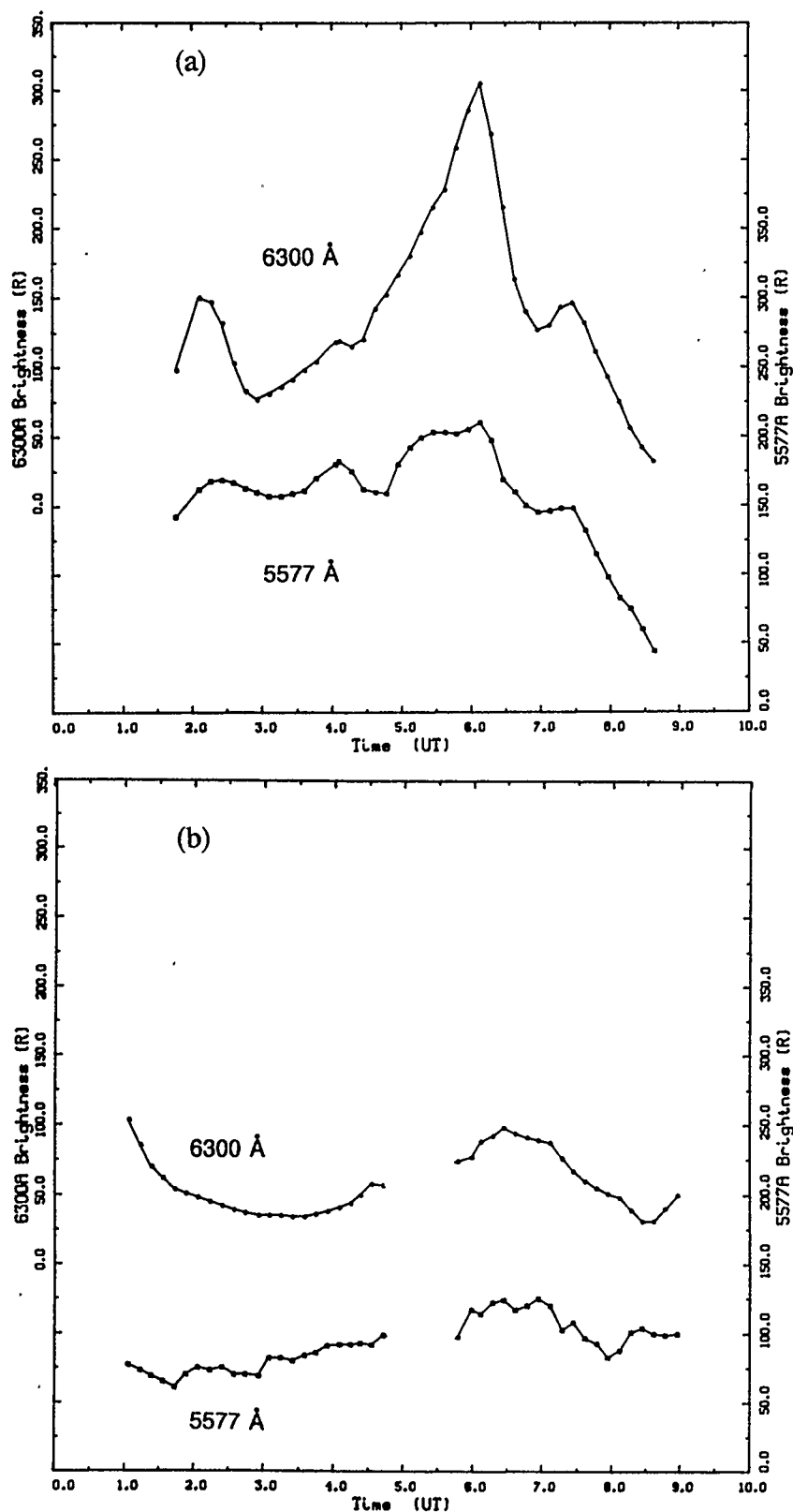(b) March 26/27, 1971 (c) March 31/April 1, 1971

Figure 4.54 1971 Photometer data from Arecibo, continued.
(a) June 2/3, 1971 (b) June 16/17, 1971
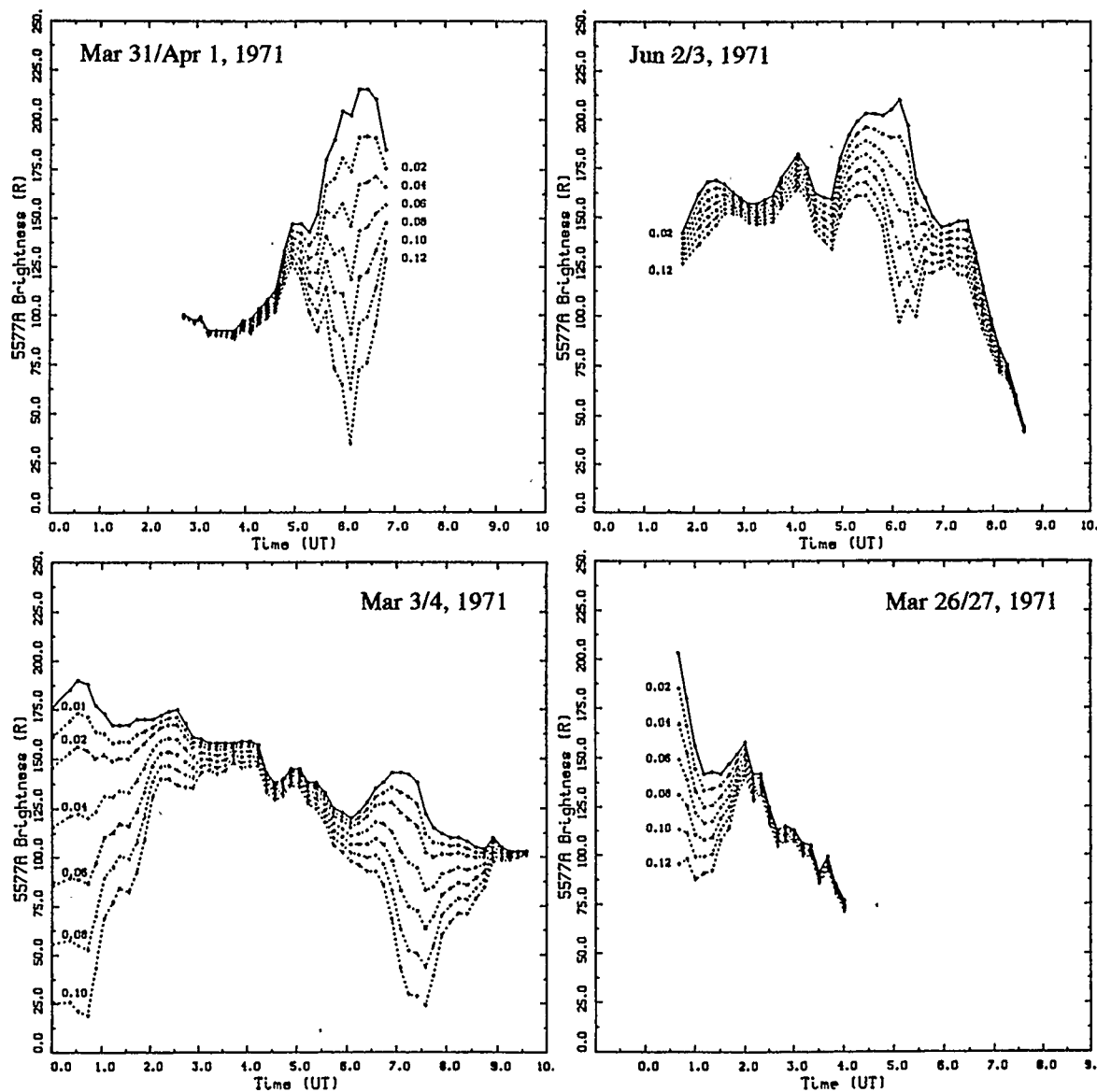
Figure 4.55 5577 Å zenith intensities at Arecibo: observed total and estimated E-region (total minus F-region contribution). Solid curves show the total intensity. Dashed curves give results of subtracting F-region contribution using various values of β_{1S}. β_{1S} may be taken to be zero at any solid curve, increasing in steps of 0.02 as one reads down a given set of dashed plots (a result for β_{1S} = 0.01 is included for Mar 3/4, 1971, only).

Figure 4.56 Correlation coefficient of F region O(^{1}D) production *vs.* E region
5577 Å brightness (observed total minus estimated F region), calculated
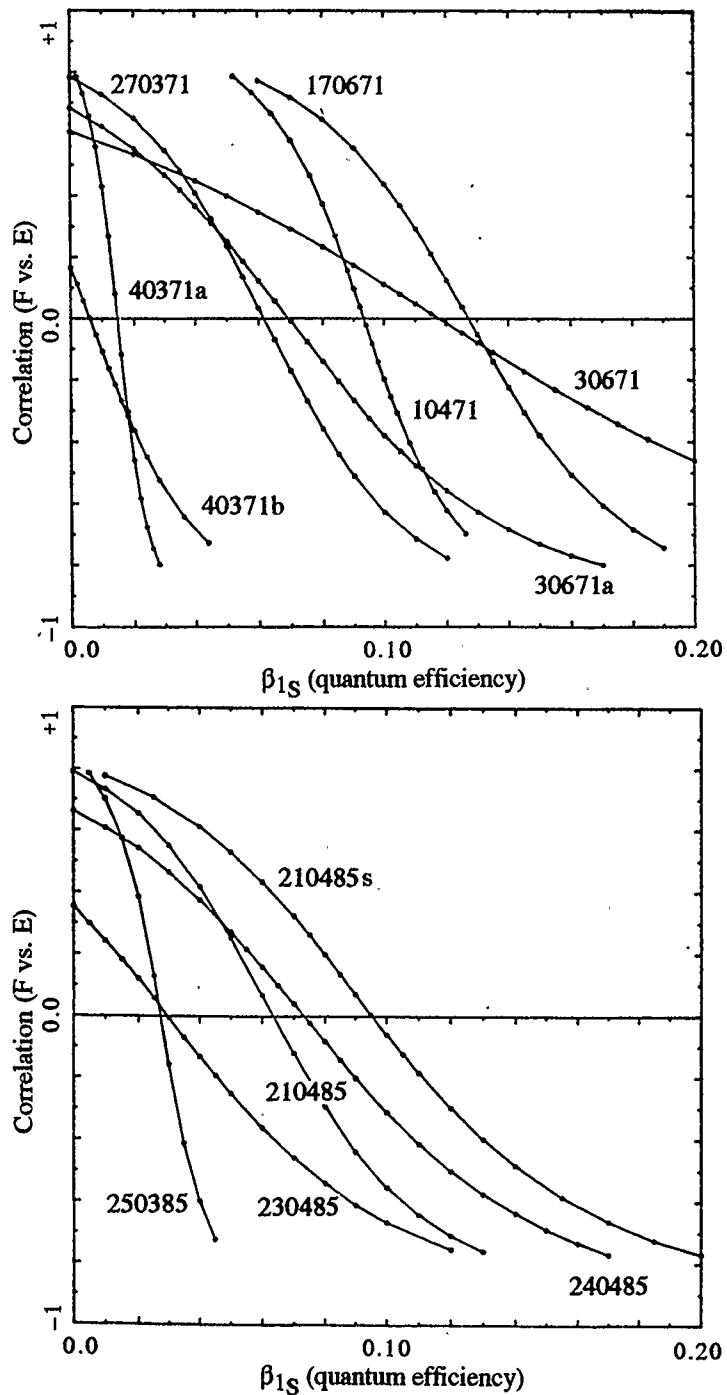using rate1 reaction rates. (30671 - whole night; 30671a - main peak;
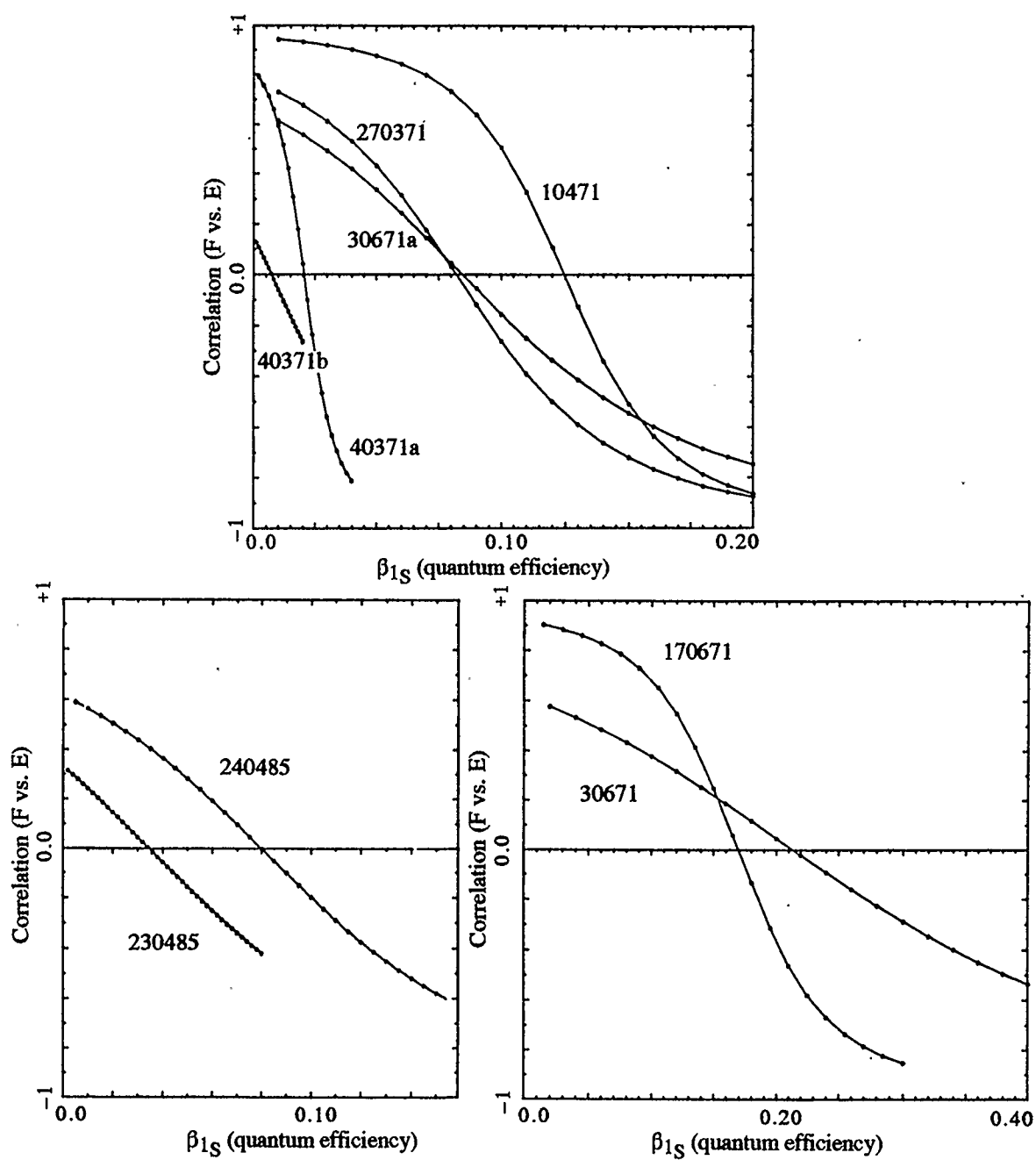210485s calculated for n_e x 0.7.)

Figure 4.57 As for fig. 4.56, using rate2 reaction rates.

Table 4.5 Results of OI 6300/5577 Airglow Production Correlation

Night	Times (UT)	Ap	T_{ex} (K)	N_{max} (10^{11} m^{-3})	h_{max} (km)	β_{1S} for zero correlation	
						rate1	rate2
Post-twilight:							
40371	0.54–3.56	9	1025–875	10.4–5.5	300–360	.015±.005	.02±.01
270371	0.68–2.18	15	940–870	6–4.5	310–380	.062±.04	.08±.06
250385	-0.50–2.06	5	830–730	6.5–1.3	250–325	.027±.007	
Main peaks:							
40371	5.06–8.41	9	830-920	4.6–5.5	360-260	$.01\,^{+.02}_{-.01}$	$.01\,^{+.02}_{-.01}$
10471	2.74–6.81	26	860–940	3.7–6.8	410–250	.093±.015	.125±.02
170671	3.19–8.11	6	770–830	3.3–6.5	360–280	.13±.03	.17±.04
230485	4.34–7.50	12	700–740	0.7–2.1	320–240	.03±.03	.03±.03
240485	5.80–8.10	17	720–750	0.6–2.2	300–250	.073±.037	.08±.05
Storm peaks:							
30671	4.63-7.13	31	790-860	16–9	360–320	.07±.04	.08±.06
210485	2.09-3.15	103	860-940	13–9	420–310	.063±.018	

T_{ex} – averaged ion and electron temperatures

N_{max} – number density of electrons at F2 peak

h_{max} – height of F2 peak

The results shown in table 4.5 are rather inconclusive. The largest spread of β_{1S} values is found in the group of main (post-midnight) peaks, with no obvious general tendencies related to magnetic activity, temperature, or electron densities. The reaction rate coefficients used are of prime importance, and in fact, for the approach used here, production and quenching must independently be accurate, which is not guaranteed by a good fit of 6300 Å intensities. As anticipated, the average value of β_{1S} found using rate2 was higher than that for rate1. Neither rate set produced very consistent results, however, and the range of values was greater for rate2 than for rate1. This might tend to tip the balance in favour of rate1, or at least in favour of larger values for both production and quenching of $O(^1D)$.

The range of β_{1S} values calculated for the instances of best I_{6300} fits is (.03±.03) to (.09±.02) for rate1, (.03±.03) to (.13±.02) for rate2. It seems likely, then, that $\beta_{1S} \lesssim 0.1$. These results are quite consistent with the 1988 calculations of Zipf, but do not rule out the lower end of the range of values reported by Abreu *et al.* (1983).

An additional upper limit to β_{1S} may be inferred from Guberman (1987), using currently accepted values of the dissociative recombination coefficient, α_1. From fig. 2 of Guberman, the maximum values of $\beta_{1S}\alpha_1$ occur for the $v = 2$ level of O_2^+, and for ionospheric temperatures lie roughly in the 1.2–1.6 x 10^{-8} cm^3/s range. For the values of α_1 shown in table 4.4, these lead to an upper limit for β_{1S} of (very roughly) 0.14±.02.

In an attempt to add observational evidence to these results, a search was made of ISIS-2 satellite data obtained in 1971. Green line intensities were measured by ISIS photometers (Cogger and Anger, 1973) in the E and F regions separately, but due to the flight path of the satellite, only a few readings were taken in the vicinity of Arecibo. Only a handful of these corresponded to times when airglow experiments were simultaneously carried out at

Arecibo. The satellite data were not background corrected, and appeared to be subject to large fluctuations. Results are summarized in table 4.6.

Table 4.6 Comparison of 5577 Å airglow intensities from ISIS 2 and Arecibo

time (UT)	lat (°N)	long (°E)	I_{5577} (R) F Region	I_{5577} (R) Total	I_{5577} (R) Total (obs.)	I_{5577} (R) F region[†]	I_{6300} (R) Calc. rate1(rate2)	I_{6300} (R) Obs.
June 3, 1971								
5.85	12.4	318.5	90	220	203	58(40)	215(194)	268
7.17	11.4	290.5	67	122	146	19(13)	88(78)	133
7.78	18	286	42	125	116	19(14)	83(75)	112
June 17, 1971								
5.30*	18	267	30	130	99	15(11)	68(59)	66

*ISIS data averaged over several adjacent readings; Arecibo data interpolated between
UT= 4.71 and 5.78

[†]calculated for rate1(rate2), $\beta_{1S} = 0.1$

These data are insufficient to draw any firm conclusions. It is interesting to note, however, that in all cases the ISIS measured F-region I_{5577} intensities were substantially greater than the model calculations, even using $\beta_{1S} = 0.1$. This is true despite reasonable agreement between the total intensities observed by both instruments, indicating that the difference cannot be entirely ascribed to background contamination or to calibration uncertainties. The

passage of waves through the area is a likely cause of disagreement between observed and calculated brightnesses, particularly given the slight displacement of ISIS readings from the precise location of Arecibo. For example, $6°$ of latitude corresponds to a distance of approximately 450 km at F-region heights, and a peak calculated value of $I_{5577} \sim 100$ R was found for 6.1 UT at Arecibo on June 3, 1971. This may partially account for the discrepancy in the first data point of table 4.6.

Given the large values of F-region I_{5577} observed by ISIS 2, it is tempting to conclude from table 4.6 that the value of β_{1S} should not be less than 0.1, with higher values again implied for rate2 calculations, but the sparseness and uncertainty of the data do not permit any more than conjecture on this point. A more extensive comparison of satellite and ground-based observations might prove rather interesting.

Probably the best approach to resolving the difficulties posed by the various methods employed in this section would be a series of rocket flights. Elimination of the need for height integration would simplify the problem considerably. If simultaneous measurements of neutral species densities could also be made, reliance on a model atmosphere could be avoided, thus further reducing uncertainties.

A rocket experiment has in fact recently been performed over Natal, Brazil, in the equatorial region (Takahashi *et al.*, 1990 and Sobral *et al.*, 1992). A near-midnight flight was made to measure airglow emission profiles at 6300 Å and 5577 Å. Electron density profiles were also measured, but the MSIS-86 model was used for all neutral densities and temperatures. Thus the problem of height integration has been avoided, but other limitations remain. Using the rates of Link and Cogger (1988), the investigators found β_{1S} to vary with height in a complex fashion, with values ranging from about .02 to .13. This range certainly encompasses all the results of the correlation analysis in this thesis.

A further result of this rocket experiment with quite considerable implications for modelling of the 6300 Å nightglow was the marked variation of β_{1D} with height. Sobral *et al.* (1992) found a minimum of about 0.77 at 250 km, with values increasing above and below to about 2. This variation is not yet sufficiently well understood to be applied to ground-based studies relying on height integration of emission profiles. Bates (1992) discusses these results from a theoretical standpoint, and suggests that transport of suprathermal O(^{1}D) atoms is an important factor in the apparent profile of β_{1D}.

4.8 Tides and the Red Line Hysteresis Effect

As previously noted, the loop structure which appears in many of the calculated *vs.* observed 6300 Å brightness plots points to a need to consider dynamical processes in our airglow model calculations. Figures 4.34–4.41 and 4.49–4.52 illustrate this feature, as observed by Cogger *et al.* (1980). In many cases, the loop size was very slightly reduced by using MSIS-83 values for exospheric temperature, rather than the measured ion and electron temperatures. The variation of these temperatures was shown in figures 4.25–4.32 for the 1971 and 1976 nights; figures 4.58–4.62 show values for the (quiet) nights of 1985, along with some neutral density variations from the MSIS-83 model.

Significant post-midnight bulges in ionospheric temperature were observed for most of these nights, the greatest enhancements being seen near spring equinox, solar maximum conditions. On these nights, the temperature started rising 1–2 hours after local midnight, reaching a maximum value about 1.5 hours later, or about 0230-0300 local time (0630–0700 ut), with an amplitude in the 60–100 K range. One summer solstice night from the same year showed a much smaller increase with maximum occurring at local midnight.
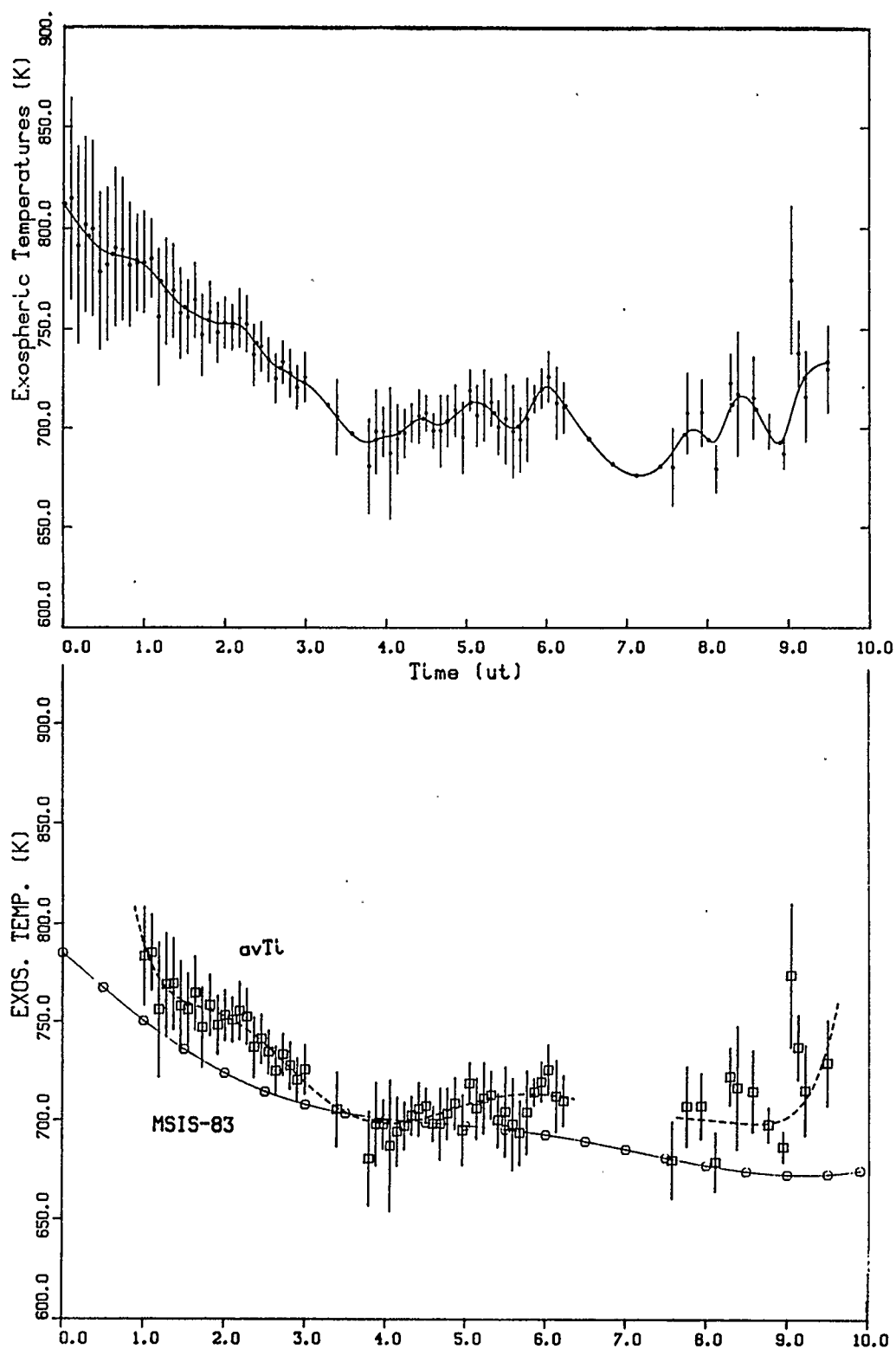
Figure 4.58 Exospheric temperatures for March 22/23, 1985.
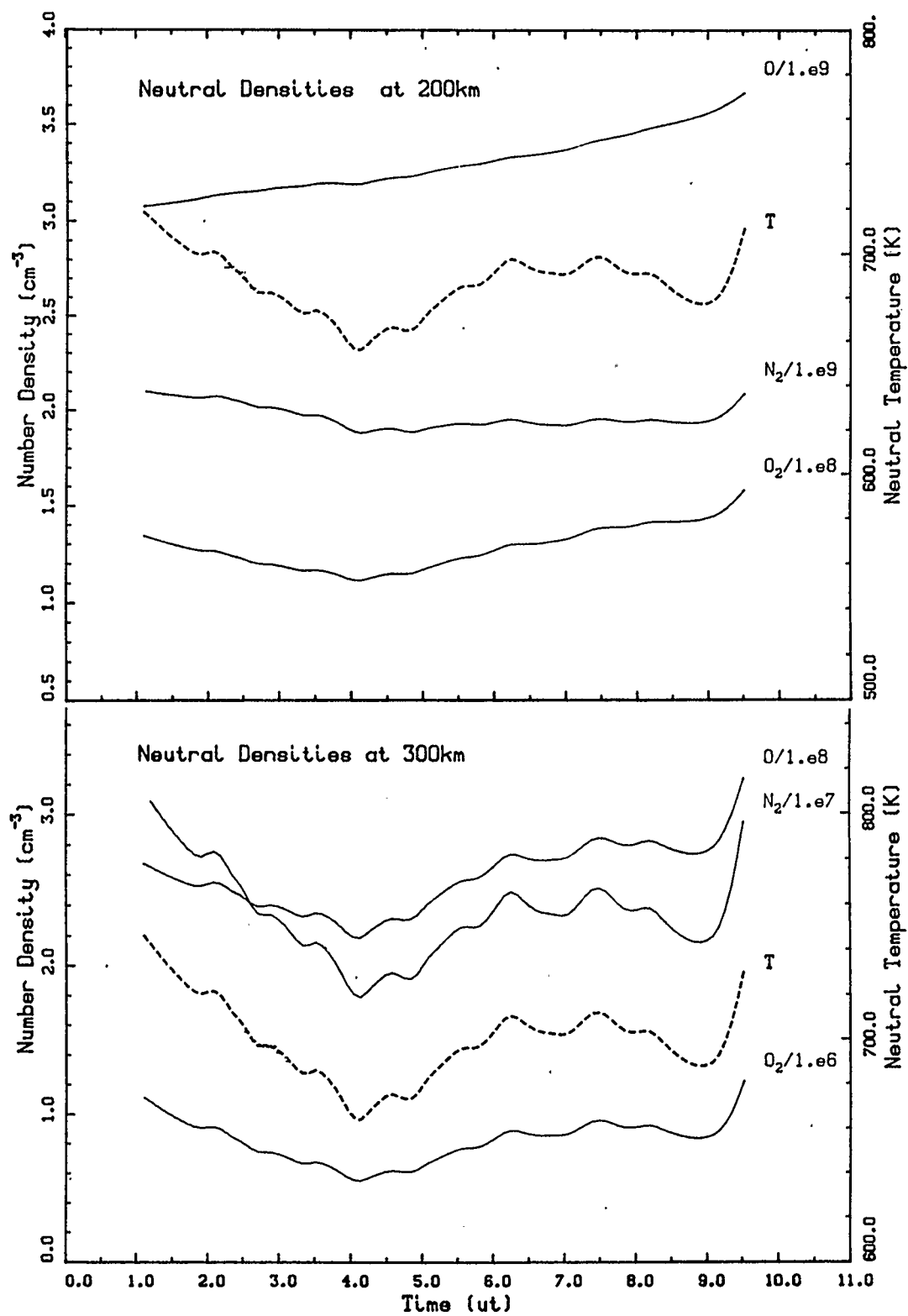Top: spline smoothing of avTi
Bottom: avTi and MSIS T_{ex}

Figure 4.59 Temperatures and neutral densities from MSIS-83 using avTi as input, March 23/24, 1985.
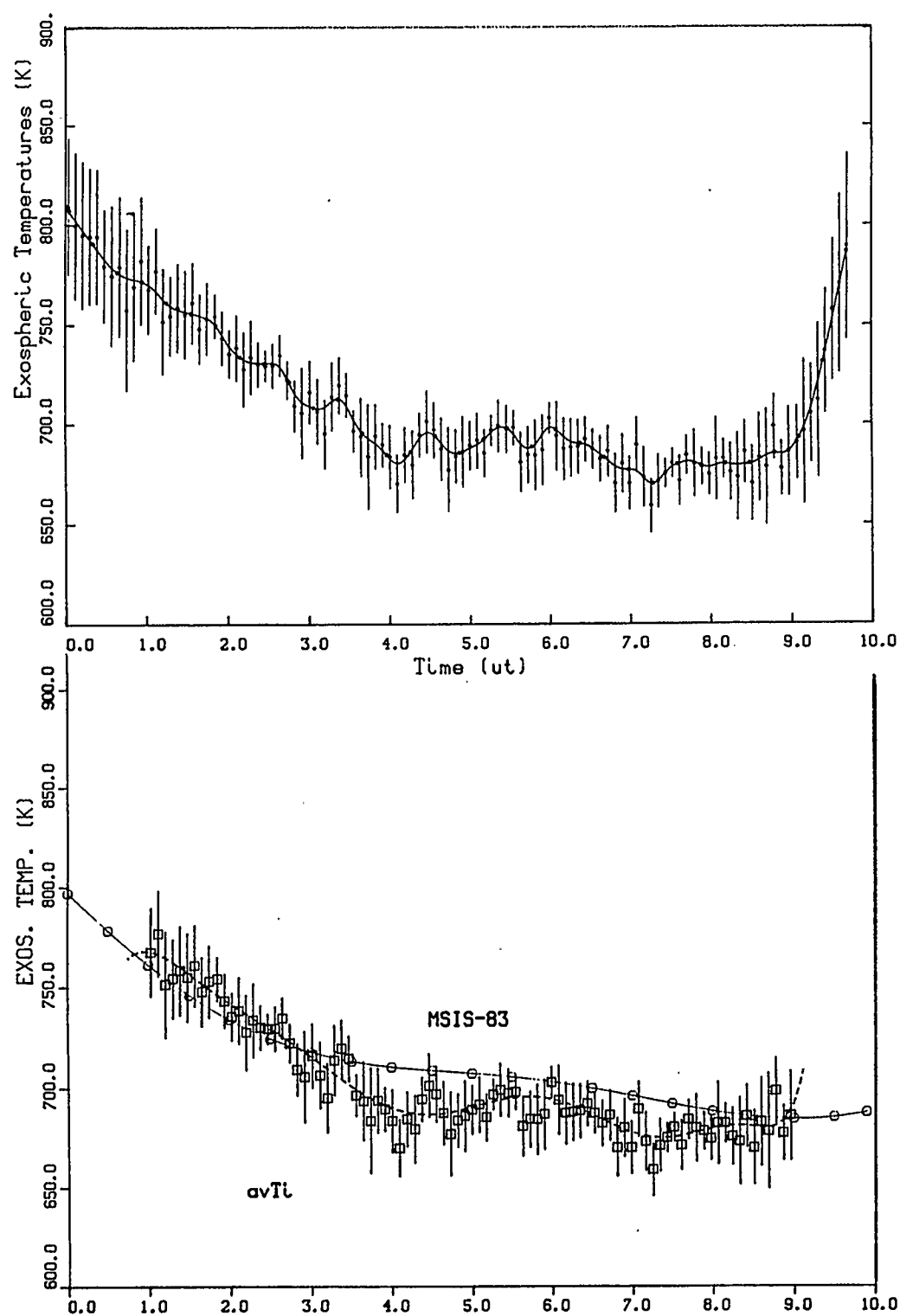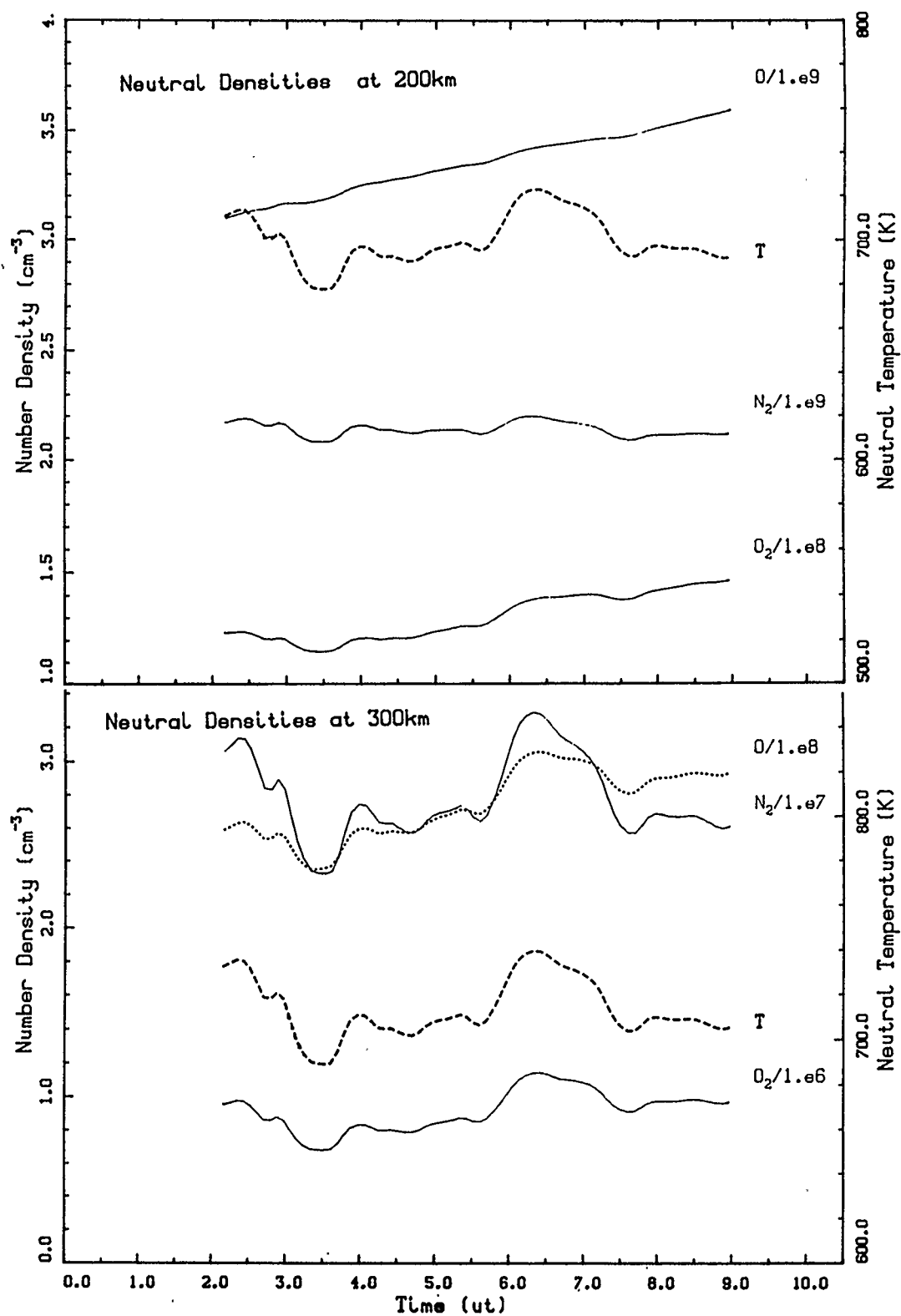
Figure 4.60 As in 4.58, for March 24/25, 1985.

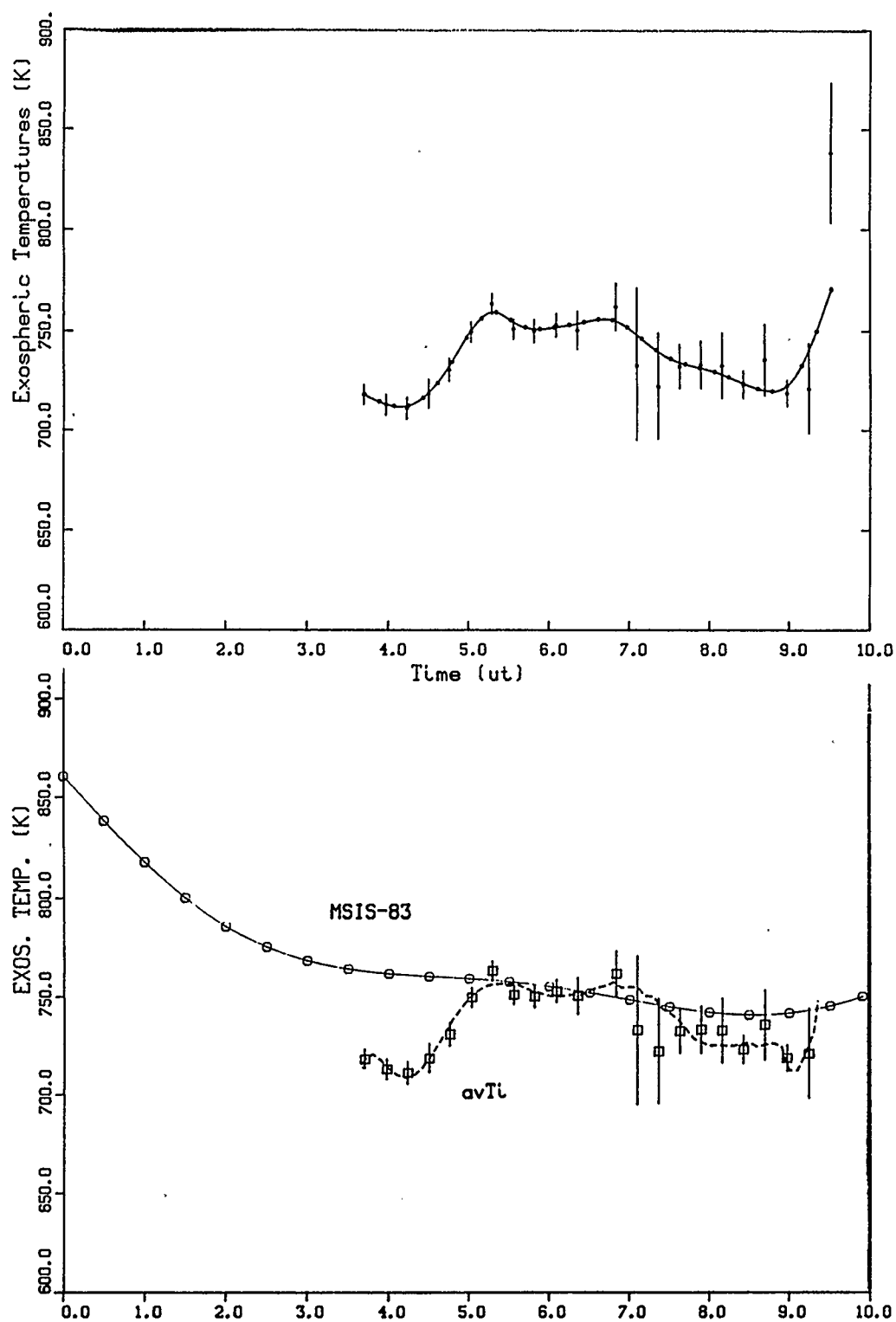**Figure 4.61** As in 4.59, for April 22/23, 1985.

Figure 4.62 As in 4.58, for April 23/24 1985.

No general trends were observed in the 1976 data (solar minimum spring equinox), but an increase of about 50 K to a maximum at 0100 local time was measured on one night. In contrast, solar minimum spring equinox measurements made in 1985 did show fairly consistent behaviour. On most quiet nights, the ion and electron temperatures started rising at about local midnight, increasing by about 30–40 K over the next 1–3 hours. Table 4.7 summarizes these results along with two other relevant parameters, the height of the F_2 peak and the oxygen red line brightness, for the nights to be used in the hysteresis study. The direction of the hysteresis loop on calculated $vs.$ observed I_{6300} plots is also given, and it might be added that in many of these cases, particularly at solar minimum, the graph was better behaved on the "up" leg, $i.e.$, when the F layer was descending, than later as the red line intensity decreased.

Some recent work on atmospheric tides may shed some light on this problem. Given the slight reduction in loop size obtained by using MSIS T_{ex} values instead of measured ion temperatures, it seemed at first that T_i might not be representative of thermospheric conditions. However, the report by Mayr $et\ al.$ (1979) showing that neutral densities may be out of phase with temperature near 200 km altitude reduces the apparent inconsistency. A comparison of several models calculating tidal effects on thermospheric temperature, with the measured ion temperatures, is shown in table 4.8. Most of these calculations are for the semidiurnal tide, which should be the most significant in the post-midnight (local time) period. Amplitudes and phases vary somewhat with altitude. There is good agreement in most cases between model/measured variations in neutral temperature and the Arecibo ion temperature measurements, indicating that our values of avTi may well represent the behaviour of the neutral atmosphere. Day to day variability in atmospheric

Table 4.7 Measured changes in ionospheric temperature, F_2 layer peak and airglow intensity, with times (ut) extreme values first attained.

| night | avTi | | h_{max} | | I_{6300} (obs.) | | hysteresis sense |
	t (max)	$\Delta T(K)$	t (min)	Δh_{max}	t (max)	$\Delta I(R)$	(cw = clockwise acw=anticlockwise)
40371	7 ut	90	7.2 ut	80	7.3 ut	120	cw (slight)
270371	6.5	60	7	80	6.6	70	cw
10471	6.3	90	6.6	150	6.0	180	cw
170671	4	20	6.8	60	6.4	60	acw
260476	5	50	5.4	70	5.8	120	cw
290476	–	–	6.3	90	6.6	50	cw
230385	6	30	8	100	7.8	30	acw (cw top loop)
240385	6.2	40	6.3	100	6.8	50	cw
230485	6.5	30	6.3	100	5.9	70	acw
240485	5.2	40	7	100	6.6	80	cw

tides is large, so it should be expected that some nights of data show behaviour quite different from the above. A closer examination of the temperature *vs.* time graphs reveals a possible separation of semidiurnal and terdiurnal peaks, by anywhere from one to three hours (*cf.* results of Hedin, Spencer and Mayr, 1980).

Looking at the model for tidal variations in composition of Forbes (1978), it is apparent that large changes in magnitude and particularly in phase, with latitude, will make it very

Table 4.8 Amplitudes and Phases of Tidal Variations in Thermospheric Temperature

Model	Amplitude (ΔT)	Phase (φ, local time)
Mayr *et al.* (1979); order up to m=4 SSMIN, equinox, equatorial	~10% (70-80K)	0200
Forbes and Garrett (1979)	30–40 K	0100–0200
Hedin, Spencer & Mayr (1980) a) semi-diurnal ~2–3% (15–25 K) SSMIN, equatorial (AE-E meas.) b) terdiurnal ~1–2% (7–15 K)		0300–0330 0000–0200
Forbes (1982b) 18° latitude, equinox	50–60 K	0600
Fesen *et al.* (1986) equinox, using TGCM	SSMAX: 40–70 K	0215
	SSMIN: 35 K	0230
This work - Arecibo meas. (T$_i$) 18° latitude, equinox	SSMAX: 60–100 K	0230–0300
	SSMIN: 30–40 K	0200–0300

Table 4.9 Semidiurnal Composition Variations at 18° Latitude

Altitude (km)		relative amplitude (phase, local time)		
		N$_2$	O$_2$	O
225	SSMAX	.04 (0400)	.05 (0420)	.023(0815)
	SSMIN	.06 (0340)	.07 (0340)	.035(0240)
250	SSMAX	.04 (0315)	.05 (0320)	.02 (0745)
	SSMIN	.1 (0250)	.12 (0300)	.06 (0210)
275	SSMAX	.06 (0230)	.08 (0245)	.025(0200)
	SSMIN	.14 (0200)	.17 (0210)	.09 (0130)

difficult to apply any of the above model results to Arecibo. Most of both the satellite measurements and theoretical calculations are for the equator at solar minimum, equinox conditions. Forbes has given the most extensive coverage, supplying semidiurnal amplitudes and phases for N_2, O_2 and O (among others) at 0° and 40° latitude, for both solar maximum and solar minimum. They differ from the measurements of Hedin, Spencer and Mayr (1980) mainly in having much larger amplitudes - the phases are in reasonable agreement. Table 4.9 gives very approximate values, interpolated from those of Forbes (1978), for the latitude of Arecibo, 18° N. There is no physical justification for this interpolation.

An examination of the calculated *vs.* observed 6300 Å brightness plots for March/April 1971 (SSMAX) reveals the following. All three exhibit clockwise hysteresis, though the individual shapes are quite different, and small waves with periods roughly 30–40 minutes. To close the loops would require changes to calculated I_{6300} of about -10 to 20% centred on or near the the time of maximum avTi, followed by +15 to 25% an hour later. Total perturbation duration would be about two hours. The magnitudes given in table 4.9 are not sufficient to accomplish these changes, but the direction is right. As the F layer descends, the times of maximum $[N_2]$ and $[O_2]$ become later, leading to $[N_2]$ and, especially, $[O_2]$ less than expected, hence lower I_{6300}. The actual peaks are encountered about an hour later, resulting in enhanced I_{6300} over that calculated using MSIS-83. The sizes of the temperature bulges are quite large, which could amplify this effect, and in addition the terdiurnal amplitudes given by Hedin, Spencer and Mayr are significant, being of the same order as their semidiurnal amplitudes.

Two of the April 1976 (SSMIN) plots exhibit sizable clockwise loops, and small waves with periods of about an hour. Unfortunately, the temperature data for these nights do not

cover enough time to quantify the post-midnight enhancement. The changes in I_{6300} required to close the loops are quite different from the above, as no decrease near the temperature maximum seems necessary. Large increases beginning immediately after the peak in I_{6300} and lasting about 1.5 hours are required, with amplitudes of 30% (April 25/26) and 50% (April 28/29). According to the models, amplitudes of composition perturbations are expected to be larger at solar minimum (see table 4.9), but again they do not appear sufficient to explain the increase in airglow brightness.

The June solstice night of 1971 and the first March night from 1985 both have anticlockwise loops, and in both cases the I_{6300} peak occurs about two hours after the peak in avTi. This supports the hypothesis that tidal composition variations are at least in part responsible for the red line hysteresis effect.

Data from Mar 23/24, Apr 22/23, and Apr 23/24, 1985, may be relevant to this discussion. Significant clockwise loops appeared on Mar 23/24 and Apr 23/24, when double peaks in ion temperatures were also seen. The large excursion in calculated vs. observed I_{6300} appearing on March 23/24 (fig. 4.50) corresponds to the time between the first temperature peak and the maximum observed 6300 Å brightness, when, according to tidal theory, the neutral densities are rising rather than falling. Part of the size of the loop in this case may be due to a bump in the background reading of the photometer. On April 23/24, the second avTi maximum coincides with the peak in I_{6300}, and this night most closely resembles those of April, 1976.

Finally, the results for April 22/23, 1985, are a little puzzling. The loop is anticlockwise despite the peak intensity occurring half an hour before $T_i(max)$. As in April 1976, both this and the following night show small, one-hour waves in calculated vs. observed red-line brightness.

All of the calculations in this section have used our original set of reaction rates, rate1. The calculated *vs.* observed brightness plots show that for most cases the loops are smaller for rate2. This is offset, however, by the fact that greater changes in neutral densities (by about 50%) are required to produce the same changes in I_{6300}. It is also often the case that calculated values for I_{6300} using rate1 are closer to observed values than those using rate2. These rather qualitative tidal considerations do not, therefore, tip the balance in favour of either set of rates.

A more quantitative investigation may be possible using recent models such as the one presented by Roble *et al.* (1988). They found a much larger midnight temperature bulge than that of MSIS-86, in agreement with Arecibo ion temperature measurements. This adds support to the use of measured T_i to represent neutral temperature variations, as well as evidence that large day-to-day changes in atmospheric tides lead to their effects being averaged out by models such as MSIS. On a given day, therefore, tidal amplitudes may well be big enough to produce the observed red line hysteresis. In addition, tidal density perturbations may resolve the poor fit generally obtained in the post-twilight decay.

One further possible implication of the tide models examined in this section has to do with the β_{1D} profile calculated by Sobral *et al.* (1992). They found a minimum in β_{1D} at about 250 km, which corresponds quite closely to the amplitude minimum of the semidiurnal tide found both theoretically (Forbes, 1978) and experimentally (Hedin, Spencer and Mayr, 1980). Application of tidal perturbation theory to the results of Sobral *et al.* may reduce the variation of β_{1D} with height, and give renewed credibility to ground-based studies of F-region airglow. These considerations illustrate even more the benefits of *in situ* measurements of neutral densities as well as airglow emission rates.

4.9 Effects of Magnetic Storms on Low Latitude Airglow

Observations were made during two magnetic storms - a relatively minor one in June, 1971, and a much more active one in April, 1985. The corresponding daily Ap values were 31 and 103, respectively. The two showed some similarity in features (see fig. 4.28 and 4.54(a) for June 2/3, 1971, and figs. 4.6, 4.12 and 4.45 for April 20/21, 1985). These include wave structure in both red and green line intensities and ionospheric temperatures as functions of time, increased electron densities during the early hours and F_2 layers higher than normal. There was also a high degree of correlation between observed I_{6300} and I_{5577}, and the analysis of section 4.7 yielded quite consistent results for β_{1S} between these two nights.

All of these common features were more striking in the 1985 storm, and, in addition, significant wave structure was observed in h_{max} and n_{max} *vs.* time and in electron density profiles. A substantial increase in ionospheric temperature was observed in the latter part of the April, 1985, storm night, followed by the virtual disappearance of the F region. Hence, while the 1971 storm showed only a positive phase over Arecibo during the period of observations, significant positive and negative phases were evident during the major storm of 1985. In fact, the three successive nights of observations in April, 1985, give good coverage of positive, negative and recovery phases. The progression of this latter storm is illustrated by the Kp and Dst indices shown in figure 4.63.

Another major difference between the 1971 and 1985 storms is in the ability of the photochemical model to reproduce photometric 6300 Å brightnesses. The earlier data were modelled quite successfully, with the exception of a persistent "background" of about 20 R, and with surprisingly little dependence on exospheric temperature. In fact, it can be seen in fig. 4.28 that variations in I_{6300} and T_i do not generally coincide, except for the
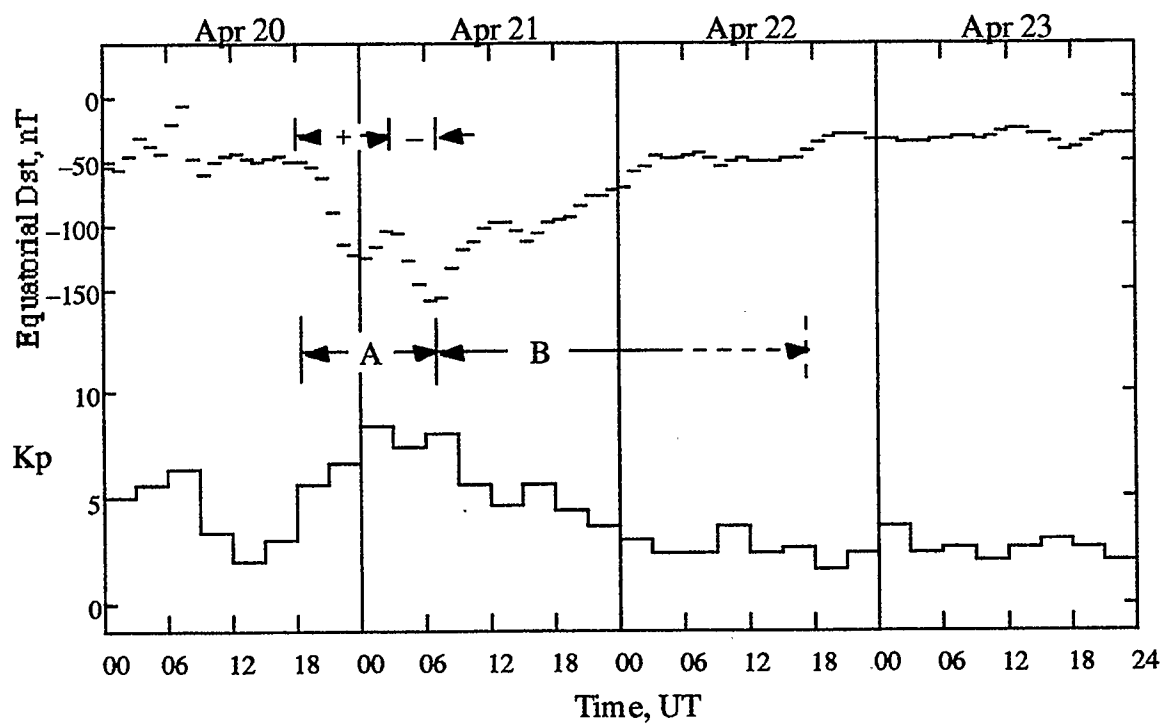
Figure 4.63 Geomagnetic activity indices, Dst and Kp, for the storm of April, 1985.
A: main phase; B: recovery phase. Periods of increasing and
decreasing electron density during the main phase are indicated by plus
and minus signs.

main peak at about 0600 h. Therefore, the standard dissociative recombination model, together with MSIS-83, is sufficient to describe the 6300 Å brightness variations on this night, leaving only the small excess background to be explained.

On the other hand, the night of April 20/21, 1985 presents a much more perplexing situation. (See figs. 4.12–4.14, 4.45–4.47 and 4.64–4.67 for time-dependent parameters.) Very fine wave structure in the photometer data ($\tau \sim$ minutes) cannot be adequately modelled given the coarser temporal resolution of the radar observations. The gross variations in brightness are reasonably well reproduced in the first three hours of data, but after 0400 h the model appears to break down. This corresponds with a sharp increase in upper F-region ion and electron temperatures. It should be noted that these measured temperatures were used as input to the MSIS-83 program; a far worse fit was obtained using MSIS model T_{ex} values. The breakdown in the fit of I_{6300} values follows the beginning of the negative storm phase, signalled by a large drop in electron densities. Thus it would seem that our basic model works reasonably well during positive ionospheric storms.

The most remarkable departure of observed from calculated 6300 Å brightness is the large peak occurring at 0500 h, which coincides with a large peak in avT_i and a small peak in n_{max}, but no significant lowering of h_{max}. There is very little difference between the results for the two different sets of rates, implying that the particular quenching scheme used is not the main factor. No irregularities were seen in the ion/electron temperature profiles, and the proton/electron ratio for this period was particularly low and therefore an unlikely source of error.
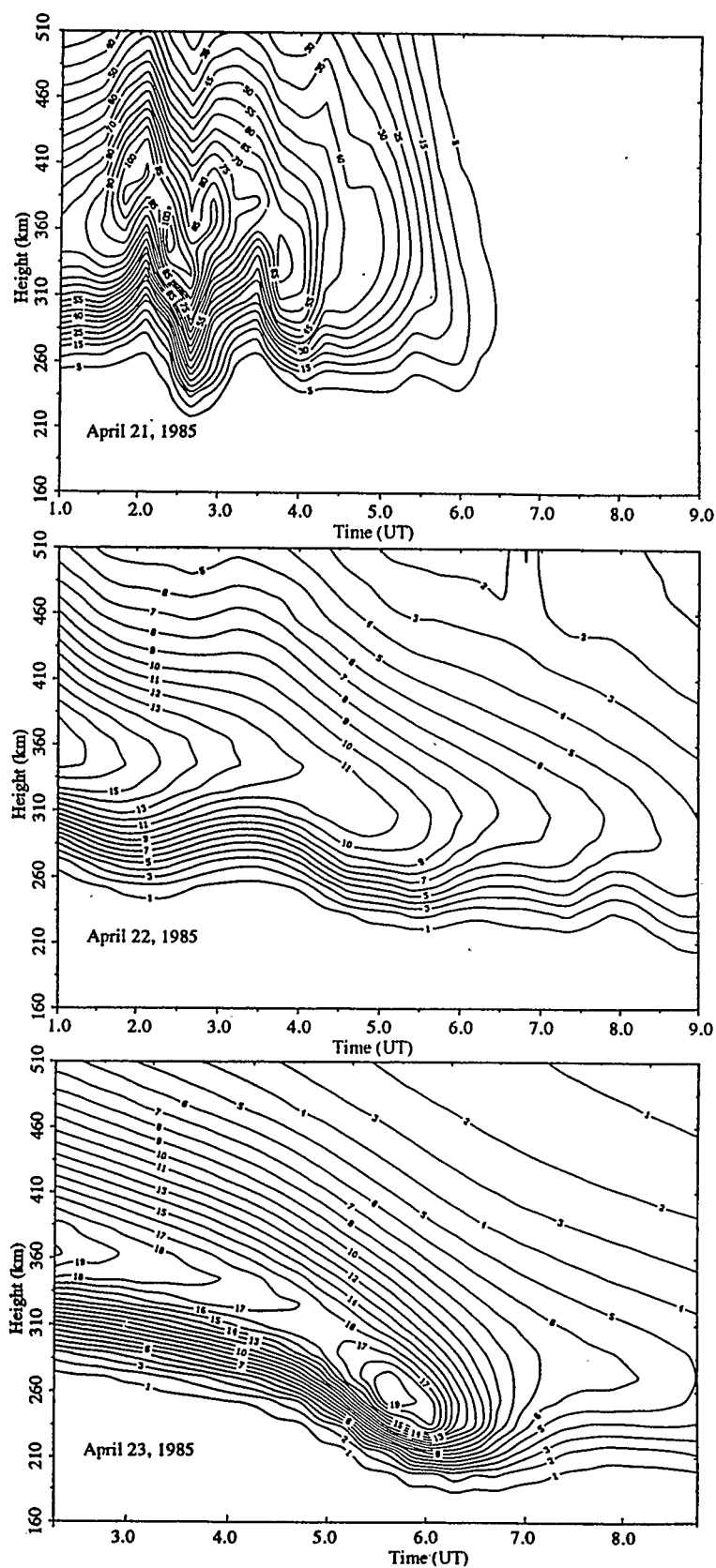
Figure 4.64 Electron density contour maps (Barker profiles); contour scale 10^4 cm^{-3}.
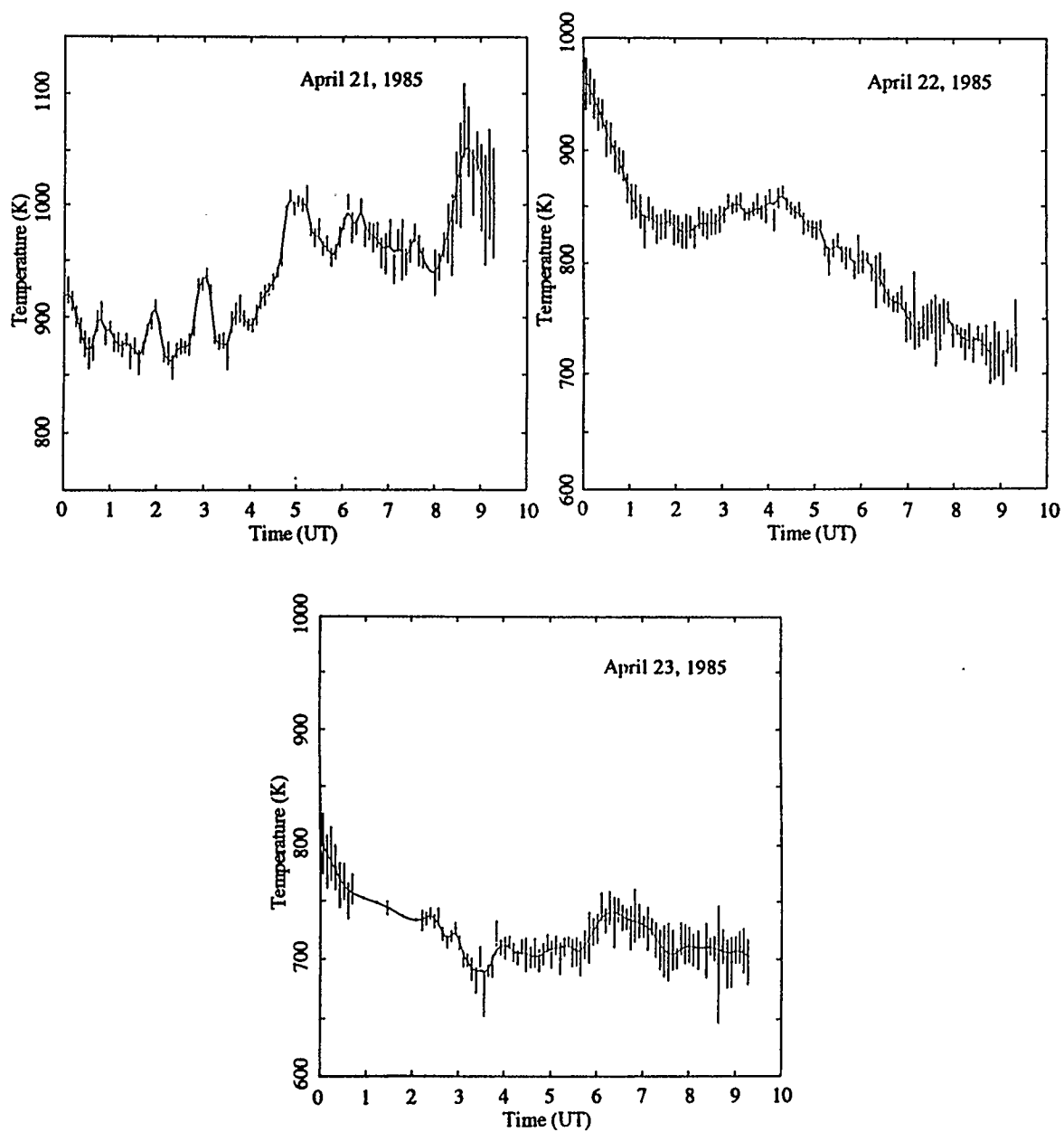
Figure 4.65 Spline smoothed avTi calculations of exospheric temperatures
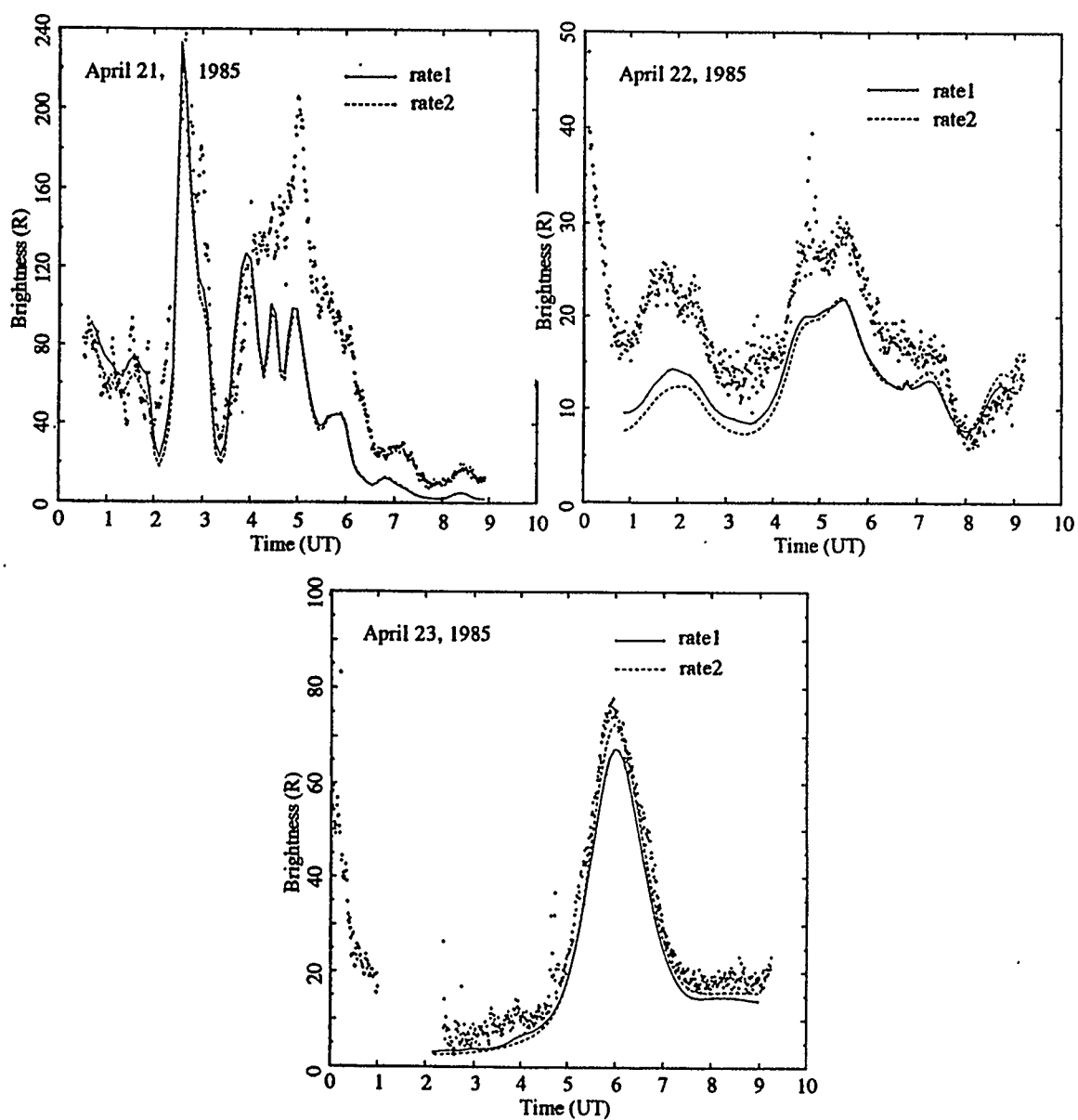
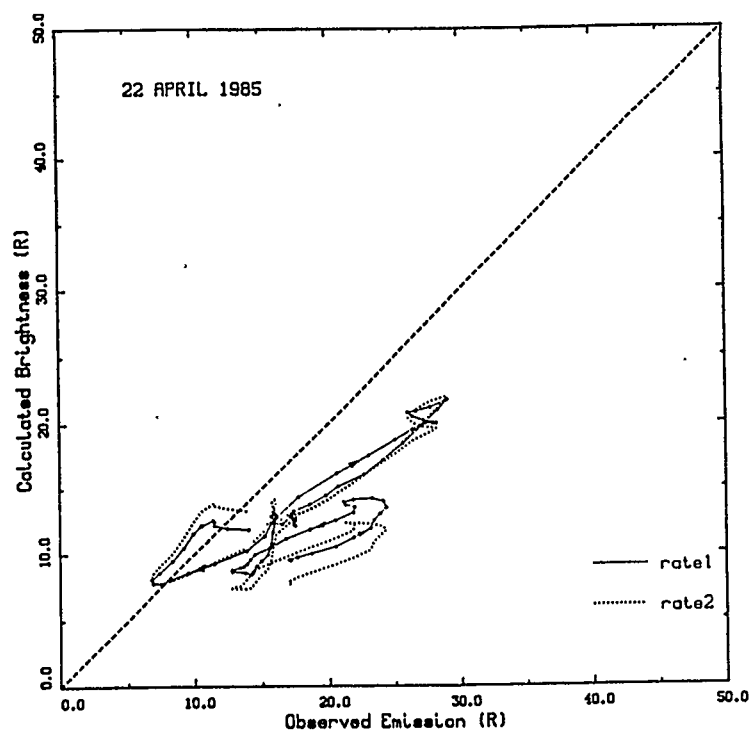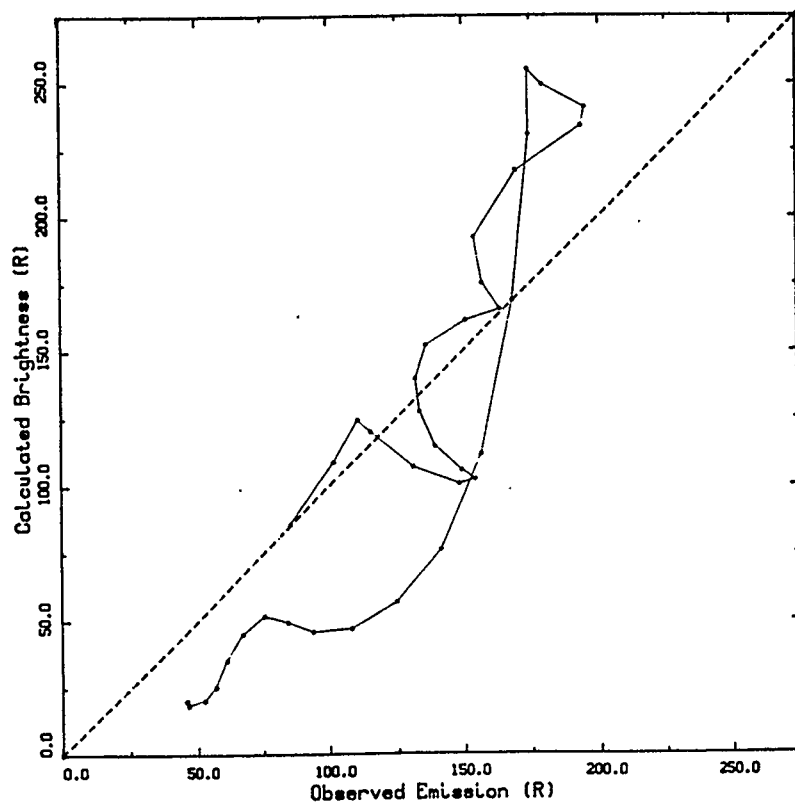Figure 4.66 Observed and calculated brightness of 6300 Å airglow

Figure 4.67 Calculated vs. observed I$_{6300}$:
top - April 20/21, 1985 (rate1, first peak)
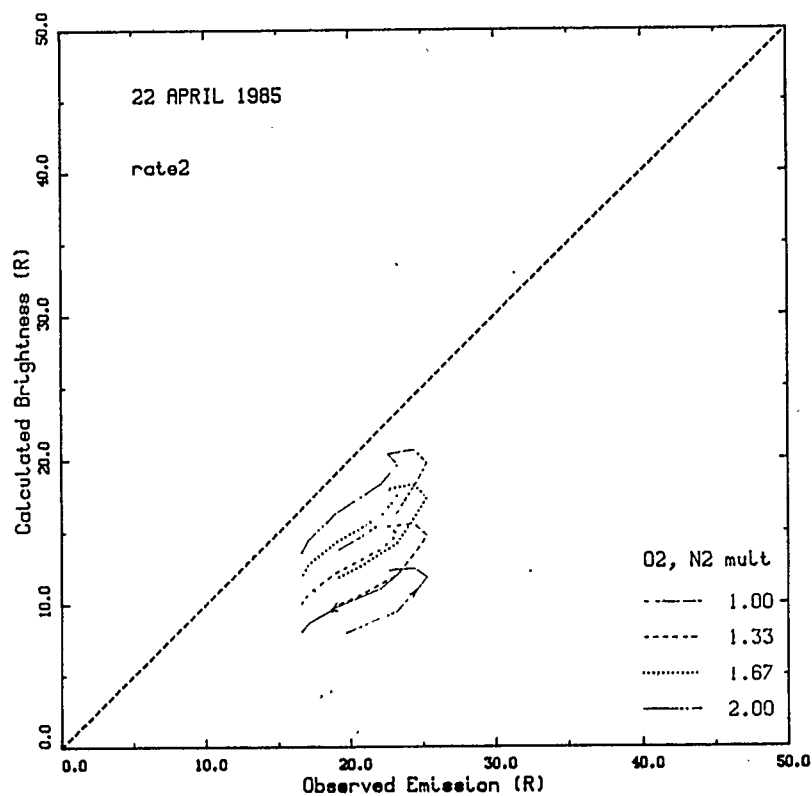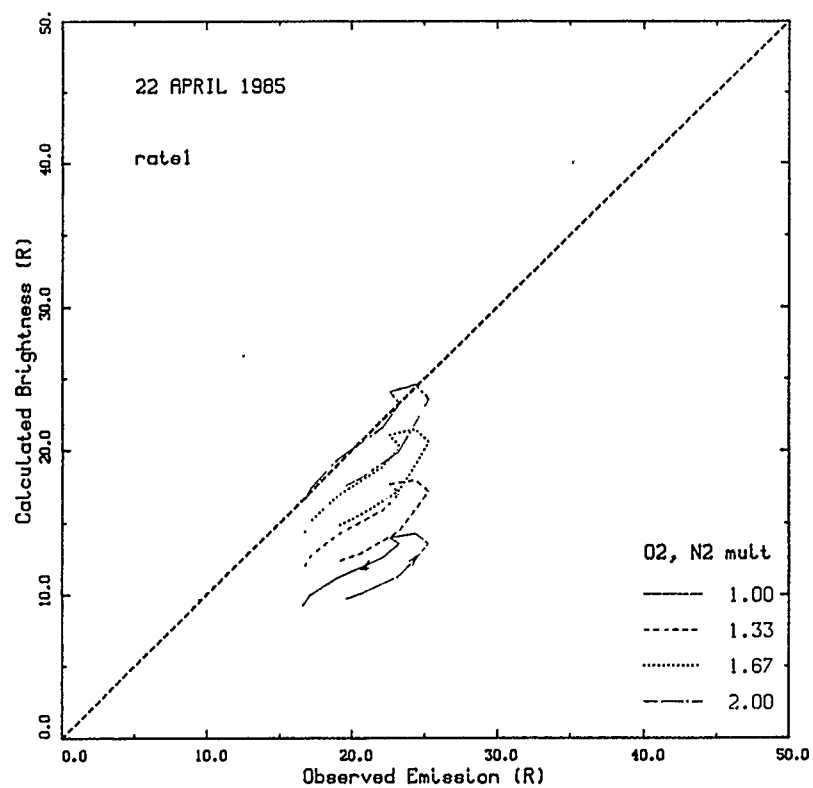bottom - April 21/22, 1985 (whole night)

Figure 4.68 Calculated vs. observed I_{6300} with modified neutral atmosphere (molecular densities increased by factors shown), Apr 21/22, 1985, peak 1.
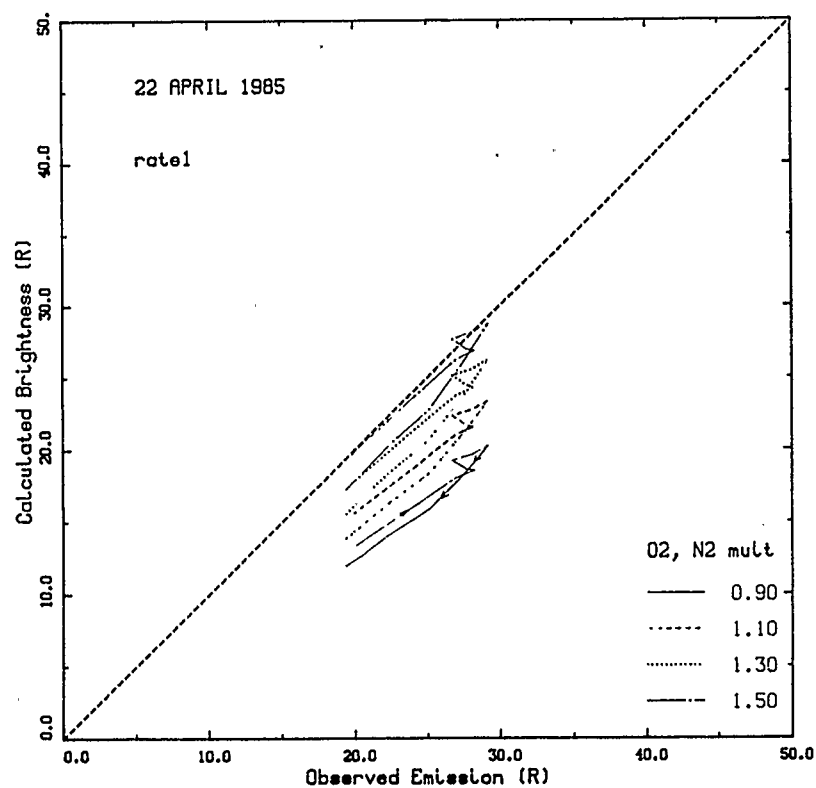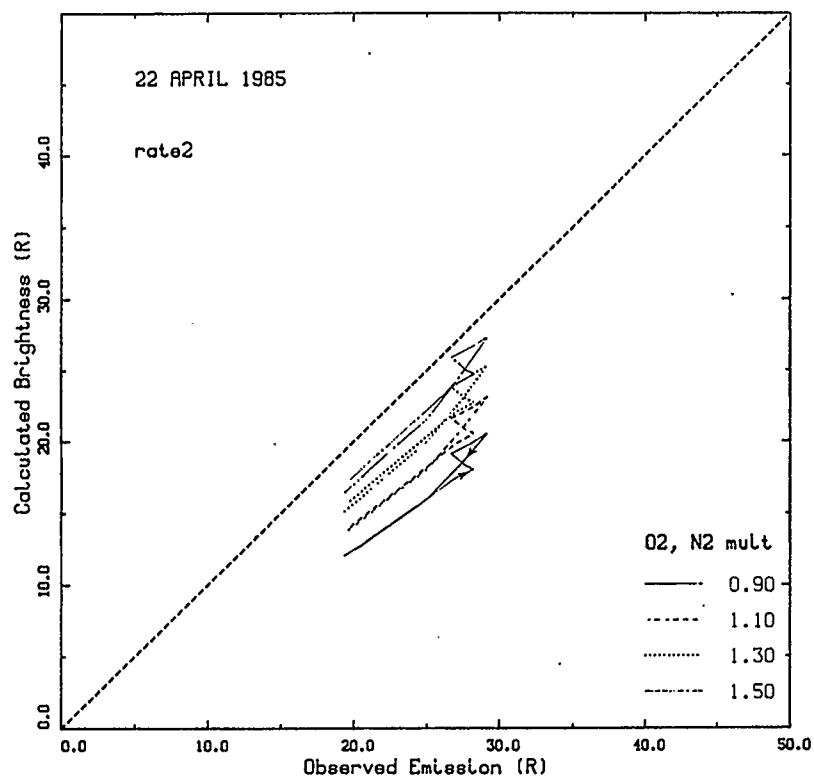
Figure 4.69 As for 4.68, Apr 21/22, 1985, peak 2

The considerable enhancement of I_{6300} over calculated values presents an interesting problem. The possibility of a SAR arc can be eliminated because the 5577 Å brightness is similarly enhanced; in fact, the red and green lines show remarkable correlation throughout the night. This suggests either a suppression of E_{5577} or a correlation of E- and F-region green line production. Also, the latitude of Arecibo is rather low for SAR arcs, which tend to be observed at higher mid-latitudes (~50–60° dip latitude, see Rees and Roble, 1975).

Low latitude particle precipitation associated with geomagnetic disturbances has been observed and discussed by several authors (Tinsley, 1979, Tinsley *et al.*, 1986 and 1988, Sahai *et al.*, 1988 and 1990, Rassoul *et al.*, 1992). Although I_{6300} may be significantly increased by hot electron precipitation (kinetic energy ~ eV), this mechanism cannot account for large increases in I_{5577} due to higher energy requirements, as in SAR arcs. Precipitation of keV ions and neutrals may result in higher energy airglow emissions (H, He^+, N_2^+ emissions have been measured), but the effect on I_{5577} and I_{6300} appears to be negligible. Therefore particle precipitation may be ruled out as a signficant factor in the direct production of OI 5577 and 6300 Å emissions at low to mid-latitudes, though it may contribute indirectly through heating and composition changes.

Discussions of heating and composition changes resulting from magnetic disturbances may be found in, for example, Rishbeth *et al.* (1985), Prölss (1987), Buonsanto *et al.* (1990), Miller *et al.* (1990) and Reddy *et al.* (1990). It seems to be well accepted that the negative storm phase is associated with a marked increase in the ratio of molecular to atomic number density, in particular the ratio $[N_2]/[O]$ in the F region. This increase may be much greater than that due to temperature alone, and does not appear well-represented in the MSIS-83 model. It seems unlikely that use of MSIS-86 results would change our calculations

appreciably, given the inherent averaging in such models as compared with the unique nature of each geomagnetic storm.

By reference to equations 4.3.20–4.3.23, the effects of various composition changes may be estimated. It is apparent that a large increase in $[N_2]$ and $[O_2]$ will significantly increase both I_{5577} and I_{6300}, and, in fact, the relative enhancement of I_{5577} will be even greater than that of I_{6300} due to the lack of quenching. The higher the F_2 peak, the greater the effect. For example, at 0500 ut on April 21, 1985, the effect of doubling $[N_2]$ and $[O_2]$ will be to increase emission rates at 300 km by nearly 100% at 5577 Å, and about 70% at 6300 Å. See figures 4.68–4.69 for the effects of varying model molecular density values. Clearly, such composition changes could go a long way towards improving the fit between observed and calculated brightnesses. A detailed calculation involving total electron content and vertical plasma motions might help to establish the magnitude of such changes, and hence the likely effect on airglow intensities. Rapid up/down plasma movements and ion drag may also have considerable effects.

To summarize, then, the positive phase storms resulting from a geomagnetic disturbance do not significantly affect the calculation of I_{6300} using the present model and MSIS-83. In contrast, the negative and recovery phases show significant enhancements in both I_{6300} and I_{5577}, which indicates that substantial increases in $[N_2]$ and particularly $[O_2]$ are quite likely. A closer examination of the total recombination rate and vertical plasma motions, as compared with the actual decrease in F-region electron content, could help to verify such composition changes.

Chapter 5

Summary and Conclusions

In this thesis, simultaneous photometric and incoherent scatter radar observations made at the Arecibo Observatory have been analyzed in an attempt to model visible atomic oxygen emissions, in particular the red line at 6300 Å and the F-region contribution to the green line at 5577 Å. Radar measurements of electron densities and ion temperatures made on selected nights of 1971, 1976 and 1985 were used as input to a simple photochemical equilibrium model to calculate expected 6300 Å brightness values. The model incorporated some recent determinations of reaction rate coefficients and predictions of the MSIS-83 model atmosphere. These calculations were compared with the photometric measurements, with the following results.

1. Reasonable fits were obtained for most of the nights studied, and for both sets of rate coefficients used in the calculations. Taken in groups according to year, fits were best for the 1976 data, followed by the 1971 set, with the 1985 measurements the least well reproduced. Problems with calibration were suspected for some of the 1985 radar data.

2. Very little difference was found between fits that used MSIS-83 predictions of exospheric temperature and those that used measured ion and electron temperatures, except during the geomagnetic storm of April 20/21, 1985. In many cases, the fit was slightly better when MSIS-83 temperatures were used.

3. The red line hysteresis effect (loops appearing in calculated $vs.$ observed I_{6300} graphs), consistently observed to run clockwise with increasing time in the spring months of

1971 and 1976, was less remarkable in 1985. In addition, the hysteresis was found to proceed anticlockwise on some graphs in 1985.

4. On average, the original rate coefficients ("rate1") chosen for this study yielded somewhat better results than the comparison set ("rate2") of Link and Cogger (1988). Both sets gave good fits, however, and the difference was insufficient to prefer one set over the other.

5. Measurements of $[H^+]/[e]$ at high altitudes made in 1985 showed very low values, confirming assumptions made in the model about the relative unimportance of the H^+ species at these altitudes.

6. Brightness of the 6300 Å line was found to be relatively insensitive to the abundance of atomic nitrogen. The one calculation seriously affected by [N] was that of 5577 Å brightness in the post-twilight decay period, rendering these times unsuitable for analysis of the green line.

An attempt was made to pin down the F-region contribution to the total brightness at 5577 Å using the same photochemical model, thereby setting some limits on the efficiency of $O(^1S)$ production from dissociative recombination of O_2^+. Difficulties inherent in this approach (*i.e.*, using ground-based observations) led to rather inconclusive results, and inclusion of ISIS 2 photometric measurements did not help to clarify the situation. Some conclusions made and problems encountered were:

1. Somewhat more consistent results were obtained with rate1, our original set of rate coefficients, than with rate2 (Link and Cogger, 1988).

2. A reasonable range for β_{1S} appears to be .03–.1 per recombination.

3. Heavy reliance on many rate coefficients, a model neutral atmosphere, and absolute

　　measurements of electron density limit the usefulness of this approach.

These results are consistent with those of Sobral *et al.* (1992) and Zipf (1988), and overlap the lower range of values found by Abreu *et al.* (1983). The very large variation of β_{1S} with height found by Sobral *et al.* introduces a serious complication to ground-based measurements relying on height integration of emission rates for comparison with photometric observations.

The variation with height of β_{1D}, found by the same authors, is even more problematic. Bates (1992) has suggested that much of the variation may be attributed to transport of suprathermal $O(^1D)$ atoms. Another factor may be the departure of neutral densities from the MSIS-86 model used by Sobral *et al.* Theory and measurements of atmospheric tides show that such deviations are quite likely, and that both the magnitude and the time (phase) vary considerably with height. Clearly, *in situ* measurements of neutral densities, along with ionospheric parameters and airglow emission rates, would do much to isolate these effects.

The possibility that atmospheric tides cause the red line hysteresis loops was investigated. Preliminary results definitely support this hypothesis, showing that modes $m \geq 2$, responsible for the post-midnight temperature bulge, also lead to neutral density fluctuations in the required directions. Amplitudes needed to close the loops range from about 20% to 50% for rate1, higher for rate2. These are larger than expected from existing models, but the differences do not appear irreconcilable. Transport of suprathermal $O(^1D)$ atoms may also play a role in the hysteresis, but according to the results of Schmitt *et al.* (1981) and Yee (1988), this should not be a major factor.

Some of the data obtained from Arecibo show the effects of geomagnetic disturbances, a small one in June, 1971, and a large one in April, 1985. The model used to calculate 6300 Å brightness worked very well during the positive phases, but failed to reproduce observations during the large negative phase of April 21, 1985. There appear to be two main reasons for this discrepancy. The first is a likely enhancement of $[N_2]$ and particularly $[O_2]$ over MSIS-83 predictions, on the order of a factor of 2. Secondly, the F region moved rapidly up and down, and the effects of this have not been thoroughly considered. Particle precipitation or SAR arcs have been ruled out due to the high degree of correlation between 6300 Å and 5577 Å brightnesses.

Inclusion of atomic oxygen quenching in the atmospheric model was effective in reproducing observed trends. Introduction of this process into models used in future work is recommended whether or not the result of Chen et al. (1978) is adopted for the oxygen charge exchange rate k_1.

Other suggestions for further study include the use of the MSIS-86 neutral atmosphere with the introduction of realistic tidal perturbations. These could be estimated from measured ion temperatures and vertical velocity components. The results could then be applied to both the red line hysteresis effect and the variablity of quantum efficiencies of $O(^1S)$ and $O(^1D)$ with altitude.

Incorporation of dynamic effects and recombination could be used to investigate neutral atmosphere changes during a geomagnetic disturbance, and to indicate whether the need exists for an extra source of excited oxygen atoms in the F region in this case.

The role of molecular ions has not been fully investigated, and their importance in the lower F region indicates a need for further study in this area. Due to a lack of data in this region, such a study would necessarily be quite theoretical.

In conclusion, the photochemical model employed, along with the MSIS-83 neutral atmosphere, reproduced 6300 Å brightnesses quite adequately under most circumstances. Solar minimum and maximum conditions have been covered equally well, with equally good results.

Bibliography

Abreu, V.J., S.C. Solomon, W.E. Sharp and P.B. Hays, "The dissociative recombination of O_2^+: the quantum yield of $O(^1S)$ and $O(^1D)$," J. Geophys. Res. 88, 4140–4144, 1983.

Abreu, V.J., J.H. Yee, S.C. Solomon and A. Dalgarno, "The quenching rate of $O(^1D)$ by $O(^3P)$," Planet. Space Sci. 34, 1143–1145, 1986.

Ahlquist, N.C. and R.J. Charlson, "Measurement of the wavelength dependence of atmospheric extinction due to scatter," Atmos. Envir. 3, 551–564, 1969.

Anderson, D.N. and R.G. Roble, "Neutral wind effects on the equatorial F-region ionosphere," J. Atmos. Terr. Phys. 43, 835–843, 1981.

Banks, P.M. and G. Kockarts, Aeronomy, Academic Press, New York, 1973.

Barbier, D., "Interprétation de la luminescence nocturne de la raie rouge de l'oxygène," C.R. Acad. Sci. Paris 244, 2077–2080, 1957.

Bates, D.R., "Forbidden oxygen and nitrogen lines in the nightglow," Planet. Space Sci. 26, 897–912, 1978.

Bates, D.R., "Recombination in the normal E and F layers of the ionosphere," Planet. Space Sci. 36, 55–63, 1988.

Bates, D.R., "Emission of forbidden red and green lines of atomic oxygen from the nocturnal F region," Planet. Space Sci. 40, 893–899, 1992.

Bauer, S.J., Physics of Planetary Ionospheres, Springer-Verlag, New York, 1973.

Beer, T., Atmospheric Waves, John Wiley & Sons, New York, 1974.

Behnke, R.A., Vector Measurements of the Ion Transport Velocity with Applications to F-Region Dynamics, Ph.D. Thesis, Rice University (Houston), 1970.

Blanc, M., "Electrodynamics of the ionosphere from incoherent scatter: a review", J. Geomagn. Geoelec. 31, 137-164, 1979.

Brinton, H.C. , M.W. Pharo, III, H.G. Mayr and H.A. Taylor, Jr., "Implications for ionospheric chemistry and dynamics of a direct measurement of ion composition in the F_2 region," J. Geophys. Res. 74, 2941–2951, 1969.

Buonsanto, M.J., J.C. Foster, A.D. Galasso, D.P. Sipler and J.M. Holt, "Neutral winds and thermosphere/ionosphere coupling and energetics during the geomagnetic disturbances of March 6–10, 1989," J. Geophys. Res. 95, 21033–21050, 1990.

Burnside, R.G. Dynamics of the Low-Latitude Thermosphere and Ionosphere, Ph.D. Thesis, Univ. of Michigan (Ann Arbor), 1984.

Burnside, R.G., R.A. Behnke and J.C.G. Walker, "Meridional neutral winds in the thermosphere at Arecibo: simultaneous incoherent scatter and airglow observations," J. Geophys. Res. 88, 3181–3189, 1983.

Burnside, R.G., J.W. Meriwether and M.R. Torr, "Contamination of ground-based measurements of OI (6300 Å) and NI (5200 Å) airglow by OH emissions," Planet. Space Sci. 25, 985–988, 1977.

Burnside, R.G., J.C.G. Walker, R.A. Behnke and C.A. Tepley, "Plasma dynamics in the night-time F-region at Arecibo," J. Atmos. Terr. Phys. 47, 925–939, 1985.

Burrage, M.D., C.G. Fesen and V.J. Abreu, "Low-latitude thermospheric neutral winds determined from AE-E measurements of the 6300 Å nightglow at solar maximum," J. Geophys. Res. 95, 10357–10364, 1990.

Carlson, H.C., Ionospheric Heating by Conjugate Point Photoelectrons as Observed at Arecibo, Ph.D. Thesis, Cornell Univ. (Ithaca, N.Y.), 1965.

Chamberlain, J.W., Physics of the Aurora and Airglow, Academic Press, New York, 1961.

Chamberlain, J.W. and D.M. Hunten, Theory of Planetary Atmospheres (an Introduction to their Physics and Chemisry), 2nd ed., Academic Press, Orlando, Florida, 1987.

Chapman, S., F.R.S., "Some phenomena of the upper atmosphere," Proc. Roy. Soc. A132, 353–374, 1931.

Chapman, S. and R.S. Lindzen, Atmospheric Tides, Gordon and Breach, New York, 1970.

Chen, A., R. Johnson and M.A. Biondi, "Measurements of the O^++N_2 and O^++O_2 reaction rates from 300 to 900 K," J. Chem. Phys. 69, 2688–2691, 1978.

Cogger, L.L. and C.D. Anger, "The OI 5577 Å experiment on the ISIS 2 satellite," J. Atmos. Terr. Phys. 35, 2081–2084, 1973.

Cogger, L.L., G.J. Nelson, M.A. Biondi, R.D. Hake, Jr. and D.P. Sipler, "Coincident F-region temperature determinations from incoherent backscatter and Doppler broadening of [OI] 6300 Å," J. Geophys. Res. 75, 4887–4889, 1970.

Cogger, L.L., L.S. Smith and R.M. Harper, "Aeronomical determination of the efficiency of $O(^1D)$ production by dissociative recombination of O_2^+," Planet. Space Sci. 25, 155-159, 1977.

Cogger, L.L., J.C.G. Walker, J.W. Meriwether and R.G. Burnside, "F region airglow: are ground-based observations consistent with recent satellite results?" J. Geophys. Res. 85, 3013–3020, 1980.

Cogger, L.L., V.B. Wickwar and H.C. Carlson, "Combined airglow and incoherent scatter observations as a technique for studying neutral atmospheric variations," Radio Science 9, 205–210, 1974.

Dalgarno, A. and J.C.G. Walker, "The red line of atomic oxygen in the day airglow," J. Atmos. Sci. 21, 463–474, 1964.

Eather, R.H. and D.L. Reasoner, "Spectrophotometry of faint light sources with a tilting filter photometer: theory and practice," Appl. Opt. 8, 227–242, 1969.

Evans, J.V., "Theory and practice of ionosphere study by Thomson scatter radar," Proc. IEEE 57, 496–530, 1969.

Evans, J.V., "Incoherent scatter contributions to studies of the dynamics of the lower thermosphere," Rev. Geophys. Space Phys. 16, 195–216, 1978.

Evans, J.V., W.L. Oliver, Jr., and J.E. Salah, "Thermospheric properties as deduced from incoherent scatter measurements," J. Atmos. Terr. Phys. 41, 259–278, 1979.

Farley, D.T., "Review of the theory of Thomson scattering," in Thomson Scatter Studies of the Ionsophere – an Informal Conference Record, (J.V. Evans, ed.) Univ. of Illinois (Urbana), 1967.

Fesen, C.G. and V.J. Abreu, "Modeling the 6300 Å low-latitude nightglow," J. Geophys. Res. 92, 1231–1239, 1987.

Fesen, C.G., R.E. Dickinson and R.G. Roble, "Simulation of the thermospheric tides at equinox with the National Center for Atmospheric Research thermospheric general circulation model," J. Geophys. Res. 91, 4471–4489, 1986.

Forbes, J.M., "Tidal variations in thermospheric O, O_2, N_2, Ar, He and H," J. Geophys. Res. 83, 3691–3698, 1978.

Forbes, J.M., "Atmospheric tides 1. Model description and results for the solar diurnal component," J. Geophys. Res. 87, 5222–5240, 1982a.

Forbes, J.M., "Atmospheric tides 2. The solar and lunar semidiurnal components," J. Geophys. Res. 87, 5241–5252, 1982b.

Forbes, J.M. and H.B. Garrett, "Theoretical studies of atmospheric tides," Rev. Geophys. Space Phys. 17, 1951–1981, 1979.

Giraud, A. and M. Petit, Ionospheric Techniques and Phenomena, D. Reidel, Dordrecht, 1978.

Guberman, S.L., "The production of $O(^1S)$ from dissociative recombination of O_2^+," Nature 327, 408–409, 1987.

Guberman, S.L., "The production of $O(^1D)$ from dissociative recombination of O_2^+," Planet. Space Sci. 36, 47–53, 1988.

Hagfors, T. and R.A. Behnke, "Measurement of three-dimensional plasma velocities at the Arecibo Observatory," Radio Sci. 9, 89–93, 1974.

Hargreaves, J.K., The Upper Atmosphere and Solar-Terrestrial Relations, Van Nostrand Reinhold, Wokingham, Berkshire, 1979.

Harper, R.M., Dynamics of the Neutral Atmosphere in the 200–500 km. Height Region at Low Latitudes, Ph.D. Thesis, Rice University (Houston), 1971.

Harper, R.M., "Some results on mean tidal structure and day-to-day variability over Arecibo," J. Atmos. Terr. Phys. 43, 255–262, 1981.

Hays, P.B., V.J. Abreu, S.C. Solomon and J.H. Yee, "The visible airglow experiment - a review," Planet. Space Sci. 36, 21–35, 1988.

Hays, P.B., D.W. Rusch, R.G. Roble and J.C.G. Walker, "The OI (6300 Å) airglow," Rev. Geophys. Space Phys. 16, 225–232, 1978.

Hedin, A.E., "A revised thermospheric model based on mass spectrometer and incoherent scatter data: MSIS-83," J. Geophys. Res. 88, 10170–10188, 1983.

Hedin, A.E., N.W. Spencer and H.G. Mayr, "The semidiurnal and terdiurnal tides in the equatorial thermosphere from AE-E measurements," J. Geophys. Res. 85, 1787–1791, 1980.

Hernandez, G., "Contamination of the OI ($^3P_2$ - $^1D_2$) emission line by the (9 - 3) band of OH $X^2\Pi$ in high resolution measurements of the night sky," J. Geophys. Res. 79, 1119–1123, 1974.

Hines, C.O., "Motions of the neutral atmosphere," in Physics of the Earth's Upper Atmosphere, (C.O. Hines, I. Paghis, T.R. Hartz, J.A. Fejer, eds.) Prentice-Hall Inc., New Jersey, 1965.

Ioannidis, G. and D.T. Farley, "Incoherent scatter observations at Arecibo using compressed pulses," Radio Science 7, 763–766, 1972.

Kelley, M.C., The Earth's Ionosphere: Plasma Physics and Electrodynamics, Academic Press, San Diego, 1989.

Link, R. and L.L. Cogger, "A reexamination of the OI 6300 Å nightglow," J. Geophys. Res. 93, 9883–9892, 1988.

Link, R., J.C. McConnell and G.G. Shepherd, "A self-consistent evaluation of the rate constants for the production of the OI 6300 Å airglow," Planet. Space Sci. 29, 589–594, 1981.

Mayr, H.G., P. Bauer, H.C. Brinton, L.H. Brace and W.E. Potter, "Diurnal and seasonal variations in atomic and molecular oxygen inferred from Atmosphere Explorer-C," Geophys. Res. Lett. 3, 77–80, 1976.

Mayr, H.G., I. Harris, N.W. Spencer, A.E. Hedin, L.E. Wharton, H.S. Porter, J.C.G. Walker and H.C. Carlson, Jr., "Tides and the midnight temperature anomaly in the thermosphere," Geophys. Res. Lett. 6, 447–450, 1979.

McCormac, B.M., ed., Aurora and Airglow, Reinhold, New York, 1967.

Miller, N.J., L.H. Brace, N.W. Spencer, G.R. Carignan, "DE 2 observations of disturbances in the upper atmosphere during a geomagnetic storm," J. Geophys. Res. 95, 21017–21031, 1990.

Moorcroft, D.R., "The determination of ionic composition and temperature from the spectra of Thomson scattered signals," in Thomson Scatter Studies of the Ionosphere – an Informal Conference Record, (J.V. Evans, ed.) Univ. of Illinois (Urbana), 1967.

Nagy, A.F., R.G. Roble and P.B. Hays, "Stable mid-latitude red arcs: observations and theory," Space Sci. Rev. 11, 709–727, 1970.

Nelson, G.J. and L.L. Cogger, "Dynamical behaviour of the nighttime ionsophere at Arecibo," J. Atmos. Terr. Phys 33, 1711–1726, 1971.

Peterson, V.L., "F region photochemical nightglow emission," in Aurora and Airglow, (B.M. McCormac, ed.), Reinhold, New York, 1967.

Prölss, G.W., "Storm-induced changes in the thermospheric composition at middle latitudes," Planet. Space Sci. 35, 807-811, 1987.

Rao, R.V. and P.V. Kulkarni, "Measurements of extinction coefficient and the night airglow," Ann. Géophys. 29, 97–102, 1973.

Rassoul, H.K., R.P. Rohrbaugh and B.A. Tinsley, "Low-latitude particle precipitation and associated local magnetic disturbances," J. Geophys. Res. 97, 4041–4052, 1992.

Reddy, C.A., S. Fukao, T. Takami, M. Yamamoto, T. Tsuda, T. Nakamura, S. Kato, "A MU radar-based study of mid-latitude F region response to a geomagnetic disturbance," J. Geophys. Res. 95, 21077–21094, 1990.

Rees, M.H., Physics and Chemistry of the Upper Atmosphere, Cambridge U. Press, Cambridge, 1989.

Rees, M.H. and R.G. Roble, "Observations and theory of the formation of stable auroral arcs," Rev. Geophys. Space Phys. 13, 201–242, 1975.

Reinsch, C.H., "Smoothing by spline functions," Numer. Math. 10, 177–183, 1967.

Richmond, A.D., "Thermospheric dynamics and electrodynamics," in Solar-Terrestrial Physics: Principles and Theoretical Foundations, (R.L. Carovillano and J.M. Forbes, eds.), D. Reidel, Dordrecht, 1983.

Rishbeth, H., "On the F2-layer continuity equation," J. Atmos. Terr. Phys. 48, 511–519, 1986.

Rishbeth, H. and O.K. Garriott, Introduction to Ionospheric Physics, Academic Press, New York, 1969.

Rishbeth, H., R. Gordon, D. Rees and T.J. Fuller-Rowell, "Modelling of thermospheric composition changes caused by a severe magnetic storm," Planet. Space Sci. 33, 1283–1301, 1985.

Roble, R.G., E.C. Ridley, A.D. Richmond and R.E. Dickinson, "A coupled thermosphere/ionosphere general circulation model," Geophys. Res. Lett. 15, 1325–1328, 1988.

Sahai, Y., J.A. Bittencourt, H. Takahashi, N.R. Teixeira, J.H.A. Sobral, B.A. Tinsley and R.P. Rohrbaugh, "Multispectral optical observations of ionospheric F-region storm effects at low latitude," Planet. Space Sci. 36, 371–381, 1988.

Sahai, Y., J.A. Bittencourt, H. Takahashi, N.R. Teixeira, B.A. Tinsley and R.P. Rohrbaugh, "Analysis of storm-time low-latitude simultaneous ionospheric and nightglow emission measurements," J. Atmos. Terr. Phys. 52, 749–757, 1990.

St.-Maurice, J.-P. and D.G. Torr, "Nonthermal rate coefficients in the ionosphere: the reactions of O^+ with N_2, O_2 and NO," J. Geophys. Res. 83, 969–977, 1978.

Schmitt, G.A., V.J. Abreu and P.B. Hays, "Non-thermal $O(^1D)$ produced by dissociative recombination of O_2^+: a theoretical model and observational results," Planet. Space Sci. 29, 1095–1099, 1981.

Schunk, R.W., "The terrestrial ionosphere," in Solar-Terrestrial Physics: Principles and Theoretical Foundations, (R.L. Carovillano and J.M. Forbes, eds.), D. Reidel, Dordrecht, 1983.

Sharp, W.E., "Sources of the emission features between 2000 and 8000 Å in the thermosphere," Can. J. Phys 64, 1594–1607, 1986.

Sobral, J.H.A., H. Takahashi, M.A. Abdu, P. Muralikrishna, Y. Sahai and C.J. Zamlutti, "$O(^1S)$ and $O(^1D)$ quantum yields from rocket measurements of electron densities and 557.7 and 630.0 nm emissions in the nocturnal F-region," Planet. Space Sci. 40, 607–619, 1992.

Takahashi, H., B.R. Clemesha, P.P. Batista, Y. Sahai, M.A. Abdu and P. Muralikrishna, "Equatorial F-region OI 6300 Å and OI 5577 Å emission profiles observed by rocket-borne airglow photometers," Planet. Space Sci. 38, 547–554, 1990.

Tinsley, B.A., "Energetic neutral atom precipitation during magnetic storms: optical emission, ionization, and energy deposition at low and middle latitudes," J. Geophys. Res. 84, 1855–1864, 1979.

Tinsley, B.A., R.P. Rohrbaugh, H. Rassoul, Y. Sahai, N.R. Teixeira and D. Slater, "Low latitude aurorae and storm time current systems," J. Geophys. Res. 91, 11257–11269, 1986.

Tinsley, B.A., Y. Sahai, M.A. Biondi and J.W. Meriwether, Jr., "Equatorial particle precipitation during magnetic storms and relationship to equatorial thermospheric heating," J. Geophys Res. 93, 270–276, 1988.

Torr, M.R., P.B. Hays, B.C. Kennedy and J.C.G. Walker, "Intercalibration of airglow observatories with the Atmosphere Explorer Satellite," Planet. Space Sci. 25, 173–184, 1977.

Wickwar, V.B., Photoelectrons from the Magnetic Conjugate Point Studied by Means of the 6300 Å Predawn Enhancement and the Plasma Line Enhancement, Ph.D. Thesis, Rice University (Houston), 1971.

Wickwar, V.B., L.L. Cogger and H.C. Carlson, "The 6300 Å $O(^1D)$ airglow and dissociative recombination," Planet. Space Sci. 22, 709-724, 1974.

Yee, J-H., "Non-thermal distribution of $O(^1D)$ atoms in the night-time thermosphere," Planet. Space Sci. 36, 89–97, 1988.

Yee, J-H. and A.Dalgarno, "Energy transfer of $O(^1D)$ atoms in collision with $O(^3P)$ atoms," Planet. Space Sci. 35, 399–404, 1987.

Yee, J-H., A.Dalgarno and S.L. Guberman, "The quenching of $O(^1D)$ by $O(^3P)$ atoms," EOS Trans. 66, 993, 1985.

Zipf, E.C., "The dissociative recombination of O_2^+ ions into specifically identified final atomic states," Bull. Am. Phys. Soc. 15, 418, 1970.

Zipf, E.C., "The excitation of the $O(^1S)$ state by the dissociative recombination of O_2^+ ions: electron temperature dependence," Planet. Space Sci. 36, 621–628, 1988.